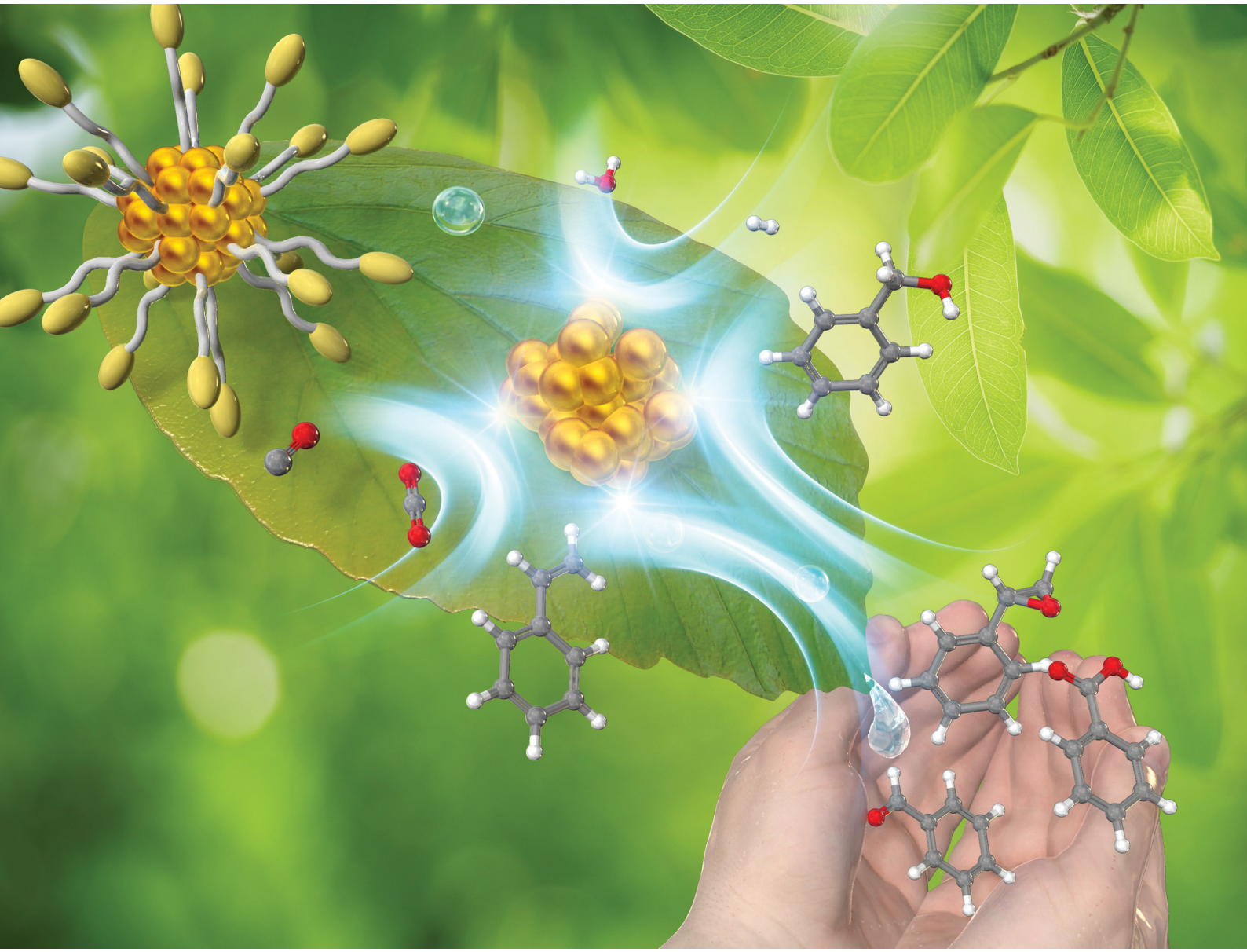
Volume 6
Number 6
June 2021
Pages 403–498

Nanoscale Horizons

The home for rapid reports of exceptional significance in nanoscience and nanotechnology

rsc.li/nanoscale-horizons



ISSN 2055-6756

ROYAL SOCIETY OF CHEMISTRY

REVIEW ARTICLE

Yuichi Negishi *et al.*

Toward the creation of high-performance heterogeneous catalysts by controlled ligand desorption from atomically precise metal nanoclusters

NCNST

Nanoscale Horizons

ROYAL SOCIETY OF CHEMISTRY

REVIEW

View Article Online
View Journal | View Issue

Check for updates

Cite this: *Nanoscale Horiz.*, 2021, **6**, 409

Toward the creation of high-performance heterogeneous catalysts by controlled ligand desorption from atomically precise metal nanoclusters

Tokuhisa Kawawaki,[abc] Yuki Kataoka,[a] Momoko Hirata,[a] Yuki Iwamatsu,[a] Sakiat Hossain[a] and Yuichi Negishi*[abc]

Ligand-protected metal nanoclusters controlled by atomic accuracy (*i. e.* atomically precise metal NCs) have recently attracted considerable attention as active sites in heterogeneous catalysts. Using these atomically precise metal NCs, it becomes possible to create novel heterogeneous catalysts based on a size-specific electronic/geometrical structure of metal NCs and understand the mechanism of the catalytic reaction easily. However, to create high-performance heterogeneous catalysts using atomically precise metal NCs, it is often necessary to remove the ligands from the metal NCs. This review summarizes previous studies on the creation of heterogeneous catalysts using atomically precise metal NCs while focusing on the calcination as a ligand-elimination method. Through this summary, we intend to share state-of-art techniques and knowledge on (1) experimental conditions suitable for creating high-performance heterogeneous catalysts (*e.g.*, support type, metal NC type, ligand type, and calcination temperature), (2) the mechanism of calcination, and (3) the mechanism of catalytic reaction over the created heterogeneous catalyst. We also discuss (4) issues that should be addressed in the future toward the creation of high-performance heterogeneous catalysts using atomically precise metal NCs. The knowledge and issues described in this review are expected to lead to clear design guidelines for the creation of novel heterogeneous catalysts.

Received 23rd January 2021,
Accepted 6th April 2021

DOI: 10.1039/d1nh00046b

rsc.li/nanoscale-horizons

Open Access Article. Published on 12 2021. Downloaded on 02.06.2026 12:22:59.
This article is licensed under a Creative Commons Attribution 3.0 Unported Licence.

[a] *Department of Applied Chemistry, Faculty of Science, Tokyo University of Science, Kagurazaka, Shinjuku-ku, Tokyo 162-8601, Japan. E-mail: negishi@rs.tus.ac.jp*
[b] *Photocatalysis International Research Center, Tokyo University of Science, 2641 Yamazaki, Noda, Chiba 278-8510, Japan*
[c] *Research Institute for Science and Technology, Tokyo University of Science, Kagurazaka, Shinjuku-ku, Tokyo 162-8601, Japan*



Tokuhisa Kawawaki

Tokuhisa Kawawaki Assistant Professor of the Department of Applied Chemistry at Tokyo University of Science. He received a PhD degree (2015) in Applied Chemistry from the University of Tokyo. In 2016–2017, he worked as a Japan Society for the Promotion of Science (JSPS) Postdoctoral fellow (PD) at the University of Melbourne. In 2017–2018, he worked as a JSPS super PD (SPD) at Kyoto University. In 2019, he moved to his current position. His current research topics include the synthesis of metal nanoparticles and nanoclusters in solution and their applications for photoelectrochemistry and photocatalysts.



Yuki Kataoka

Yuki Kataoka Master course student in the Negishi group at Tokyo University of Science. He received a MSc (2021) in Chemistry from Tokyo University of Science. His research interests include the activation of water-splitting photocatalysts by heteroatom doping of cocatalysts and elucidation of calcination process for loading precise metal NCs on photocatalysts.

Open Access Article. Published on 12 2021. Downloaded on 02.06.2026 12:22:59.
This article is licensed under a Creative Commons Attribution 3.0 Unported Licence.

1. Introduction

1.1. Catalysts

Modern affluent society is supported by a wide variety of substances. Most of those are produced by chemical reactions, and most of the chemical reactions are promoted by catalysts. Although the number of elements that can be handled stably on the earth is limited, catalysts can produce a wide variety of useful chemical substances from this limited number of elements and therefore are indispensable materials in our society. Researchers have developed various catalysts one after another to meet the demands of society, leading to the establishment of a fulfilling life and helping to overcome food shortages and reduce environmental pollution.[1] However, our society still has many problems related to resources, energy, and the environment. Therefore, future studies are expected to develop novel catalysts that will address these problems facing modern society.

The concept of catalysis was first presented in 1836. Berzelius described in his paper that "catalysis is the acceleration of a slow chemical reaction by the presence of a foreign substance".[2] Then, in 1901, Ostwald defined a catalyst as "any substance which alters the rate of a chemical reaction without appearing in the final product".[3] This definition also clearly distinguished between "chemical equilibrium" and "reaction rate". Thus, a catalyst is a substance that can change a chemical reaction without being consumed. In reality, although the catalyst does not change before and after the chemical reaction, it forms a reaction intermediate with the reactant during catalysis. Therefore, in modern chemistry, the catalyst is defined as "a substance that changes the reaction rate in a chemical reaction but does not appear in the general reaction formula and does not change the equilibrium constant, reduces the apparent activation energy by creating a new reaction pathway, and allows a specific reaction among several possible reactions to proceed selectively".[4]

A catalyst contained in the same phase as the reactant is called a homogeneous catalyst. For example, molecular catalysts,[5] such as metal complexes used when synthesizing pharmaceuticals and organic compounds in a solvent, are classified as homogeneous catalysts. These catalysts can generally be designed at the molecular level, which allows the desired reaction to proceed with high selectivity. However, because all of the substances related to the reaction are dissolved in a solvent, it is often difficult to separate products and recover the catalyst.



Momoko Hirata

Momoko Hirata Master course student in the Negishi group at Tokyo University of Science. She received a BSc (2020) in Chemistry from Tokyo University of Science. Her research interests include the elucidation of calcination process for loading precise metal NCs on photocatalysts.



Yuki Iwamatsu

Yuki Iwamatsu Master course student in the Negishi group at Tokyo University of Science. He received a BSc (2020) in Chemistry from Tokyo University of Science. His research interests include the electrochemical application of precise metal NCs.



Sakiat Hossain

Sakiat Hossain Assistant Professor at Tokyo University of Science. He obtained his BSc (2005) from Ramakrishna Mission Residential College, Narendrapur, Calcutta University, MSc (2007) from the Indian Institute of Technology Delhi, and PhD (2013) from the Indian Institute of Technology Kanpur under the supervision of Prof. V. Chandrasekhar. He joined Tokyo University of Science in 2015. His research interests include the synthesis of novel metal clusters and study of their properties.



Yuichi Negishi

Yuichi Negishi Professor of the Department of Applied Chemistry at Tokyo University of Science. He received a PhD degree in Chemistry in 2001 under the supervision of Prof. Atsushi Nakajima from Keio University. Before joining Tokyo University of Science in 2008, he was employed as an Assistant Professor at Keio University and at the Institute for Molecular Science. His current research interests include the precise synthesis of stable and functionalized metal nanoclusters and their applications in energy and environmental materials.

This journal is © The Royal Society of Chemistry 2021

Open Access Article. Published on 12 2021. Downloaded on 02.06.2026 12:22:59.
This article is licensed under a Creative Commons Attribution 3.0 Unported Licence.

Furthermore, in such a reaction system, the activity is generally not so high because the reaction temperature is limited to below the boiling point of the solvent.

A catalyst with a phase different from that of the reactant and product, such as a solid-state catalyst[6,7] (metal/metal oxide nanoparticles loaded on a support), is called a heterogeneous catalyst.[8] Generally, heterogeneous catalysts are used in large-scale industrial processes. In this reaction system, the reaction temperature can be raised to the heat-resistant temperature of solid-state catalysts such that high activity is often obtained. In addition, it is relatively easy to separate products and recycle the catalysts in this reaction system, which is a great advantage in industrial processes. However, the surfaces of heterogeneous catalysts are not always homogeneous, and it is difficult to design and control them at the molecular level. For this reason, reactions using heterogeneous catalysts often have low selectivity.

In the development of catalysts, it is very important to account for the activity, selectivity, durability/stability, and environmental burden.[9] Understanding the reaction mechanism is also essential for improving the activity and selectivity. Thus, it is necessary to develop many catalysts for which these factors are improved.

1.2. Atomically precise metal nanoclusters as catalysts

Ligand-protected metal nanoclusters controlled by atomic accuracy (*i. e.* atomically precise metal NCs)[10–46] have attracted considerable attention as novel homogeneous and heterogeneous catalysts. Research on the synthesis and determination of geometrical structure of these atomically precise metal NCs began in the 1970s, and initially gold (Au) NCs protected by phosphine (PR_3) and halogen (X) ($Au_n(PR_3)_mX_l$ NCs; n = number of Au atoms; m and l = number of PR_3 and X, respectively)[47–58] and platinum (Pt) and palladium (Pd) NCs protected by PR_3 and/or carbon monoxide (CO) ($M_n(PR_3)_m(CO)_l$; M = Pt or Pd)[59–67] were studied as the main target. However, since the precise synthesis of thiolate (SR)-protected Au NCs ($Au_n(SR)_m$ NCs),[68] which show higher stability than the above-described metal NCs, was achieved in 2005, SR-protected Au,[10–17,19,21,26,33,36,41,42] silver (Ag),[10,18,20,22,43] copper (Cu)[31,32] and their alloy[25,27–30,34,35,37–40,44] NCs have become the main research focus. In addition, numerous studies have been conducted on metal NCs with alkyne (C≡CR),[73–76] selenolate,[77–84] and tellurolate[33] as ligands in recent years. For the synthesis and electronic/geometrical structure of these metal NCs, we point the interested reader to a number of reviews published in the last few years by several groups, including ours.[23,24,85–95]

Regarding these atomically precise metal NCs, in 2010, Jin *et al.* found that $Au_{25}(PET)_{18}$ (PET = phenylethanethiolate) can function as either a homogeneous catalyst (sometimes called quasi-homogeneous; Fig. 1A) or a heterogeneous catalyst (Fig. 1B–D) for the selective hydrogenation of benzalacetone by hydrogen (H_2).[96] Since then, the catalytic reaction using atomically precise metal NCs has attracted much attention. As described in Section 1.1, heterogeneous catalysts have an advantage in the recycling. In addition, the use of support typically results in the improvements of the catalytic activity; *e.g.* the catalytic activity of $Au_{99}(SPh)_{42}$ (SPh = phenylthiolate) for the hydrogenation of 4-nitrobenzaldehyde to 4-nitrobenzyl alcohol was reported to be improved tenfold by supporting them on cerium(IV) oxide (CeO_2).[97] Thus, the recent studies have particularly focused on the use of atomically precise metal NCs in a heterogeneous catalyst.

Atomically precise metal NCs are attracting attention as heterogeneous catalysts for the following reasons:

(1) In a conventional heterogeneous catalyst, metal nanoparticles (NPs) on a support have a relatively large size distribution. For such a system, it is difficult to identify highly active particles and selectively load them. In contrast, for heterogeneous catalysts loaded with atomically precise metal NCs, metal NCs with an atomically defined chemical composition are loaded such that highly active metal NCs can be identified and thereby selectively loaded onto supports.

(2) Ligand-protected metal NCs exhibit different physicochemical properties and functions from bulk metals, and these properties and functions change depending on the number of constituent atoms and the type of ligand.[86,98–120] Therefore, it is possible to create a new heterogeneous catalyst with a unique catalytic activity when using these metal NCs.

(3) In recent years, it has become possible to synthesize various types of atomically precise metal NCs.[18,22–24,31–33,69–84]

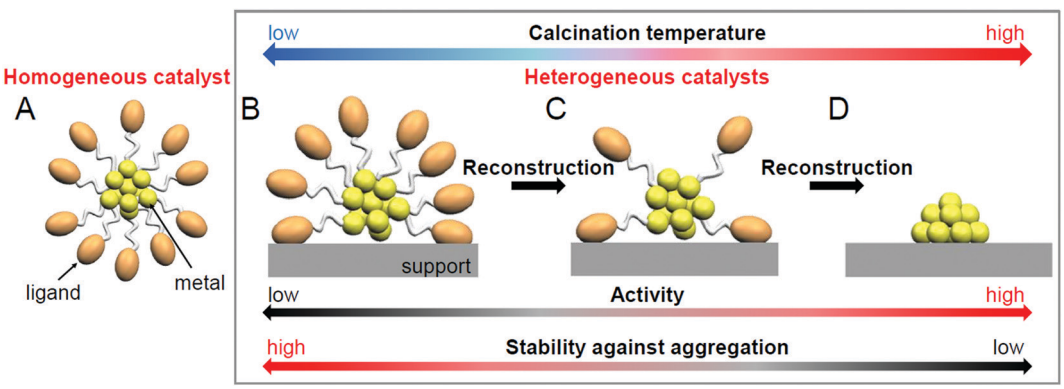


Fig. 1 Categorization of catalysts: (A) homogeneous catalyst (sometimes called quasi-homogeneous catalyst) and (B–D) heterogeneous catalysts. This review discusses heterogeneous catalysts prepared using atomically precise, ligand-protected metal NCs (B–D). Note that calcination induces not only the ligand elimination but also the reconstruction of the metal-core structure.

Open Access Article. Published on 12 2021. Downloaded on 02.06.2026 12:22:59.
This article is licensed under a Creative Commons Attribution 3.0 Unported Licence.

Therefore, it is possible to create a heterogeneous catalyst suitable for the desired reaction based on the design, and it is expected that high reaction selectivity could be achieved.

(4) For atomically precise metal NCs, it is often possible to determine the geometrical structure through single-crystal X-ray diffraction (SC-XRD) analysis.[26,28–30,37,39,40,98–100,121–180] Therefore, for heterogeneous catalysts using atomically precise metal NCs, it is possible to obtain a deep understanding of the correlation between the geometrical/interface structure of catalysts and catalytic activity and the reaction mechanism.

As described above, the use of atomically precise metal NCs as catalysts has many advantages for both the development of practical catalysts and the understanding of the mechanism of the catalytic reaction. Therefore, it seems possible to create a heterogeneous catalyst, in which the above-described four factors (activity, selectivity, durability/stability, and environmental burden) are improved using this catalyst system. However, the presence of ligands on the surface of the metal NCs interrupts the approach of the reactant to the surface of the metal NCs, which often leads to a decrease in catalytic activity (Fig. 1B). Therefore, many attempts have been made to create heterogeneous catalysts with even higher activity by removing part (Fig. 1C) or all (Fig. 1D) of the ligands.[24,181,182] For example, in 2009, Tsukuda *et al.* succeeded in preparing a heterogeneous catalyst with both high activity and selectivity by removing all the ligands of triphenylphosphine (PPh_3)-protected Au_{11} NCs.[183] In this way, it is expected that a heterogeneous catalyst having even higher activity than that containing the ligands will be created when an appropriate amount of ligands is removed from the metal NCs.

1.3. Purpose and contents of this review

As mentioned in Section 1.2, ligand elimination induces activation of catalysts. However, ligand elimination also induces reconstruction and aggregation of metal NCs (Fig. 1B–D). When aggregation occurs, the catalytic activity decreases as the proportion of surface atoms in the loaded metal NCs decreases. Therefore, in a ligand elimination, it is extremely important to select suitable conditions. The conditions appear to vary depending on the type of support, the metal NCs, the ligands, and the catalytic reaction. In addition, if the desorbed ligands from metal NCs are adsorbed on the support, they will also affect the catalytic activity. Indeed, Burns *et al.* reported that nickel-oxide supported-Au NPs decreased the catalytic activity when the sulfate ions existed on the support.[184] Thus, to create a highly active heterogeneous catalyst, it is necessary to deeply understand the mechanism of the ligand elimination. However, as the number of studies on the creation of highly functional heterogeneous catalysts based on such a ligand elimination has increased rapidly in recent years, it is difficult for researchers (especially beginners) to extract all of the knowledge gained from previous studies.

This review summarizes representative previous studies on the preparation of heterogeneous catalysts using atomically precise metal NCs while focusing on calcination as a ligand-elimination method. The purpose of this review is to discuss existing knowledge on (1) the experimental conditions suitable for the creation of highly functional heterogeneous catalysts (types of support, metal NCs, and ligands and calcination temperature), (2) the calcination mechanism, and (3) the mechanism of catalytic reaction over the created heterogeneous catalyst.

In the next section (Section 2), we describe previous studies while classifying them by the catalytic reaction. Then, we describe the experimental conditions suitable for the creation of high-performance heterogeneous catalysts (Section 3.1), calcination mechanisms (Section 3.2), and the mechanism of the catalytic reaction over the prepared heterogeneous catalyst (Section 3.3). After a brief summary in Section 4, the future outlook is described in Section 5.

For metal NCs whose constituent atoms are not controlled with atomic precision, the creation of heterogeneous catalysts using calcination has been well studied over many years.[185–200] However, this review summarizes the previous studies while focusing on examples using atomically precise metal NCs, the study of which only started in recent years. In addition, the ligands of metal NCs can be removed not only by calcination but also by light irradiation,[201–203] oxidation,[204–207] or reduction[208] treatment. However, we do not touch on such methods because of space limitations. For readers interested in the elimination of ligands by methods other than calcination, it is better to read other reviews or original papers.

2. Examples of activation of atomically precise metal nanoclusters

In this section, we summarize representative studies on the functionalization of heterogeneous catalysts based on ligand elimination while classifying the studies by the catalytic reaction. The geometrical structures of the atomically precise metal NCs used in these studies are shown in Fig. 2. In addition, the metal NCs and supports used in each study are summarized in Table 1,[128,178,180,183,200,209–247] and the characteristics of each support are summarized in Table 2.[183,184,198,209,211,212,214,220,234,248–258] For readers interested in the details of the experimental conditions in each catalytic reaction, it is better to read the original paper. In the following, for example, Au_n NCs loaded on a metal oxide are represented as Au_n/metal oxide.

2.1. Oxidation reaction

2.1.1. Alcohol oxidation. Alcohol oxidation is one of the most important reactions in the organic synthesis of chemicals and pharmaceutical products. For these oxidation reactions, in recent years, reactions using molecular oxygen (O_2), which is abundant in the atmosphere, as an oxidant have attracted particular attention from the viewpoints of environmental harmony and cost reduction. In 2009, Tsukuda *et al.* prepared an alcohol oxidation catalyst by loading Au_{11} NCs on mesoporous silica (SBA-15).[183] In this experiment, PPh_3-protected Au_{11} NCs (the authors estimated the main product to be $[Au_{11}(PPh_3)_8Cl_2]^+$ (Cl = chlorine); Fig. 2A) were first adsorbed on SBA-15 and then calcined at 200 °C for 2 h under vacuum to remove the

 This journal is © The Royal Society of Chemistry 2021

Open Access Article. Published on 12 2021. Downloaded on 02.06.2026 12:22:59.
This article is licensed under a Creative Commons Attribution 3.0 Unported Licence.

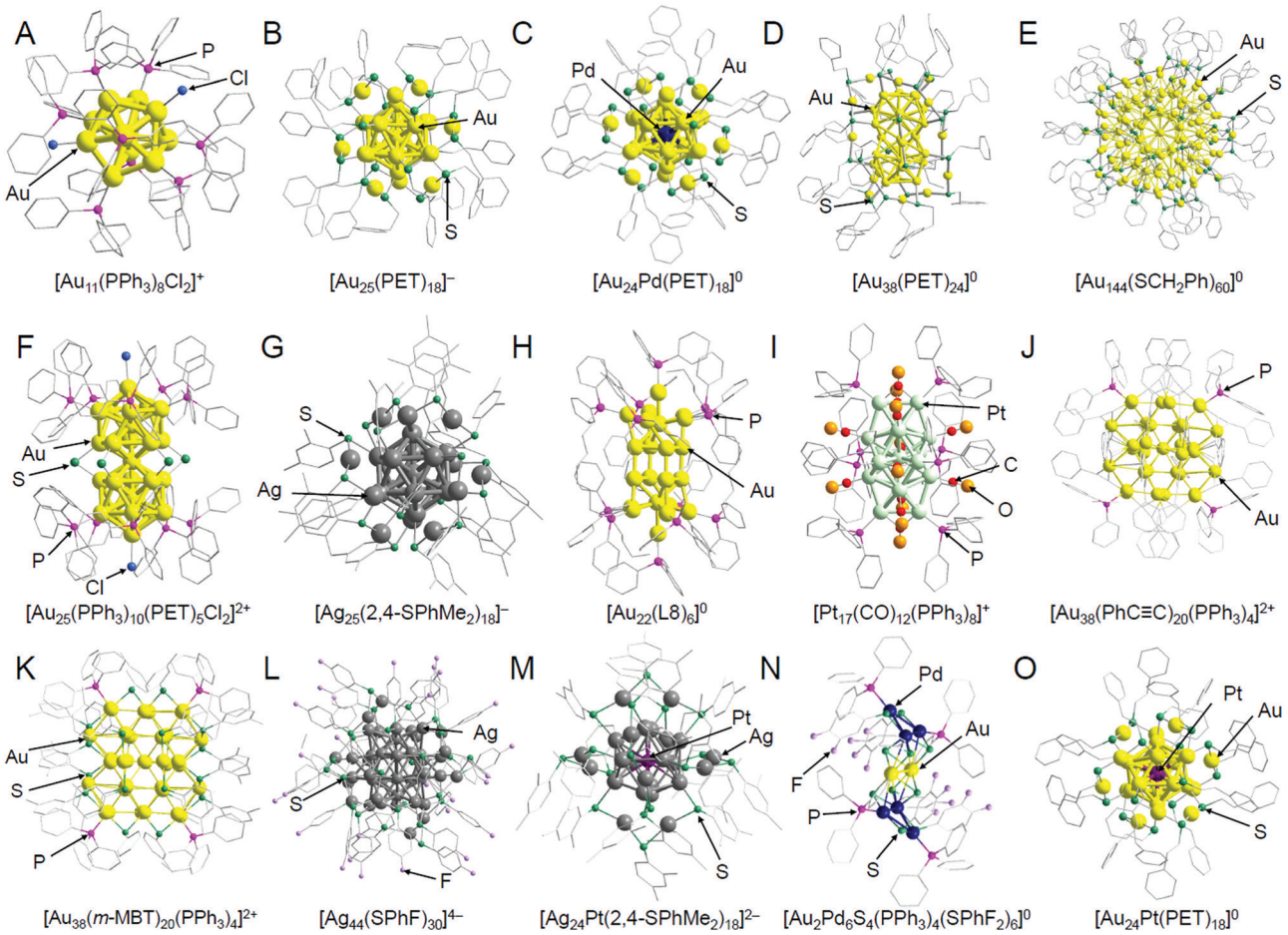


Fig. 2 Geometrical structures of atomically precise, ligand-protected metal NCs: (A) $[Au_{11}(PPh_3)_8Cl_2]^+$,[171] (B) $[Au_{25}(PET)_{18}]^-$,[42] (C) $[Au_{24}Pd(PET)_{18}]^0$,[172] (D) $[Au_{38}(PET)_{24}]^0$,[173] (E) $[Au_{144}(SCH_2Ph)_{60}]^0$,[174] (F) $[Au_{25}(PPh_3)_{10}(PET)_5Cl_2]^{2+}$,[175] (G) $[Ag_{25}(2,4\text{-}SPhMe_2)_{18}]^-$,[43] (H) $[Au_{22}(L8)_6]^0$,[176] (I) $[Pt_{17}(CO)_{12}(PPh_3)_8]^+$,[177] (J) $[Au_{38}(PhC{\equiv}C)_{20}(PPh_3)_4]^{2+}$,[178] (K) $[Au_{38}(m\text{-}MBT)_{20}(PPh_3)_4]^{2+}$,[178] (L) $[Ag_{44}(SPhF)_{30}]^{4-}$,[44] (M) $[Ag_{24}Pt(2,4\text{-}SPhMe_2)_{18}]^{2-}$,[179] (N) $[Au_2Pd_6S_4(PPh_3)_4(SPhF_2)_6]^0$,[180] and (O) $[Au_{24}Pt(PET)_{18}]^0$.[26] The gray points indicate carbon atoms, and hydrogen atoms are not shown. $Au_{25}(SR)_{18}$ (SR = SC12 or SG) discussed in Sections 2.1.1, 2.1.2, and 2.4 is considered to have a similar geometrical structure as $[Au_{25}(PET)_{18}]^-$ (B). $Au_{24}Pd(SC12)_{18}$ discussed in Section 2.1.1 is considered to have a similar geometrical structure as $[Au_{24}Pd(PET)_{18}]^0$ (C). $Au_{38}(SC12)_{24}$ discussed in Section 2.1.4 is considered to have a similar geometrical structure as $[Au_{38}(PET)_{24}]^0$ (D). $Au_{144}(PET)_{60}$ discussed in Sections 2.1.1–2.1.4 is considered to have a similar geometrical structure as $[Au_{144}(SCH_2Ph)_{60}]^0$ (E). These graphics were reproduced with permission from ref. 26, 42–44 and 171–180. Copyright 2016 Royal Society of Chemistry, 2008 American Chemical Society, 2015 American Chemical Society, 2013 Springer-Nature, 2014 American Chemical Society, 2016 American Chemical Society, 2010 American Chemical Society, 2018 AAAS, 2007 American Chemical Society, 2014 American Chemical Society, 2017 American Chemical Society, 2017 AAAS, 2017 American Chemical Society, 2018 Royal Society of Chemistry, respectively.

ligand (Fig. 3A). Based on the thermogravimetric analysis (TGA) performed under similar experimental conditions for $[Au_{11}(PPh_3)_8Cl_2]^+$, it was interpreted that all the ligands were removed from $[Au_{11}(PPh_3)_8Cl_2]^+$ by calcination. High-angle annular dark field-scanning transmission electron microscopy (HAADF-STEM) images showed that the particle size of the loaded Au NCs was 0.8 ± 0.3 nm (Fig. 3B and C), indicating that the Au_{11} NCs were loaded onto the mesoporous silica without any aggregation. It was interpreted that the use of mesoporous silica with small pore size and high specific surface area (Table 2) as a support greatly contributed to the suppression of the aggregation of Au_{11} NCs. In fact, some aggregation was observed when other mesoporous silicas (MCF or HMS), which cause the increase of the Au_n NCs density, were used as a support. The authors examined the catalytic activity of the obtained Au_{11}/SBA-15 for the benzyl alcohol oxidation (Scheme 1). In this experiment, hydrogen peroxide (H_2O_2) was used as the oxidant, and the solution was heated by microwave. As a result, Au_{11}/SBA-15 showed higher conversion efficiency and selectivity for benzoic acid (Scheme 1C) than the catalysts in which larger Au NP (Au_{NP}) was loaded by impregnation or precipitation methods (Au_{NP}/SBA-15). A similar phenomenon was observed when other primary benzyl alcohols were used as substrates. Unfortunately, Au_{11}/SBA-15 did not show high catalytic activity in the reaction using molecular O_2 as an oxidant at room temperature. However, this study is very important because it demonstrated that by using atomically precise metal NCs as a precursor, (1) fine metal NCs can be loaded and (2) it is possible to produce catalysts with higher activity and selectivity than those prepared using larger Au_{NP}.

Open Access Article. Published on 12 2021. Downloaded on 02.06.2026 12:22:59.
This article is licensed under a Creative Commons Attribution 3.0 Unported Licence.

Table 1 Catalytic reaction, preparation conditions of catalysts, and resulting particle size of loaded metal NCs

Reaction	NCs[a]	Support	Metal weight	Calc. atmosphere	Calc. temp./°C	Particle size/nm	Ref.[b]
Oxidation of benzyl alcohol	$Au_{11}(PPh_3)_8Cl_2$	SBA-15	0.4 wt%	Vacuum	200	0.8 ± 0.3	183
	$Au_{25}(SC12)_{18}$	MWCNTs	0.05–1.0 wt%	Vacuum	300	1.1 ± 0.2	209
					450	1.2 ± 0.2	
	$Au_{24}Pd(SC12)_{18}$				300	1.2 ± 0.3	
					450	1.2 ± 0.3	
	$Au_{25}(SC12)_{18}$	HPCSs	1.0 wt%	Vacuum	500	1.2 ± 0.3	210
	$Au_{25}(PET)_{18}$	HPCSs	1.0 wt%	Vacuum	550	1.0 ± 0.2	211
	$Au_{38}(PET)_{24}$					1.2 ± 0.3	
	$Au_{144}(PET)_{60}$					1.6 ± 0.1	
	$Au_{\sim 330}(PET)_{\sim 80}$					2.0 ± 0.2	
	$Au_{13}Cu_8(PPh_2Py)_{12}$	CNTs	—[c]	Vacuum	370	—[c]	128
	$Au_{25}(SPh\text{-}pNH_2)_{17}$	SBA-15	0.04 wt%	Air	400	1.9 ± 0.6	212
			1.07 wt%			1.8 ± 0.5	
Oxidation of glucose	$Au_{38}(PET)_{24}$	AC	1.38 wt%	Air	120	~1.6	213
Aerobic oxidation of cyclohexane	$Au_{10}(SG)_{10}$	HAP	0.2 wt%	Vacuum	300	1.0 ± 0.4	214
	$Au_{18}(SG)_{14}$					1.0 ± 0.4	
	$Au_{25}(SG)_{18}$					1.1 ± 0.5	
	$Au_{39}(SG)_{24}$					1.1 ± 0.5	
	$Au_{38}(PET)_{24}$	CeO_2 or Al_2O_3	2 wt%	Air	250 or 350	—[c]	215
	$Au_{38}(PET)_{24}$	CeO_2	0.5 wt%	Air	150	~1	216
					250		
		Al_2O_3			150	2–3	
					250		
	$Au_{38}(PET)_{24}$	CeO_2	0.5 wt%	Air	250	~1	217
		Al_2O_3				2–3	
	$Au_{25}(PET)_{18}$	TiO_2	0.54 wt%	Air	150	1.1 ± 0.3	218
					250	—[c]	
		SiO_2	0.34 wt%		150	1.2 ± 0.6	
					250	—[c]	
	$Au_{144}(PET)_{60}$	TiO_2	0.36 wt%		150	1.6 ± 0.6	
					250	—[c]	
		SiO_2	0.25 wt%		150	1.7 ± 0.4	
					250	—[c]	
Oxidation of styrene	$Au_{25}(SG)_{18}$	HAP	0.5 wt%	Vacuum	300	1.4 ± 0.6	219
	$Au_{25}(PET)_{18}$	SiO_2 or HAP	1 wt%	Vacuum	200	—[c]	220
	$Au_{38}(PET)_{24}$						
	$Au_{144}(PET)_{60}$						
	$Au_{25}(PET)_{18}$	CeO_2	1 wt%	Vacuum	260	—[c]	221
	$Au_{25}(PPh_3)_{10}(PET)_5Cl_2$						
	$Au_{25}(PET)_{18}$	SiO_2	~1 wt%	Vacuum	200	3–4	222
	$Au_{25}(PPh_3)_{10}(PET)_5Cl_2$						
	$Au_{25}(MHA)_{18}$	HAP	1 wt%	N_2	300	2.4 ± 1.3	223
		TiO_2				2.0 ± 0.8	
		AC				4.0 ± 5.0	
		PGO				3.8 ± 3.1	
		SiO_2				5.0 ± 3.9	
	$Ag_{25}(2,4\text{-}SPhMe_2)_{18}$	AC	4 wt%	Air	250	1.2 ± 0.3	224
					350	2.6 ± 0.4	
					450	2.8 ± 0.6	
Oxidation of CO	$Au_{38}(SC12)_{24}$	TiO_2	0.7 wt%	H_2/He	400	3.9 ± 1.0	225
	$Au_{25}(PET)_{18}$	TiO_2	1 wt%	O_2	150	—[c]	226
		Fe_2O_3	2 wt%				
		CeO_2					
	$Au_{38}(PET)_{24}$	CeO_2	1 wt%	O_2	100–250	—[c]	227
	$Au_{144}(PET)_{60}$	CeO_2	1 wt%	O_2/CO or H_2	80	—[c]	228
	$Au_{25}(PET)_{18}$	CeO_2	0.66 wt%	O_2	150	—[c]	229
	$Au_{25}(1SNap)_{18}$		0.63 wt%				
	$Au_{25}(2SNap)_{18}$		0.63 wt%				
	$Au_{36}(S\text{-}c\text{-}C_5H_9)_{24}$		0.74 wt%				
	$Au_{36}(SPh)_{24}$		0.72 wt%				
	$Au_{36}(SPh\text{-}t\text{Bu})_{24}$		0.64 wt%				
	$Au_{36}(2SNap)_{24}$		0.64 wt%				
	$Au_{38}(PET)_{24}$		0.69 wt%				
	$Au_{38}(SPh)_{24}$		0.73 wt%				
	$Au_{38}(o\text{-}MBT)_{24}$		0.71 wt%				
	$Au_{28}(S\text{-}c\text{-}C_6H_{11})_{20}$	CeO_2	0.32 μmol	O_2	150 or 300	—[c]	230
	$Au_{28}(TBBT)_{20}$					—[c]	
	$Au_{25}(PET)_{18}$	CeO_2	~1 wt%	O_2	150–350	—[c]	231
	$Au_{22}(L8)_6$	TiO_2, SiO_2, or CeO_2	~0.5 wt%	O_2	22–400	—[c]	232

This journal is © The Royal Society of Chemistry 2021

Open Access Article. Published on 12 2021. Downloaded on 02.06.2026 12:22:59.
This article is licensed under a Creative Commons Attribution 3.0 Unported Licence.

Table 1 (*continued*)

Reaction	NCs[a]	Support	Metal weight	Calc. atmosphere	Calc. temp./°C	Particle size/nm	Ref.[b]
	$Au_{38}(PET)_{24}$	CeO_2	2 wt%	O_2	150 or 250	2–4	233
	$Au_{25}(PET)_{18}$	Co_3O_4-EP-FDU-12	1.1–2 wt%	Air	300	—[c]	234
	$Au_{144}(PET)_{60}$	CuO-EP-FDU-12	1.1 wt%			1.7 ± 0.2	
	$Pt_{17}(CO)_{12}(PPh_3)_8$	γ-Al_2O_3	0.15 wt%	Vacuum	500	1.1 ± 0.2	235
Semihydrogenation of alkynes	$Au_{25}(PET)_{18}$	TiO_2, CeO_2, SiO_2, or Al_2O_3	1 wt%	Vacuum	300	—[c]	236
	$Au_{38}(PhC{\equiv}C)_{20}(Ph_3P)_4$ $Au_{38}(m\text{-MBT})_{20}(Ph_3P)_4$	TiO_2	0.4 wt%	Vacuum	130	1.4	178
Reduction of 4-nitrophenol	$Au_{25}(PET)_{18}$	CB	0.3 wt%	Air	125	1.5 ± 0.2	237
					200	1.7 ± 0.8	
					250	1.9 ± 1.1	
					350	2.1 ± 0.9	
Reduction of nitrobenzene	$Au_{25}(MHA)_{18}$	HAP	1 wt%	N_2	300	2.4 ± 1.3	223
		TiO_2				2.0 ± 0.8	
		AC				4.0 ± 5.0	
		PGO				3.8 ± 3.1	
		SiO_2				5.0 ± 3.9	
Hydrogenation of 3-nitrostyren	$Au_{25}(Cys)_{18}$	ZnAl-HT	1.1 wt%	Air	300	1.7 ± 0.5	238
H_2 generation	$Ag_{44}(SPhF)_{30}$	MPC	0.2 wt%	Vacuum	150 and 300	1–2	239
Photocatalytic HER and OER	$Au_{25}(SG)_{18}$	$BaLa_4Ti_4O_{15}$	0.1 wt%	Reduced pressure	300	1.2 ± 0.3	240
	$Au_{10}(SG)_{10}$	$BaLa_4Ti_4O_{15}$	0.1 wt%	Reduced pressure	300	0.9 ± 0.2	241
	$Au_{15}(SG)_{13}$					1.0 ± 0.2	
	$Au_{18}(SG)_{14}$					1.1 ± 0.2	
	$Au_{22}(SG)_{16}$					1.5 ± 0.4	
	$Au_{25}(SG)_{18}$					1.2 ± 0.3	
	$Au_{29}(SG)_{20}$					1.6 ± 0.4	
	$Au_{33}(SG)_{22}$					1.7 ± 0.5	
	$Au_{39}(SG)_{24}$					1.5 ± 0.3	
	$Au_{25}(SG)_{18}$	$SrTiO_3$	0.1 wt%	Reduced pressure	300	1.0 ± 0.2	242
	$Au_{25}(SG)_{18}$	Cr_2O_3-$BaLa_4Ti_4O_{15}$	0.1 wt%	Reduced pressure	300	1.1 ± 0.2	243
	$Au_{25}(PET)_{18}$ $Au_{24}Pt(PET)_{18}$	$BaLa_4Ti_4O_{15}$	~0.1 wt%	Reduced pressure	300	—[c]	244
	$Rh_2(SG)_2$	$BaLa_4Ti_4O_{15}$	0.09 wt%	Reduced pressure	300	1.3 ± 0.3	245
	$Ag_{25}(2,4\text{-}SPhMe_2)_{18}$ $Ag_{24}Pt(2,4\text{-}SPhMe_2)_{18}$	g-C_3N_4	0.2 wt%	Ar	150	1.5 ± 0.3	200
Electrocatalytic HER and OER	$Pd_6(SC12)_{12}$	AC	—[c]	Vacuum	200	—[c]	246
	$Au_2Pd_6S_4(PPh_3)_4(SPhF_2)_6$	MoS_2	0.05 wt%	Ar	100	—[c]	180
	$Au_{25}(PET)_{18}$	$CoSe_2$	~0.2 mg cm^{-2}	N_2	300	—[c]	247

[a] Counter ion is omitted. [b] Reference number. [c] No information.

In 2012, the same group studied the use of $Au_{25}(SC12)_{18}$ (Fig. 2B) and $Au_{24}Pd(SC12)_{18}$ (Fig. 2C; SC12 = 1-dodecanethiolate) as metal NCs with multi-walled carbon nanotubes (MWCNTs) as a support.[209] In this study, the ligands were removed by calcination at 300 or 450 °C for 2 h under vacuum. In both cases, no aggregation was observed when the Au loading on the MWCNTs was less than 0.2 wt% (0.2 wt% Au). However, aggregation was clearly observed when the loading was greater than 0.2 wt% (Fig. 4A). This finding indicates that the optimization of the loading amount is very important to suppress the aggregation of the loaded metal NCs. The catalytic activity of the obtained catalysts (Au_{24}M/MWCNTs; M = Au or Pd) for the oxidation of benzyl alcohol was investigated, and the results showed that the catalytic activity appeared only after ligand elimination for these catalysts. Moreover, in this study, it was shown that the oxidation reaction proceeds using atmospheric molecular O_2 as an oxidant over these catalysts and that the catalytic activity of Au_{25}/MWCNTs can be improved by nearly three times by simply replacing one Au atom with Pd (Fig. 4B).

As described above, ligand elimination induces an increase in catalytic activity. In 2014, the same group reported that moderate amounts of the remaining ligands led to control of the reaction selectivity.[210] In that study, $Au_{25}(SC12)_{18}$ (Fig. 2B) was used as the metal NCs and hierarchically porous carbon nanosheets (HPCSs; Fig. 5A) were used as the support. HPCSs have a larger specific surface area than MWCNTs (Table 2) and have more defects on their surface because of their porous structure. Therefore, almost no aggregation of Au_{25} was observed for Au_{25}/HPCSs with 1.0 wt% Au even after calcination at 500 °C for 2 h. The study using the obtained catalysts revealed that (1) a part of the SRs could not be removed from the Au_{25} surface by the calcination below 500 °C and (2) the alkyl chains, once desorbed from the Au_{25} NC surfaces by S–C dissociation at low temperature, were adsorbed on the surfaces of the HPCSs. A study on the oxidation ability of benzyl alcohol for a series of catalysts prepared at different calcination temperatures revealed that (1) ligand elimination is necessary for the emergence of the catalytic activity of this catalyst, (2) the catalytic activity increases with the amount of ligand elimination, and (3) the catalyst with

Open Access Article. Published on 12 2021. Downloaded on 02.06.2026 12:22:59.
This article is licensed under a Creative Commons Attribution 3.0 Unported Licence.

Table 2 Properties of supports introduced in this review

Support	Surface area/m^2 g^{-1}	Lewis acid site	Brønsted acid site
SBA-15	866[a]	—[k]	—[k]
(m-SiO_2)	570 ± 5[b]		
	395.2[c]		
MWCNTs	250–300[d]	—[k]	Exist[r]
HPCSs	2300[e]	—[k]	—[k]
HAP	~100[f]	—[k]	—[k]
CeO_2	65[g]	Exist[s]	A little exist[s]
Al_2O_3	172[g]	Exist[s]	Absent[s]
TiO_2	48 (P-25)[g]	Exist[s]	A little exist[s]
	9.6 (anatase)[h]		
	50 (anatase)[i]		
	6.7 (rutile)[h]		
SiO_2	200 ± 25[j]	Exist[s]	Absent[s]
PGO	—[k]	—[k]	—[k]
AC	250–2410[lw]	—[k]	—[k]
CB	—[k]	—[k]	—[k]
Fe_2O_3	10[mw]	A little exist[t]	A little exist[t]
γ-Al_2O_3	403[mw]	Exist[u]	Absent[u]
ZnAl-HT	—[k]	—[k]	—[k]
$BaLa_4Ti_4O_{15}$	6.1[ow]	—[k]	—[k]
$SrTiO_3$	3–27[pw]	Exist[v]	Absent[v]
g-C_3N_4	43–288[qw]	—[k]	—[k]
MoS_2	—[k]	—[k]	—[k]
$CoSe_2$	—[k]	—[k]	—[k]

[a] Ref. 183. [b] Ref. 212. [c] Ref. 234. [d] Ref. 209. [e] Ref. 211. [f] Ref. 214. [g] Ref. 198. [h] Ref. 184. [i] Ref. 310. [j] Ref. 220. [k] No information. [l] Ref. 248. [m] Ref. 249. [n] Ref. 250. [o] Ref. 251. [p] Ref. 252. [q] Ref. 253. [r] Ref. 254. [s] Ref. 255. [t] Ref. 256. [u] Ref. 257. [v] Ref. 258. [w] General value.

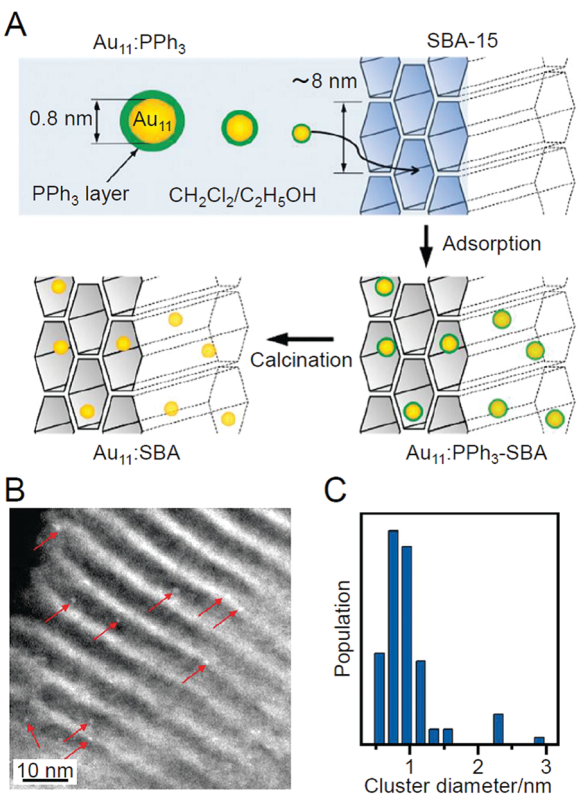
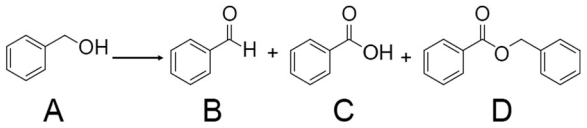


Fig. 3 (A) Synthesis procedure of sub-nanometer-sized Au NCs within SBA-15 using PPh_3-protected Au_{11} NCs as a precursor. (B) Representative HAADF-STEM image and (C) size distribution of Au NCs prepared by adsorption method. Reproduced with permission from ref. 183. Copyright 2009 American Chemical Society.



Scheme 1 Benzyl alcohol oxidation using metal NC catalysts. Generally, the reaction is conducted in the presence of a base such as cesium carbonate (Cs_2CO_3) or potassium carbonate (K_2CO_3). In the literature, the reaction was conducted with H_2O or toluene as a solvent under O_2 or air atmosphere. In ref. 183, H_2O_2 was used as an oxidant. A = benzyl alcohol, B = benzaldehyde, C = benzoic acid, D = benzyl benzoate, respectively.

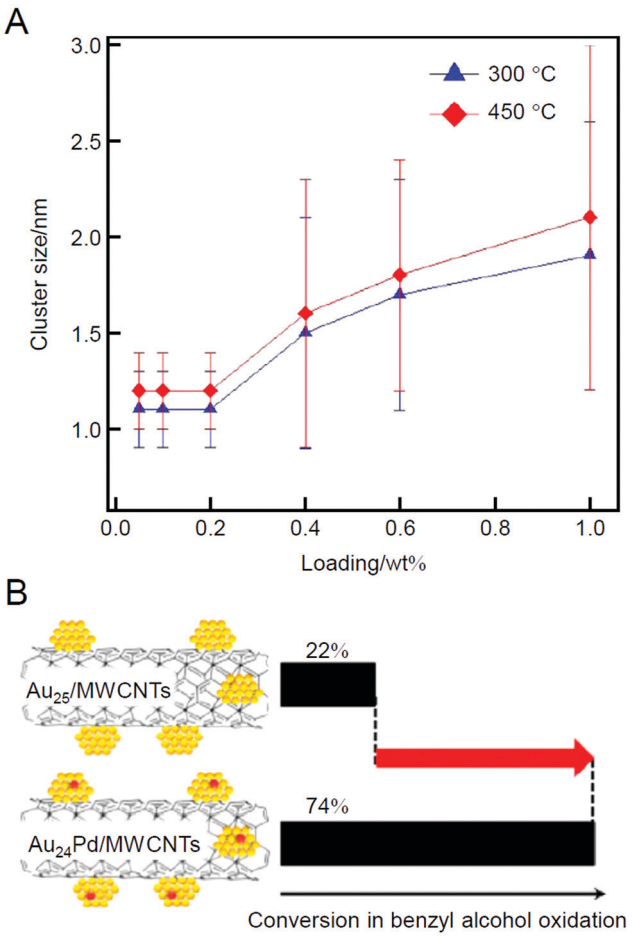


Fig. 4 (A) Dependence of the loading amounts of Au_{25} NCs on the Au particle size in Au_{25}/MWCNTs. The error bars indicate the size distribution determined by TEM. (B) Catalytic performances of Au_{25}/MWCNTs and $Au_{24}Pd$/MWCNTs for benzyl alcohol oxidation. Reproduced with permission from ref. 209. Copyright 2012 American Chemical Society.

remaining partial ligands had the highest selectivity for the conversion to benzaldehyde (Scheme 1B) (Fig. 5B). This study was of great interest as it showed that the reaction selectivity can be controlled by controlling the amount of remaining ligands. In 2016, the same group used a series of Au_n NCs (Au_{25}, Au_{38}, Au_{144}, or $Au_{\sim 330}$) to study the size dependence of Au NCs on this catalytic reaction, and the results revealed that Au_{144} shows the highest conversion efficiency.[211]

This journal is © The Royal Society of Chemistry 2021

Open Access Article. Published on 12 2021. Downloaded on 02.06.2026 12:22:59.
This article is licensed under a Creative Commons Attribution 3.0 Unported Licence.

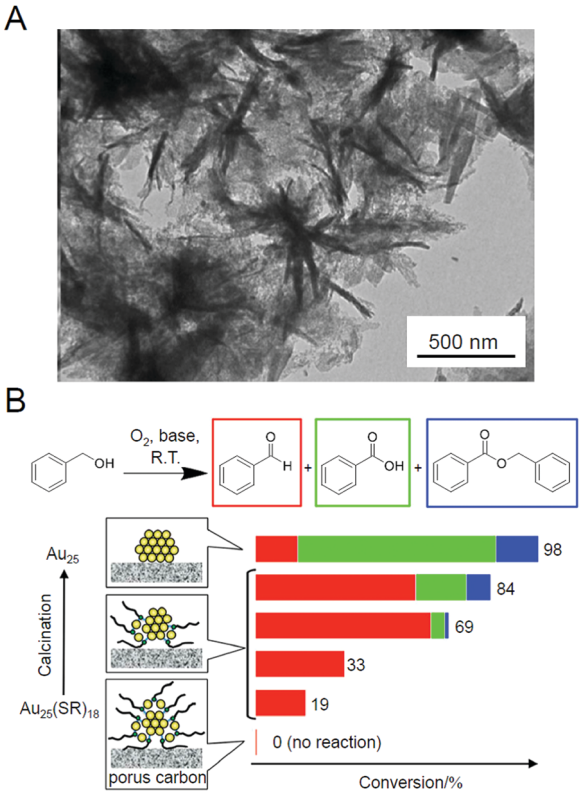


Fig. 5 (A) TEM image of HPCSs. (B) Catalytic performance of $Au_{25}(SC12)_{18-x}$/HPCSs for aerobic oxidation of benzyl alcohol. Reproduced with permission from ref. 210. Copyright 2014 American Chemical Society.

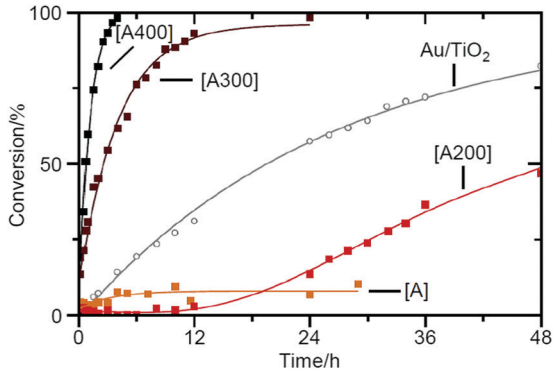
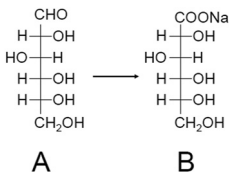


Fig. 6 Kinetic survey of benzyl alcohol dehydrogenation over Au_{25}/SBA-15 materials (1.07 wt% Au) as-synthesized [A] (orange) and calcined at 200 °C [A200] (red), 300 °C [A300] (brown), and 400 °C [A400] (black) and comparison data obtained for Au/TiO_2 (gray) (reference from the World Gold Council). Reproduced with permission from ref. 212. Copyright 2015 Elsevier.



Scheme 2 Glucose oxidation to gluconic acid using metal NC catalysts. The reaction was conducted under O_2 atmosphere in NaOH solution kept at pH 9.5 in ref. 213. A = glucose, B = gluconic acid.

Regarding benzyl alcohol oxidation, Zheng *et al.* also reported results in 2013.[128] In their study, the newly synthesized $Au_{13}Cu_8(PPh_2Py)_{12}$ (PPh_2Py = diphenyl-2-pyridylphosphine) was loaded on CNTs, and then the catalysts were calcined at 370 °C under vacuum to prepare $Au_{13}Cu_8$/CNTs without ligand. The $Au_{13}Cu_8$/CNTs showed 46.9% conversion efficiency and 61.0% selectivity to benzaldehyde under O_2 atmosphere at 80 °C. This catalyst resulted in a conversion efficiency of benzyl alcohol that was 33.2% higher than that for Au_{25}/CNTs under the same reaction conditions, demonstrating the effectiveness of alloying in improving the conversion.

In addition to these studies, in 2015, Tuel *et al.* conducted a study using $Au_{25}(SPh\text{-}pNH_2)_{17}$ (SPh-pNH_2 = 4-aminothiophenolate)[259] as a metal NC, whose geometrical structure has not been revealed to date, and SBA-15 as a support.[212] On the basis of the TGA results of unsupported $Au_{25}(SPh\text{-}pNH_2)_{17}$, they judged that calcination for 12 h at 400 °C was necessary to completely remove the ligands from this catalyst. In the TEM images of the catalysts with 0.04 or 1.07 wt% Au, particles with an average size of 1.8–1.9 nm were observed. Because this particle size is larger than that observed in the TEM image of $Au_{25}(SPh\text{-}pNH_2)_{17}$ (0.8 ± 0.2 nm), it is assumed that the aggregation of Au NCs was not completely suppressed in this experiment. The authors investigated the catalytic activity of the catalysts for the conversion of benzyl alcohol to benzaldehyde (Scheme 1B). The results revealed that uncalcined $Au_{25}(SPh\text{-}pNH_2)_{17}$/SBA-15 exhibited little catalytic activity for the oxidative dehydrogenation reaction using a strong base and that the catalytic activity increased continuously with the calcination temperature (Fig. 6). These findings indicate that it is crucial to eliminate ligand for proceeding this reaction (oxidative dehydrogenation reaction using a strong base). In contrast, for radical reactions using strong oxidants, uncalcined $Au_{25}(SPh\text{-}pNH_2)_{17}$/SBA-15 showed catalytic activity; however, calcination led to a decrease in the catalytic activity. This result indicates that the effectiveness of ligand elimination depends on the proceeding reaction mechanism.

As described above, benzyl alcohol is often used as a reactant for alcohol oxidation. Li and Huang *et al.* investigated glucose oxidation (Scheme 2) in 2017.[213] The products, gluconic acid and its salts, are widely used as additives in foods, beverages, and pharmaceuticals. Currently, microbiota and Pd-bismuth (Bi) alloys are used as catalysts for the glucose oxidation; however, the catalysts must be produced with higher activity and fewer purification processes to save resources and energy and achieve low environmental impact. The authors found that calcination of $Au_{38}(PET)_{24}$/AC (Fig. 2D; AC = activated carbon) at 120 °C removes a part of the ligands, and the obtained catalyst (Au_{38}/AC-120) showed higher catalytic activity than conventional catalysts such as Pd/AC, Pd-Bi/AC, and Au/AC (Fig. 7). For this reaction, the conversion efficiency decreased when all the ligands were removed from $Au_{38}(PET)_{24}$ by calcination at high temperature. In general, ligand removal induces structural change of metal NCs.[244] This result implies that it is very important to maintain

Open Access Article. Published on 12 2021. Downloaded on 02.06.2026 12:22:59.
This article is licensed under a Creative Commons Attribution 3.0 Unported Licence.

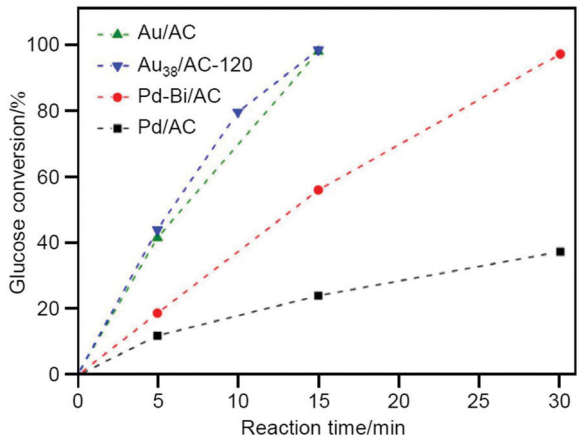


Fig. 7 Glucose conversion *vs.* time over Pd/AC, Pd-Bi/AC, Au/AC, and Au_{38}/AC-120. Reproduced with permission from ref. 213. Copyright 2017 Wiley-VCH.

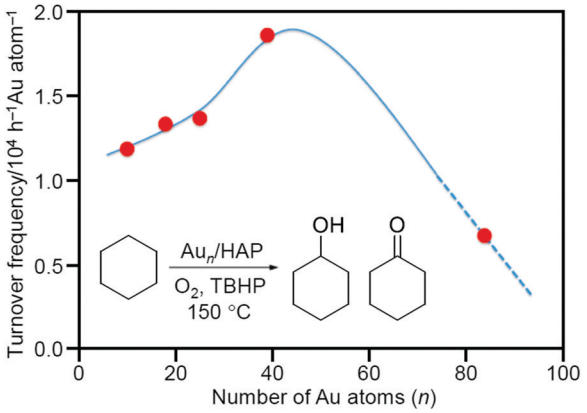
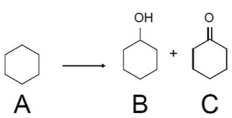


Fig. 8 Turnover frequency values as a function of the number of Au atoms, *n*. The curve is a guide for the eye. Reproduced with permission from ref. 214. Copyright 2011 American Chemical Society.

the geometrical and/or electronic structure of the precursor $Au_{38}(PET)_{24}$ for this catalytic reaction to proceed.

2.1.2. Hydrocarbon oxidation. The synthesis of a mixture of cyclohexanol and cyclohexanone (KA oil) by cyclohexane oxidation (Scheme 3)[214,215,217,218,260,261] is an important process for nylon production, and the annual production in the world is currently more than 6 million tons. At present, KA oil is produced using a large amount of energy under high temperature and pressure, and the current process uses an oxidation reaction in which improvement of the selectivity is difficult. Therefore, it is expected that a catalyst capable of synthesizing KA oil with both higher selectivity and yield under mild conditions is needed to be developed in the future.

In 2011, Tsukuda *et al.* prepared a Au_n/HAP catalyst using $Au_n(SG)_m$ (SG = glutathionate; n = 10, 18, 25, or 39) as metal NCs and hydroxyapatite (HAP) as a support.[214] In this experiment, the ligands were removed by calcination under vacuum at 300 °C for 2 h. The complete elimination of the ligands was confirmed by inductively coupled plasma (ICP) analysis. In this study, the aggregation of Au_n NCs on the support was suppressed by the following factors: (1) HAP with a large specific surface area (Table 2) was used as a support; (2) the loading amount was suppressed to 0.2 wt% Au; and (3) $Au_n(SG)_m$ NCs were adsorbed in solution at pH where charge repulsion between the metal NCs



Scheme 3 Cyclohexane oxidation using metal NC catalysts. In this reaction, TBHP was essential to initiate the reaction,[259] suggesting that this oxidation proceeds *via* a complex radical chain mechanism.[260,261] The reaction was conducted without solvent under O_2 atmosphere in the literature.[214,215,217,218] A = cyclohexane, B = cyclohexanol, C = cyclohexanone. Products B and C are called KA-oil. In ref. 214, cyclohexyl-*t*-butyl peroxide, which is an intermediate, and cyclohexanethiol were also produced (the latter was produced by the reaction between the reactant and the sulfur remaining on the support).

was likely to occur. Each of the obtained Au_n/HAP proceeded the oxidation reaction from cyclohexane to KA oil with a selectivity of more than 99%. A comparison of the catalytic activity of a series of the catalysts including Au ~ 85/HAP prepared by another method showed that Au_n/HAP shows the highest conversion efficiency for cyclohexane oxidation in the n range of 40–80 (Fig. 8).

Based on the results obtained by Tsukuda *et al.*, Barrabés and Bürgi *et al.* prepared Au_{38}/CeO_2 and Au_{38}/Al_2O_3 (Al_2O_3 = aluminum oxide) using $Au_{38}(PET)_{24}$ (Fig. 2D) as a metal NC in 2015.[215] They tracked the details of the calcination mechanism using TGA and temperature-programmed desorption/mass spectrometry (TPD/MS). Their results clarified that the SR-desorption process differed depending on the calcination atmosphere and the support. It was also shown that SR desorption occurred with two steps for both catalysts (Fig. 9A). X-ray absorption fine structure (XAFS) analysis revealed that ligands were removed at 250 °C for both catalysts. Both catalysts showed catalytic activity for the cyclohexane oxidation. Because the catalysts after calcination exhibited higher catalytic activity than those before calcination, the removal of the ligands was considered effective for improvement of the catalytic activity in these catalysts. Between the two, Au_{38}/CeO_2 showed higher activity. In Au_{38}/CeO_2, Au became cationic, which seems to induce high activity. In this study, cyclohexanethiol was also produced (Fig. 9B), suggesting that the loaded Au NCs also promoted the reaction between the cyclohexane and residual SR (or sulfur (S)).

Barrabés and Bürgi *et al.* tracked the SR-desorption process during calcination under O_2 atmosphere in more detail using X-ray absorption near edge structure (XANES; Fig. 10A) analysis and X-ray photoelectron spectroscopy (XPS) in 2018.[216] They observed that the S, which was desorbed from Au_{38} NCs, was adsorbed on a support (CeO_2 or Al_2O_3) in the vicinity of the Au_{38} NCs (Fig. 10B), and the desorbed S was oxidized in the order of SR, SO_3^{2-}, and SO_4^{2-} with increasing temperature. The S and oxidized S on the support have the following possibilities: (1) react directly with the substrate to produce by-products; (2) become a poison that suppresses the charge transfer

 This journal is © The Royal Society of Chemistry 2021

Open Access Article. Published on 12 2021. Downloaded on 02.06.2026 12:22:59.
This article is licensed under a Creative Commons Attribution 3.0 Unported Licence.

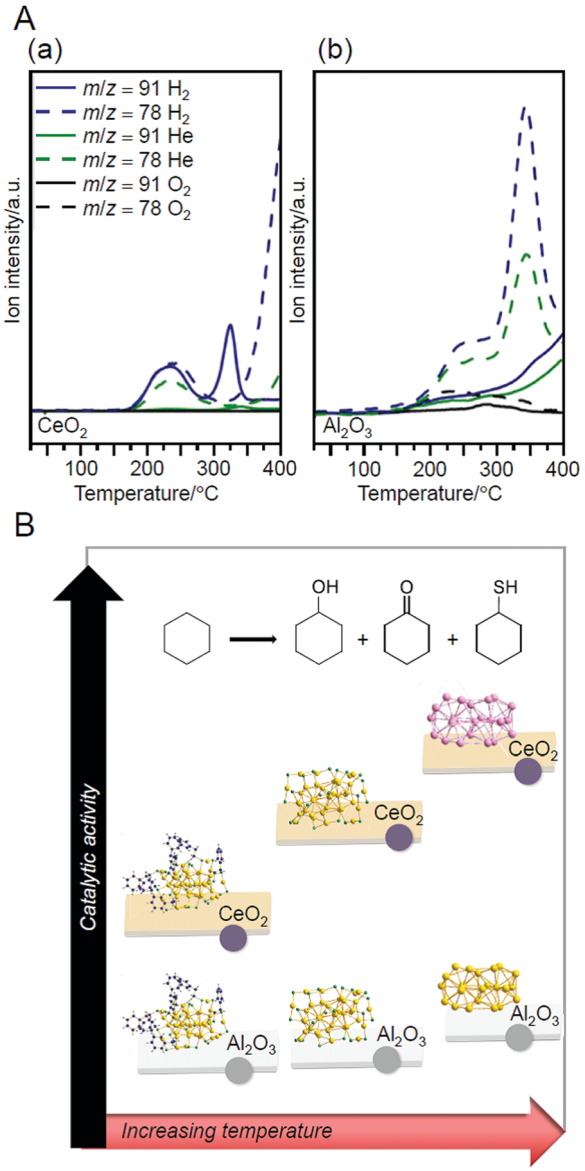


Fig. 9 (A) Desorption of each compound from (a) $Au_{38}(PET)_{24}/CeO_2$ and (b) $Au_{38}(PET)_{24}/Al_2O_3$ under different atmospheres at a heating rate of 10 °C min^{-1}, obtained by TPD/MS. The compounds with m/z = 91 and 78 are originated from SC_8H_9 and C_6H_5, respectively. (B) Relation between the catalytic activity of each catalyst for aerobic oxidation of cyclohexane and the treatment temperature. Reproduced with permission from ref. 215. Copyright 2015 American Chemical Society.

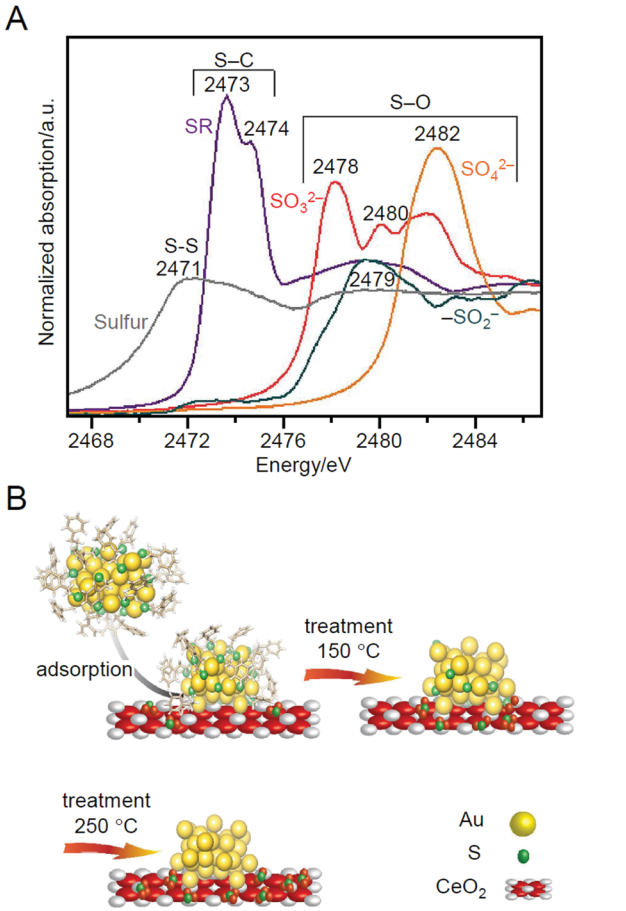


Fig. 10 (A) XANES spectra at S K-edge of different reference materials. (B) Schematic of thiolate ligands evolution upon NC deposition on CeO_2 and oxidative treatments. Reproduced from ref. 216. Copyright 2018 Wiley-VCH.

between the support and metal; or (3) change the electron density of the support and thereby affect the catalytic properties. This study is significant because it clearly demonstrates that these possibilities should also be considered in the creation of heterogeneous catalysts based on the calcination of $Au_n(SR)_m$ NCs/metal oxides. In their study in 2019, they revealed by multiple spectroscopies that S on these supports was involved in the reaction to produce the aforementioned cyclohexanethiol.[217]

In 2019, Barrabés *et al.* used two types of metal NCs, $Au_{25}(PET)_{18}$ and $Au_{144}(PET)_{60}$ (Fig. 2E), and two types of supports, titanium dioxide (TiO_2) and silicon dioxide (SiO_2), to study the effect of the size of Au_n NCs and the type of the support on the catalytic activity.[218] In this study, first, it was revealed by TGA that the ligand elimination starts at 150 °C and almost all the ligands could be removed at 250 °C for the catalysts prepared using all the combinations. However, calcination at 250 °C resulted in significant aggregation of metal NCs. Therefore, $Au_{25}(PET)_{18-x}/TiO_2$, $Au_{144}(PET)_{60-x}/TiO_2$, $Au_{25}(PET)_{18-x}/SiO_2$, and $Au_{144}(PET)_{60-x}/SiO_2$ prepared by the partial ligand removal by calcination at 150 °C under air were used as catalysts for the catalysis test. As for the size effect, it was clarified that $Au_{144}(PET)_{60-x}$ showed about two times higher conversion efficiency than $Au_{25}(PET)_{18-x}$ for both supports (Fig. 11). The difference in the conversion efficiency was interpreted to be caused by the difference in the adsorption efficiency of the substrate, activation of molecular O_2, and other factors. For the support effect, SiO_2 showed higher activity for the conversion efficiency of cyclohexane, whereas TiO_2 showed higher values for the selectivity of KA oil production (Fig. 11). It was interpreted that this difference was caused by the different reaction mechanism depending on the support.

2.1.3. Epoxidation of alkenes. This reaction (Scheme 4)[219–224] is a type of oxidation reaction, and in a laboratory, organic peracids such as *m*-chloroperbenzoic acid and peracetic acid are used as oxidants. However, from the viewpoint of environmental harmony

Open Access Article. Published on 12 2021. Downloaded on 02.06.2026 12:22:59.
This article is licensed under a Creative Commons Attribution 3.0 Unported Licence.

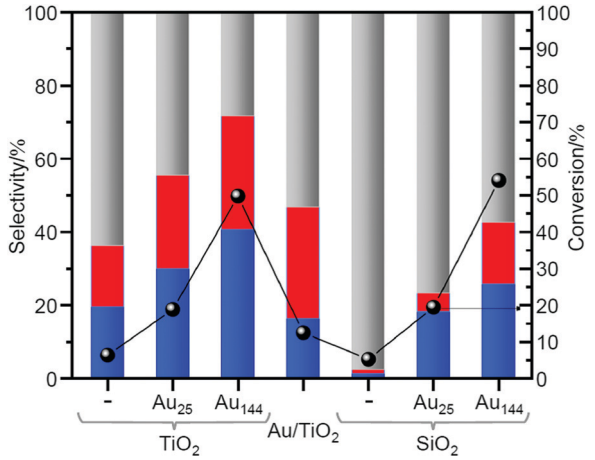
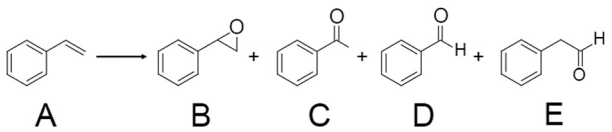


Fig. 11 Catalytic activity of loaded Au_{25} and Au_{144} NCs (pre-treated at 150 °C) in cyclohexane oxidation. Cyclohexane conversion normalized to the Au loading (except for the blank measurements) (right axis); product distribution (left axis): red, blue, and gray represent cyclohexanol, cyclohexanone, and by-products, respectively. Reproduced with permission from ref. 218. Copyright 2019 Elsevier.



Scheme 4 Styrene oxidation using metal NC catalysts. In this reaction, typically, TBHP is used as an oxidant because it is known to be more effective than O_2 for alkene oxidations.[219] The reaction was conducted in toluene or acetonitrile in the literature.[219–224] A = styrene, B = styrene oxide, C = acetophenone, D = benzaldehyde, E = 3-phenylpropionic acid. In ref. 219, by-products such as benzoic acid and benzyl alcohol are also produced.

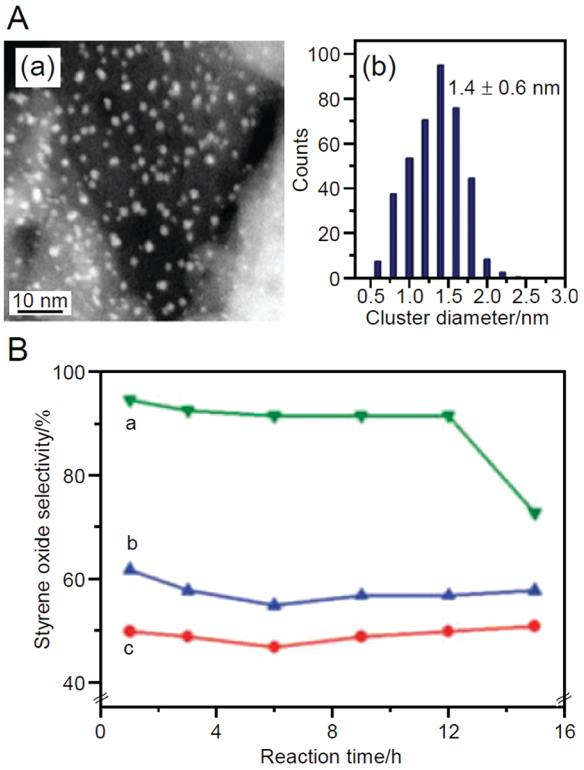


Fig. 12 (A) (a) Representative HAADF-STEM image of Au_{25}/HAP (0.5 wt% Au) and (b) size distribution of the Au NCs. (B) Selectivity of styrene oxide for (a) Au_{25}/HAP (0.5 wt% Au), (b) Au_{NP}/HAP (0.5 wt% Au) prepared by adsorption of $HAuCl_4$, and (c) Au_{NP}/HAP (0.5 wt% Au) prepared by impregnation method. Reproduced with permission from ref. 219. Copyright 2010 Royal Society of Chemistry.

and cost, it is expected that molecular O_2, which is abundant in the atmosphere, will be used as an oxidant for this oxidation reaction. Styrene oxide (Scheme 4B), obtained by the styrene oxidation, is a useful chemical used as a precursor in the syntheses of insecticides, cosmetics, surface coatings, and many pesticides. Benzaldehyde (Scheme 4D) is an aromatic component of almonds and apricots (apricot seeds) and is used as an inexpensive flavoring agent.

In 2010, Tsukuda *et al.* prepared catalysts using $Au_{25}(SG)_{18}$ as the metal NCs and HAP as the support.[219] The ligands were completely removed by calcination at 300 °C for 2 h under vacuum. This calcination slightly increased the particle size on the support from 1.0 ± 0.4 nm to 1.4 ± 0.6 nm (Fig. 12A). In the catalytic reaction, styrene oxidation was investigated using *tert*-butyl hydroperoxide (TBHP) as an oxidant, and the obtained catalyst showed 100% conversion and 92% styrene oxide (Scheme 4B) selectivity. This selectivity of the styrene oxides was higher than that of Au_{NP}/HAP loaded with larger Au_{NP} by adsorption or impregnation methods (Fig. 12B). Although the Au_{25}/HAP converted styrene to styrene oxide, the conversion ability to further oxidize the styrene oxide was low, leading to the high selectivity of styrene oxide. This study also reported preliminary results that the catalytic reaction proceeds with 22% conversion and 36% styrene oxide selectivity even using molecular O_2 as an oxidant when the reaction system was heated by microwave.

In 2010, Jin *et al.* studied the size and the support effects of catalysts using three different sizes of metal NCs ($Au_{25}(PET)_{18}$, $Au_{38}(PET)_{24}$, and $Au_{144}(PET)_{60}$) and two different supports (SiO_2 and HAP).[220] In this research, unlike in the work of Tsukuda *et al.*, only a part of the ligands was removed by calcination at 200 °C under vacuum. Such an elimination of a part of the ligands increased the conversion efficiency (the main product was benzaldehyde; Scheme 4D) for both combinations of catalysts (Fig. 13A). For example, in the reaction using TBHP as the initiator, molecular O_2 as the oxidant, and toluene as the solvent, the conversion efficiency increased with decreasing metal core size (Fig. 13B). It was interpreted that this phenomenon occurred because of the efficient activation of molecular O_2 by small Au NCs. As for the support, HAP was shown to be a more suitable support for high activation than SiO_2 (Fig. 13B). Unlike SiO_2, HAP had electronic interactions with the loaded Au NCs. In addition, HAP suppressed the aggregation of loaded Au NCs more than SiO_2. The higher conversion efficiency achieved when using HAP as the support rather than SiO_2 was attributed to these factors. Because the ligand was only partially removed in this study, the details of the reaction mechanism were discussed based on the geometrical structure of $Au_{25}(PET)_{18}$[42,262] which was determined by SC-XRD (Fig. 13C).

 This journal is © The Royal Society of Chemistry 2021

Open Access Article. Published on 12 2021. Downloaded on 02.06.2026 12:22:59.
This article is licensed under a Creative Commons Attribution 3.0 Unported Licence.

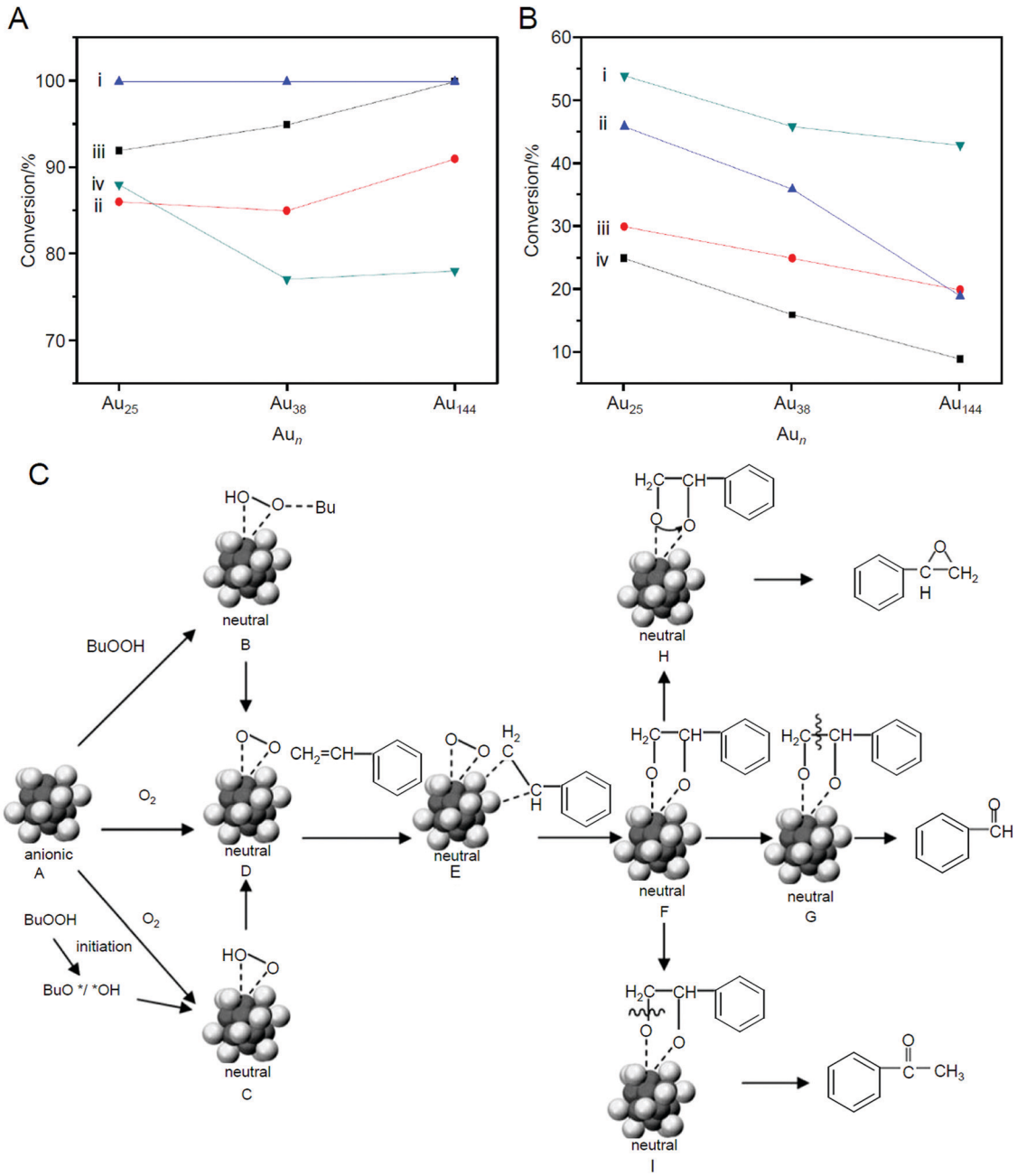


Fig. 13 (A) Catalytic result of styrene oxidation with TBHP as the oxidant on (i) calcined Au_n/HAP, (ii) uncalcined Au_n/HAP, (iii) calcined Au_n/SiO_2, and (iv) uncalcined Au_n/SiO_2 catalysts. (B) Catalytic result of styrene oxidation with TBHP as an initiator and O_2 as the main oxidant on (i) calcined Au_n/HAP, (ii) uncalcined Au_n/HAP, (iii) calcined Au_n/SiO_2, and (iv) uncalcined Au_n/SiO_2 catalysts. (C) Proposed mechanism of selective oxidation of styrene catalyzed by $Au_{25}(PET)_{18}$ NCs. For clarity, the PET ligands are not shown. Dark gray: Au atoms of the core, light gray: Au atoms of the shell. Reproduced with permission from ref. 220. Copyright 2010 Wiley-VCH.

In 2011, Jin *et al.* also conducted a study using $Au_{25}(PET)_{18}$ and $[Au_{25}(PPh_3)_{10}(PET)_5Cl_2]^{2+}$ (Fig. 2F) as metal NCs and CeO_2 as the support.[221] TBHP was used as the oxidant, and acetonitrile was used as the solvent, which is different from their study in 2010. As a result, styrene oxide (Scheme 4B) was obtained with high selectivity ($\geq$93%) using both catalysts. This result indicates that the type of solvent also greatly affects the selectivity of the product. $Au_{25}(PET)_{18}/CeO_2$ showed a higher conversion efficiency than $Au_{25}(PPh_3)_{10}(PET)_5Cl_2/CeO_2$, indicating that the metal core structure also has a significant effect on the activity. Calcination at 260 °C under vacuum resulted in a significant decrease in the activity, especially for $Au_{25}(PET)_{18}/CeO_2$. At this calcination temperature, all the ligands could be removed. In this case, the aggregation of metal NCs is likely to occur, and the cationic Au sites, which are easily attacked by the nucleophilic –CH=CH_2 group, disappear. It was interpreted that the activity significantly decreased in the calcination at 260 °C because of these factors. The authors speculated that the latter factor is also largely

Open Access Article. Published on 12 2021. Downloaded on 02.06.2026 12:22:59.
This article is licensed under a Creative Commons Attribution 3.0 Unported Licence.

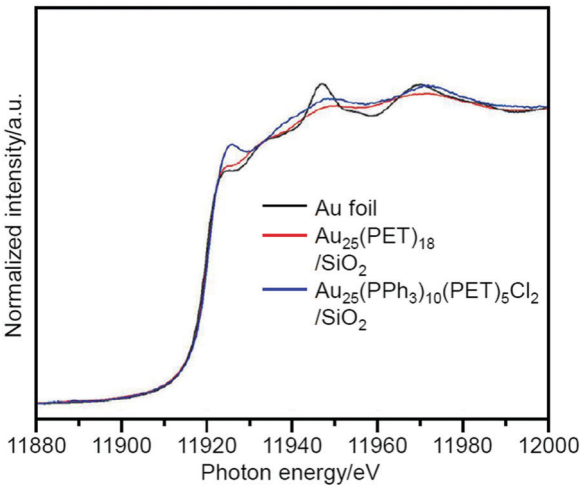


Fig. 14 Normalized Au L_3-edge XANES spectra of $Au_{25}(PET)_{18}/SiO_2$, $Au_{25}(PPh_3)_{10}(PET)_5Cl_2/SiO_2$, and Au foil. These spectra indicate that Au in $Au_{25}(PPh_3)_{10}(PET)_5Cl_2/SiO_2$ is more cationic than that in $Au_{25}(PET)_{18}/SiO_2$. Reproduced with permission from ref. 222. Copyright 2013 Wiley-VCH.

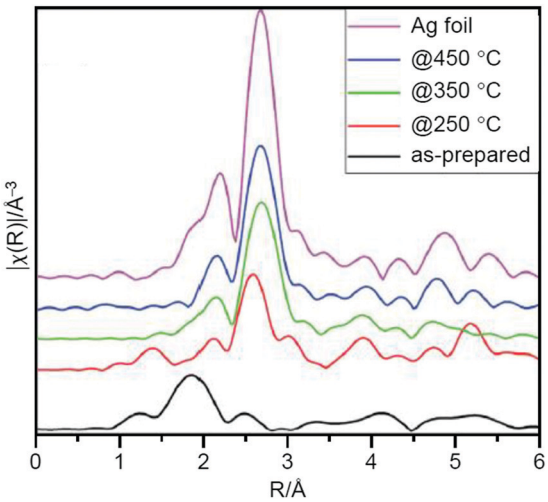


Fig. 15 Ag K-edge FT-EXAFS spectra in R-space for as-prepared and activated Ag_{25}/AC catalysts and Ag foil reference. Reproduced with permission from ref. 224. Copyright 2019 Royal Society of Chemistry.

involved in the higher conversion of $Au_{25}(PET)_{18}/CeO_2$ than $Au_{25}(PPh_3)_{10}(PET)_5Cl_2/CeO_2$. These results support their proposed reaction mechanism for this reaction (Fig. 13C).

Kumar *et al.* also studied a system similar to that of Jin *et al.* in 2013.[222] In their study, $Au_{25}(PET)_{18}$ or $Au_{25}(PPh_3)_{10}(PET)_5Cl_2$ was used as the metal NCs and SiO_2 was used as the support. TBHP and acetonitrile were used as the oxidant and solvent, respectively. In the catalysts before calcination, $Au_{25}(PET)_{18}/SiO_2$ showed high conversion efficiency, and $Au_{25}(PPh_3)_{10}(PET)_5Cl_2/SiO_2$ showed high selectivity for benzaldehyde (Scheme 4D). XANES (Fig. 14) and ultraviolet photoemission spectroscopy (UPS) demonstrated that Au in $Au_{25}(PPh_3)_{10}(PET)_5Cl_2/SiO_2$ is more cationic than Au in $Au_{25}(PET)_{18}/SiO_2$, which is interpreted to lead to the easy oxidation of styrene into benzaldehyde when using $Au_{25}(PPh_3)_{10}(PET)_5Cl_2/SiO_2$. In this study, the ligand removal was also conducted by calcination. This improved the conversion efficiency; however, the particle size of the metal NCs after calcination increased to ~3–4 nm.

Yan *et al.* conducted a more extensive study on the effect of the type of support on the particle size and catalytic activity of loaded metal NCs using $Au_{25}(MHA)_{18}$ (MHA = 6-mercaptohexanoic acid) and five different supports (HAP, TiO_2 (P-25), AC, pyrolyzed graphene oxide (PGO), and fused SiO_2) in 2015.[223] This work revealed that only the use of HAP and TiO_2 relatively suppressed the aggregation of Au_{25}. In Au_{25}/HAP, a strong interaction occurred between the phosphate ion (PO_4^{3-}) of HAP and Au. A strong interaction also occurred in Au_{25}/TiO_2. It was interpreted that the aggregation of Au_{25} was effectively suppressed on HAP and TiO_2 surfaces, unlike the surfaces on other supports, for these reasons. This study also suggested that ~50% of the S remained bound to Au when calcined at 300 °C under nitrogen (N_2) atmosphere. The obtained catalysts showed catalytic activity for styrene oxidation using TBHP as the oxidant; however, the conversion efficiency and the selectivity of styrene oxide (Scheme 4B) were comparable to those of the catalyst before calcination. In this study, the particle size slightly increased by calcination (from 1.5 to 2.4 nm).

In addition to these studies on Au NCs, Scott *et al.* conducted a study using $[Ag_{25}(2,4\text{-}SPhMe_2)_{18}]^-$ (2,4-$SPhMe_2$ = 2,4-dimethylbenzenethiolate; Fig. 2G) as a metal NC and AC as a support in 2019.[224] They prepared Ag_{25}/AC containing 4 wt% Ag by calcination at 250 °C under air. The TEM and XAFS (Fig. 15) measurements revealed that the Ag_{25} hardly aggregated and that most of the ligands were removed from the Ag_{25}. Quantitative analysis of the XPS spectrum suggested a residual of 0.55% S, which was interpreted to be transferred from the Ag_{25} surface onto the AC. When the calcination temperature was increased to 350 and 450 °C, the amount of S continuously decreased (0.14% at 350 °C and ~0.01% at 450 °C); however, there was significant aggregation of Ag_{25} in the catalysts. The catalysts prepared by calcination at 250 °C showed a conversion efficiency of 61.4% and 94% selectivity of styrene oxide (Scheme 4B) when TBHP was used as the oxidant. These values were higher than those of the catalyst before calcination, indicating that removal of the ligands by calcination led to improvement of the activity of the catalyst. Unfortunately, both the conversion efficiency and selectivity decreased when TBHP was used as the initiator and molecular O_2 was used as the oxidant. These issues are expected to be overcome in the future by improving the activity through modifications such as heteroatom substitutions.

2.1.4. CO oxidation. The CO oxidation reaction (Scheme 5) is a simple but important reaction in practical applications. For example, three-way catalysts (Pt, Pd, and rhodium (Rh)) play a role in promoting this reaction for removing CO from automotive exhaust gas. When the hydrogen (H_2) produced by steam reforming is used as a fuel for a polymer electrolyte fuel cell, if CO as a by-product is not removed, it will strongly adsorb on the surface of the Pt catalyst, resulting in a significant decrease in fuel cell performance. Prior purification through CO oxidation is necessary to prevent the decrease of fuel cell performance resulting from such catalyst poisoning by CO.

 This journal is © The Royal Society of Chemistry 2021

Open Access Article. Published on 12 2021. Downloaded on 02.06.2026 12:22:59.
This article is licensed under a Creative Commons Attribution 3.0 Unported Licence.

$$CO \longrightarrow CO_2$$

Scheme 5 CO oxidation using metal NC catalysts. The reaction was conducted while supplying reactant gas mixture containing of CO, O_2, and inert gas. Inclusion of water vapor in the feed gas has been shown to benefit the CO conversion.[226]

In this way, this reaction is a simple but important reaction and therefore often used as the model reaction to evaluate the catalytic activity of metal NCs and metal NPs. This is also the first catalysis for Au_{NP}, which was discovered by Haruta *et al.*[263]

In 2012, Spivey *et al.* conducted a study using $Au_{38}(SC12)_{24}$ as a metal NC and TiO_2 as a support.[225] In this study, the ligands were removed by calcination at 400 °C for 1 h under a mixture gas of H_2–helium (He). The catalytic activity for CO oxidation started to appear by removing ligands. However, unfortunately, remarkable aggregation of $Au_{38}(SC12)_{24}$ had already occurred when $Au_{38}(SC12)_{24}$ were adsorbed on the TiO_2 surface. Therefore, it was difficult to elucidate the catalytic activity of Au_{38}/TiO_2 for CO oxidation in this study.

In contrast, in the study by Jin *et al.* in 2012, the aggregation of metal NCs during adsorption was almost completely suppressed.[226] In this study, $Au_{25}(PET)_{18}$ was used as the metal NC and TiO_2, iron(III) oxide (Fe_2O_3), or CeO_2 was used as the support. Among these combinations, $Au_{25}(PET)_{18}/CeO_2$ showed the highest conversion efficiency. For this catalyst, high activity was induced by pre-treatment at 150 °C for 1.5 h under O_2 atmosphere (Fig. 16A). This temperature is lower than the temperature at which the ligand was removed (190 °C). Therefore, the authors described that high activity can be induced without the ligand elimination for this catalyst. On the basis of several experiments conducted under various conditions, it was suggested that (1) O_2 adsorbed onto CeO_2 could be activated by the pre-treatment and (2) the reaction occurred at the interface between $Au_{25}(PET)_{18}$ and CeO_2 (perimeter; Fig. 16B).

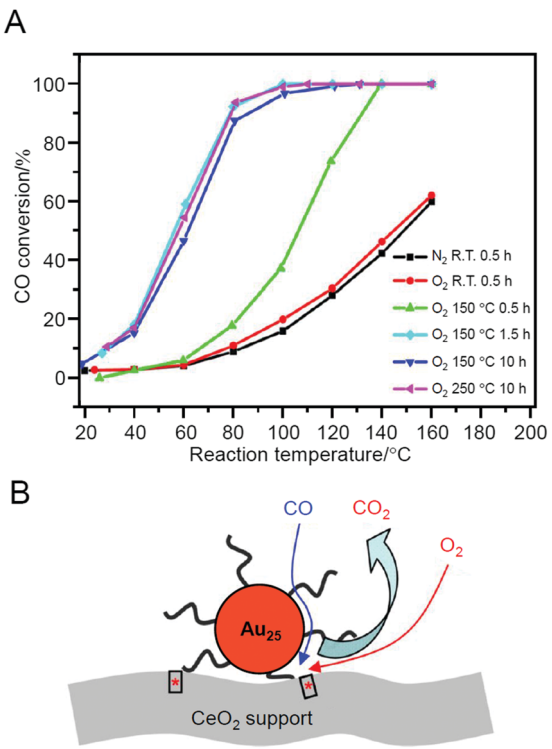


Fig. 16 (A) Reaction temperature dependence of CO conversion over $Au_{25}(PET)_{18}/CeO_2$ catalyst after different pre-treatments. Gas hourly space velocity (GHSV) = 7500 mL g^{-1} h^{-1}. (B) Proposed model for CO oxidation at the perimeter sites of $Au_{25}(PET)_{18}/CeO_2$ catalyst. Reproduced with permission from ref. 226. Copyright 2012 American Chemical Society.

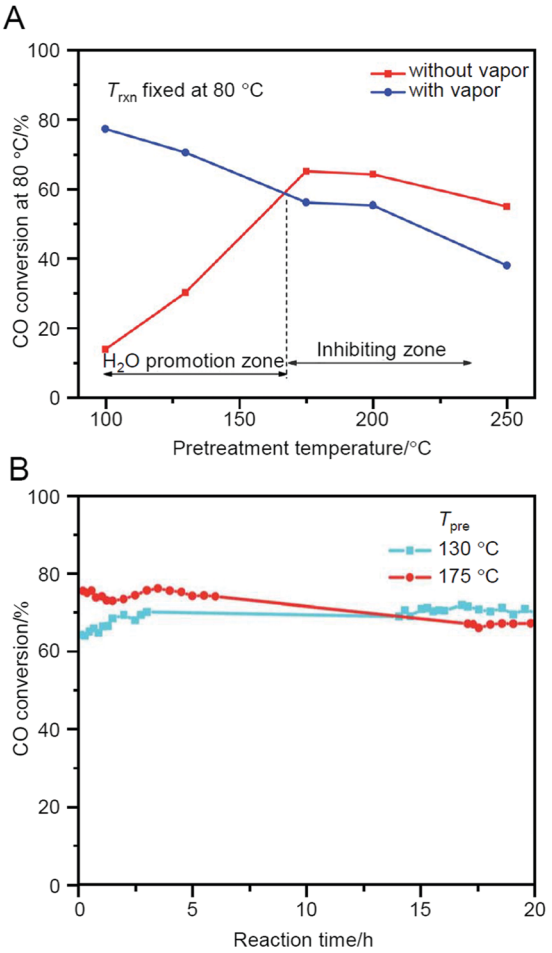


Fig. 17 (A) CO conversion at fixed reaction temperature (T_{rxn}) of 80 °C as a function of catalyst pre-treatment temperature for $Au_{38}(PET)_{24}/CeO_2$ catalyst. GHSV = 15 000 mL g^{-1} h^{-1}. (B) CO conversion at T_{rxn} = 100 °C over $Au_{38}(SR)_{24}/CeO_2$ catalyst as a function of reaction time. Pre-treatment conditions: O_2 for 2 h and pre-treatment temperature (T_{pre}) as shown in the figure. GHSV: 30 000 mL g^{-1} h^{-1}. Feed gas: without water vapor. Reproduced with permission from ref. 227. Copyright 2013 Royal Society of Chemistry.

Jin *et al.* also studied $Au_{38}(PET)_{24}/CeO_2$ in 2013[227] and demonstrated that $Au_{38}(PET)_{24}/CeO_2$ shows the highest activity when calcined at 175 °C (Fig. 17A). According to the TGA results, part of the ligands was interpreted to be removed in $Au_{38}(PET)_{24}/CeO_2$ during the calcination at this temperature. However, the conversion efficiency of this sample after 20 h of reaction was inverted by the sample prepared by calcination at 130 °C (namely, without the ligand elimination) (Fig. 17B). This finding indicates that the protection by ligands is very important for the preparation

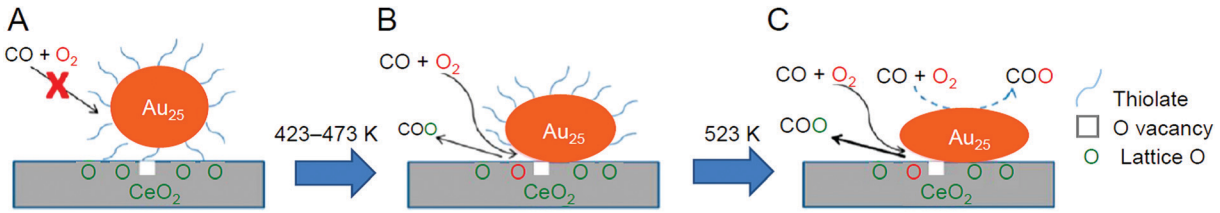


Fig. 18 CO oxidation mechanism on (A) intact, (B) partially dethiolated, and (C) fully dethiolated $Au_{25}(PET)_{18}/CeO_2$ catalysts. Reproduced with permission from ref. 231. Copyright 2014 American Chemical Society.

Open Access Article. Published on 12 2021. Downloaded on 02.06.2026 12:22:59.
This article is licensed under a Creative Commons Attribution 3.0 Unported Licence.

of highly stable catalysts. Thus, this study revealed the following two factors for the preparation of $Au_{38}(PET)_{24}/CeO_2$ catalyst that promote CO oxidation: (1) pre-treatment (calcination) under O_2 atmosphere is necessary for the activation; and (2) however, it is more appropriate not to completely remove the ligands from the viewpoint of stability. In their study in 2016, it was shown that when $Au_{144}(PET)_{60}/CeO_2$ was used as a catalyst, the inclusion of a reductive gas (H_2 or CO) along with O_2 further improved the effect of the pre-treatment.[228] Furthermore, their study in 2018 revealed that the catalytic activity of $Au_n(SR)_m/CeO_2$ (n = 25, 36, or 38) decreases overall with the bulkiness of the functional groups directly attached to S.[229] In addition to these facts, Jin *et al.* also demonstrated that both the ligand and metal core structures affect the catalytic activity by comparing the catalytic activity of $Au_{28}(S\text{-}c\text{-}C_6H_{11})_{20}$ ($S\text{-}c\text{-}C_6H_{11}$ = cyclohexanethiolate) and $Au_{28}(TBBT)_{20}$ (TBBT = 4-*tert*-butylbenzenethiolate).[230]

Wu and Overbury *et al.* performed a detailed investigation of the reaction mechanism for $Au_{25}(PET)_{18}/CeO_2$ in 2014 (Fig. 18).[231] They showed that (1) CO could not be adsorbed on the catalyst without pre-treatment and (2) after pre-treatment at 150 °C or higher under O_2 atmosphere, the PET existed at the interface between $Au_{25}(PET)_{18}$ and CeO_2 started to desorb ($Au_{25}(PET)_{18-x}/CeO_2$), and CO could be adsorbed on the exposed Au. The presence of such exposed Au was interpreted to begin to generate catalytic activity for CO oxidation at low temperature. Regarding the mechanism, it was revealed that when $Au_{25}(PET)_{18-x}/CeO_2$ was used as a catalyst, the reaction proceeds mainly by the Mars–van Krevelen mechanism (reduction mechanism), in which CO activated by $Au_{25}(PET)_{18-x}$ reacts with the oxygen in CeO_2 to produce CO_2, and O_2 in the gas phase compensates for the oxygen in CeO_2 (Fig. 18B). In addition, it was suggested that when the catalyst with the ligands further removed (Au_{25}/CeO_2) is used, the Langmuir–Hinshelwood mechanism, in which CO and O_2 react on the Au_{25} surface to produce CO_2, also occurred in parallel to the Mars–Van Krevelen mechanism (Fig. 18C). To further reinforce this interpretation, in 2016, Wu *et al.* conducted a study using $Au_{22}(L8)_6$ (L8 = 1,8-bis(diphenylphosphino)octane; Fig. 2H),[176] which contains coordinatively unsaturated Au, as a metal NC. As a result, it was confirmed that $Au_{22}(L8)_6$/metal oxide (TiO_2, SiO_2, or CeO_2) promotes CO oxidation at room temperature without pre-treatment.[232]

Thus, many catalysts require pre-treatment at an appropriate temperature. In 2020, Barrabés *et al.* tracked the phenomena occurring during the pre-treatment of $Au_{38}(PET)_{24}/CeO_2$ at 150 °C using *in situ* XAFS.[233] The results suggested that although S remained on Au, the staple structure ($Au_n(SR)_{n+1}$; n = 1 or 2)

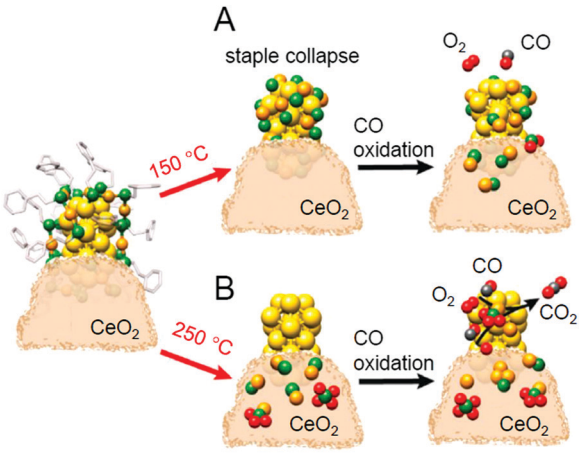


Fig. 19 Evolution of $Au_{38}(PET)_{24}/CeO_2$ catalyst structure estimated from EXAFS analyses: catalysts after pre-treatment at (A) 150 °C and (B) 250 °C and subsequent CO oxidation. Reproduced with permission from ref. 233. Copyright 2020 American Chemical Society.

surrounding the Au_{23} core (Fig. 2D) collapses with pre-treatment at 150 °C (Fig. 19A). This study also showed that Au NCs on the support change during CO oxidation reaction, which led to the adsorption of compounds with Au–S bonds on CeO_2, which are eventually oxidized to SO_3^{2-} and SO_4^{2-}. They also reported that increasing the pre-treatment temperature to 250 °C causes the complete removal of the ligands from the Au NCs, resulting in higher activity than that of the catalyst pre-treated at 150 °C (Fig. 19B). These results have led to new information on the structural changes induced by pre-treatment. However, the effect of the pre-treatment on the catalytic activity was not completely consistent with that reported by Jin *et al.* and Wu *et al.*; a deeper understanding of this difference is expected to be attained in future study.

Thus, when CeO_2 is used as a support, the aggregation of metal NCs is suppressed and high activation is induced. In 2012, Dai and Fan *et al.* reported the use of CuO-EP-FDU-12 or Co_3O_4-EP-FDU-12, in which the surface of mesoporous silica (EP-FDU-12) is modified with nanostructures of copper oxide (CuO) or cobalt oxide (Co_3O_4), as a support, resulting in the production of catalysts with very high stability.[234] They prepared Au_{144}/CuO-EP-FDU-12 or Au_{25}/Co_3O_4-EP-FDU-12 by adsorbing $Au_{144}(PET)_{60}$ onto CuO-EP-FDU-12 or $Au_{25}(PET)_{18}$ onto Co_3O_4-EP-FDU-12, followed by calcination at 300 °C under air. It was shown that such calcination removed the ligands; however, only slight aggregation of Au_{144} (Fig. 20) or Au_{25} occurred on the

 This journal is © The Royal Society of Chemistry 2021

Open Access Article. Published on 12 2021. Downloaded on 02.06.2026 12:22:59.
This article is licensed under a Creative Commons Attribution 3.0 Unported Licence.

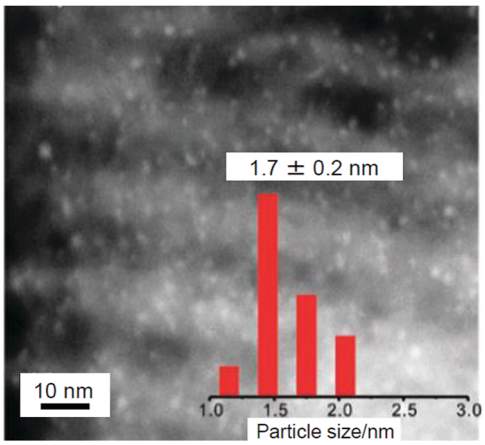


Fig. 20 STEM image of Au_{144} NCs (1.1 wt% Au) loaded on CuO-EP-FDU-12 after calcination at 300 °C and size distribution of Au NCs. Reproduced with permission from ref. 234. Copyright 2012 Royal Society of Chemistry.

support. Au NCs on silica tend to aggregate because Au NCs and silica have a weak interaction with each other. However, in their structures, the transition metal nanostructures (CuO or Co_3O_4) are strongly immobilized on the silica pore surface. It was interpreted that the aggregation of Au NCs was suppressed in Au_{144}/CuO-EP-FDU-12 and Au_{25}/Co_3O_4-EP-FDU-12 because these transition metal nanostructures strongly fix Au NCs on their surfaces. Both of the obtained catalysts exhibited high activity for CO oxidation. Because the catalyst without calcination showed little activity, it was concluded that calcination is essential for inducing catalytic activity for these catalysts.

In addition to these studies using atomically precise Au NCs, there have been examples using atomically precise Pt NCs. Negishi and Nagaoka *et al.* reported on the use of Pt_{17}/γ-Al_2O_3 as a catalyst for CO oxidation in 2020.[235] Pt is widely used as a catalyst for exhaust-gas purification; however, because Pt is a rare and expensive metal, reduction of its use through miniaturization is required. Nair and Negishi *et al.* found an easy method to synthesize Pt_{17} NCs protected by CO and PPh_3 ($[Pt_{17}(CO)_{12}(PPh_3)_8]Cl_n$; n = 1, 2; Fig. 2I) in 2017.[177] In their synthesis method, $Pt_n(CO)_m(PPh_3)_l$ NCs, in which $[Pt_{17}(CO)_{12}(PPh_3)_8]Cl_n$ was the main product, were first prepared by mixing the reagents and heating the solvent under air atmosphere. $[Pt_{17}(CO)_{12}(PPh_3)_8]Cl_n$ was isolated from the obtained mixture in high purity using the difference in solubility in the solvent. This method has the advantage that precise Pt NCs can be synthesized without any special synthesis equipment[264] or ligands.[265,266] In their study in 2020, $[Pt_{17}(CO)_{12}(PPh_3)_8]Cl_n$ was first adsorbed on γ-Al_2O_3 ($(Pt_{17}(CO)_{12}(PPh_3)_8/\gamma$-$Al_2O_3$), which was then calcined at 500 °C to obtain Pt_{17}/γ-Al_2O_3 (Fig. 21A). Pt_{17} NCs hardly aggregated in the

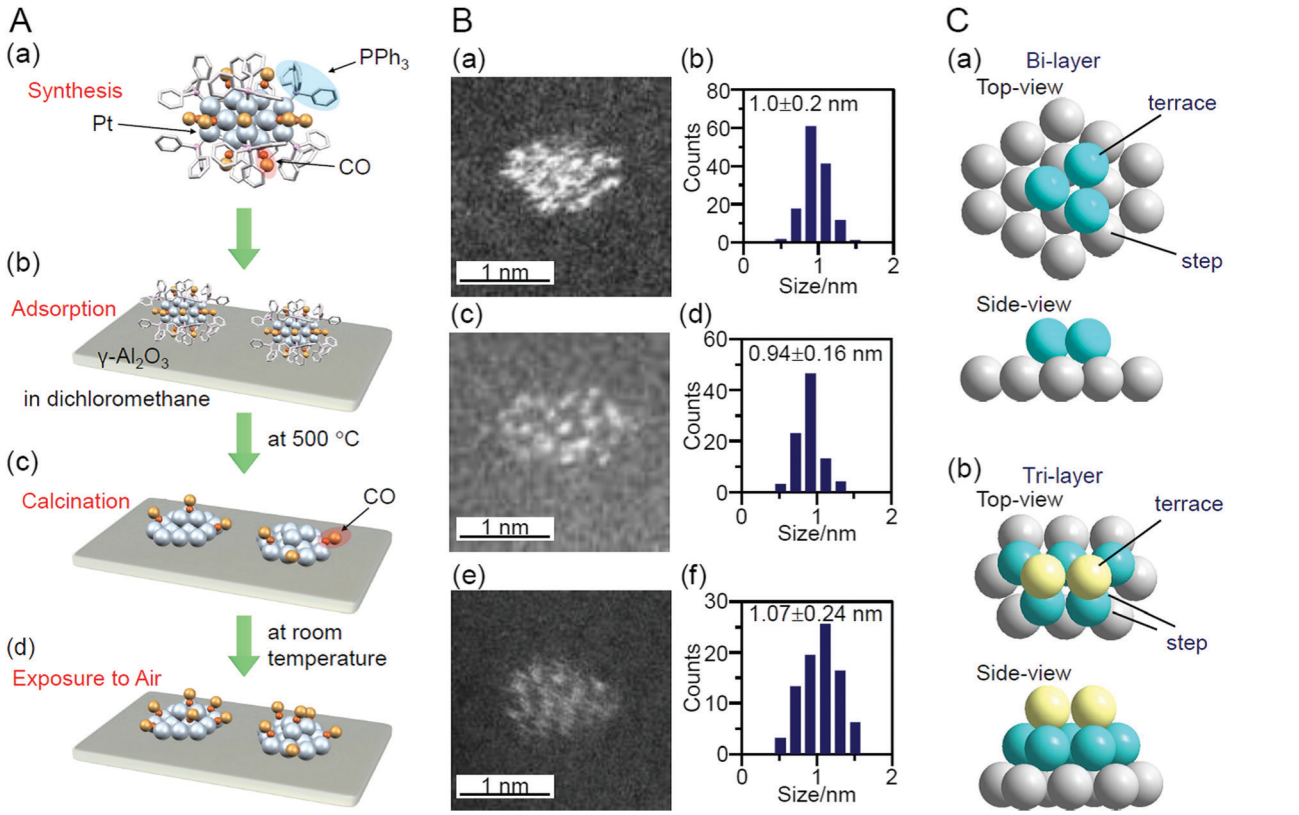


Fig. 21 (A) Schematic of preparation of Pt_{17}/γ-Al_2O_3: (a) precise synthesis of $[Pt_{17}(CO)_{12}(PPh_3)_8]Cl_n$, (b) adsorption of $[Pt_{17}(CO)_{12}(PPh_3)_8]Cl_n$ on γ-Al_2O_3 ($(Pt_{17}(CO)_{12}(PPh_3)_8/\gamma$-$Al_2O_3$), (c) calcination of ligands while maintaining the NC size (Pt_{17}/γ-Al_2O_3), and (d) exposure of Pt_{17}/γ-Al_2O_3 to air. (B) HAADF-STEM images (a, c, e) and size distribution (b, d, f) of (a, b) $[Pt_{17}(CO)_{12}(PPh_3)_8]Cl_n$, (c, d) $Pt_{17}(CO)_{12}(PPh_3)_8/\gamma$-$Al_2O_3$, and (e and f) Pt_{17}/γ-Al_2O_3. (C) Two proposed structures for Pt_{17} on γ-Al_2O_3, which were estimated based on the HAADF-STEM images of Pt_{17}/γ-Al_2O_3: (a) bi-layer and (b) tri-layer structure. In (a) and (b), both top and side views are shown. Reproduced from ref. 235. Copyright 2020 Royal Society of Chemistry.

Open Access Article. Published on 12 2021. Downloaded on 02.06.2026 12:22:59.
This article is licensed under a Creative Commons Attribution 3.0 Unported Licence.

series of operations (Fig. 21B). Compared with other noble metals (*e.g.*, Au), Pt binds strongly to O (318.4 ± 6.7 kJ mol^{-1} for Pt–O *vs.* 223 ± 21.1 kJ mol^{-1} for Au–O). Furthermore, because γ-Al_2O_3 has a complicated structure in which Al atoms are arranged octahedrally or tetrahedrally, cationic sites are present owing to the surface defects in γ-Al_2O_3.[267] Pt atoms interacted with these cation sites and, as a result, Pt clusters hardly aggregated on γ-Al_2O_3.[268] According to TGA analysis, several CO appeared to be coordinated to the surface of Pt_{17}/γ-Al_2O_3 (Fig. 21A(c)). The HAADF-STEM images suggested that the loaded Pt_{17} NCs had bi-layer or tri-layer structures (Fig. 21C). Previous studies have suggested that CO and O_2 are activated on the terrace Pt and step Pt, respectively, during the oxidation reaction of CO.[269–271] In the structure of Fig. 21C, most of the terrace Pt atoms are located near the step Pt atoms. Thus, the reaction of CO and O_2, *i.e.*, the oxidation of CO, was expected to proceed effectively over Pt_{17}/γ-Al_2O_3.

In fact, Pt_{17}/γ-Al_2O_3, loaded with 0.15 wt% Pt_{17}, showed a higher CO oxidation activity than Pt_{NP}/γ-Al_2O_3 (an industrially used Pt catalyst), in which 0.15 wt% Pt_{NP} was loaded by the impregnation method. In this experiment, Pt_{17}/γ-Al_2O_3 and Pt_{NP}/γ-Al_2O_3 were coated on a honeycomb support to evaluate their catalytic performance in a state similar to actual vehicle mounting conditions. A gas mixture consisting of 1% CO, 0.5% O_2, and 98.5% N_2 was circulated over the honeycomb support at a space velocity of 50 000 h^{-1} while the temperature of the honeycomb support was increased to 400 °C at a rate of 20 °C min^{-1}. The conversion ratio of CO over the catalyst was estimated by evaluating the components of the mixed gas before and after circulation using an exhaust gas analyzer (Fig. 22A). When Pt_{NP}/γ-Al_2O_3 was used as the catalyst, the catalytic activity started to appear at approximately 270 °C, and the conversion reached 50% at approximately 350 °C (light-off temperature) and nearly 100% at approximately 370 °C (Fig. 22B). In contrast, when Pt_{17}/γ-Al_2O_3 was used as the catalyst, the catalytic activity started from approximately 240 °C, and the conversion reached 50% at approximately 330 °C and almost 100% at approximately 350 °C (Fig. 22B). These results indicate that Pt_{17}/γ-Al_2O_3 exhibits higher catalytic activity at each temperature than Pt_{NP}/γ-Al_2O_3; namely, Pt_{17}/γ-Al_2O_3 can convert CO at lower temperatures than Pt_{NP}/γ-Al_2O_3. Similar experiments showed that Pt_{17}/γ-Al_2O_3 also has a higher catalytic activity for propylene oxidation than Pt_{NP}/γ-Al_2O_3. Currently, the catalytic activity of exhaust-gas-treating catalysts at low temperatures is expected to be improved with the spread of vehicles that frequently stop and restart their engines (*e.g.*, hybrid vehicles).[272] These results strongly suggest that Pt_{17}/γ-Al_2O_3 could be used as an exhaust-gas-treating catalyst to overcome this issue.

As mentioned above, the precursor $[Pt_{17}(CO)_{12}(PPh_3)_8]Cl_n$ can be obtained with atomic precision only by mixing the reagents under air atmosphere, heating the solvent, and using a simple separation procedure. The loaded Pt_{17} is a Pt_n cluster within the size range showing high catalytic activity.[271] Thus, it is expected that by using the method established in this study, many research groups can conduct further investigations on Pt_{17}/γ-Al_2O_3 to obtain a deeper understanding of this catalyst and will find new ways of using Pt_{17}/γ-Al_2O_3 catalysts and Pt_{17} loaded on the other oxide supports.

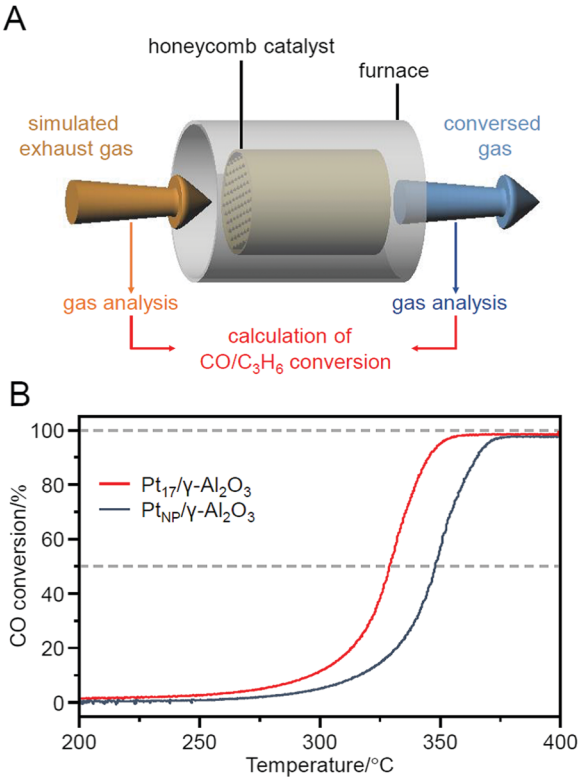
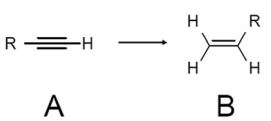


Fig. 22 (A) Schematic of the estimation of CO conversions over Pt_{17}/γ-Al_2O_3 or Pt_{NP}/γ-Al_2O_3 coated on a cordierite honeycomb substrate. (B) CO conversions over Pt_{17}/γ-Al_2O_3 or Pt_{NP}/γ-Al_2O_3. Reproduced from ref. 235. Copyright 2020 Royal Society of Chemistry.

2.2. Reduction reaction

2.2.1. Carbon–carbon multiple-bond reduction. Alkenes (olefins) are lightweight and inexpensive and have excellent chemical/physical properties and workability. They are also excellent in terms of safety and recyclability. Because of these properties, alkenes have a wide range of uses, such as in making shopping bags, shampoo bottles, food packaging materials, home electronic appliances/automobile parts, sports/leisure goods, and agricultural/civil engineering materials. Such alkenes are generally synthesized by semihydrogenation of alkynes (Scheme 6A).

In 2014, Jin *et al.* used $Au_{25}(PET)_{18}$/oxide (TiO_2, CeO_2, SiO_2, or Al_2O_3) for the semihydrogenation reaction of various terminal alkyne compounds (the products are the terminal alkenes; Scheme 6).[236,273] In this study, the ligands were not removed



Scheme 6 Semihydrogenation of terminal alkyne using metal NC catalysts. Generally, the reaction is conducted in the presence of a base, such as pyridine, because amine additives can largely promote the semihydrogenation reaction,[273] and pyridine gave the best catalytic result among them.[236] The reaction was conducted under H_2 atmosphere in ethanol or/and H_2O. A = terminal alkyne, B = alkene.

This journal is © The Royal Society of Chemistry 2021

Open Access Article. Published on 12 2021. Downloaded on 02.06.2026 12:22:59.
This article is licensed under a Creative Commons Attribution 3.0 Unported Licence.

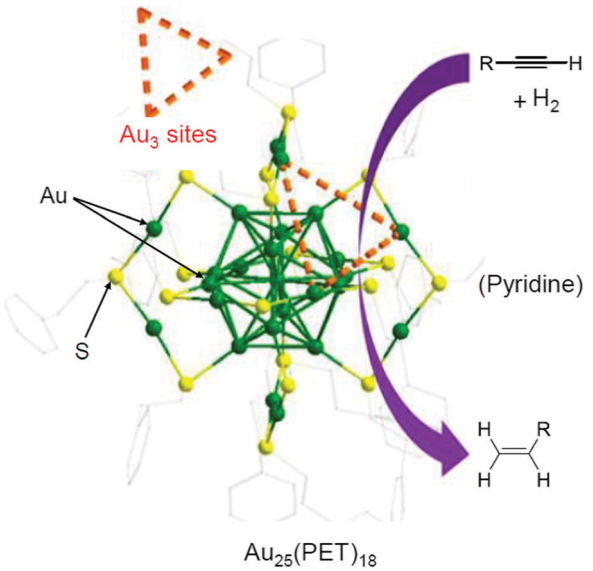
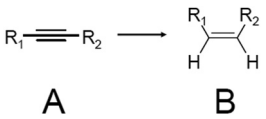


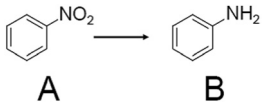
Fig. 23 Schematic illustration of semihydrogenation of $Au_{25}(PET)_{18}/TiO_2$. Reproduced with permission from ref. 236. Copyright 2014 American Chemical Society.



Scheme 7 Semihydrogenation of internal alkyne using metal NC catalysts. Generally, the reaction is conducted in the presence of a base, such as pyridine, because amine additives can largely promote the semihydrogenation reaction,[273] and pyridine gave the best catalytic result among them.[236] The reaction was conducted under H_2 atmosphere in ethanol or/and H_2O. A = internal alkyne, B = alkene.

because the catalyst was calcined at 150 °C. $Au_{25}(PET)_{18}/TiO_2$ obtained under such conditions showed, for example, a conversion efficiency and selectivity of almost 100% for the semihydrogenation reaction of 4-phenyl-1-butyne. For the mechanism, it was speculated that the reaction started by adsorption of the terminal alkyne to the plane triangular Au_3 site in $Au_{25}(PET)_{18}$ (Fig. 23). $Au_{25}(PET)_{18}/TiO_2$ showed little activity against semihydrogenation of internal alkynes (Scheme 7),[236,273] which do not contain the terminal alkyne. In contrast, a sample prepared by the calcination of $Au_{25}(PET)_{18}/TiO_2$ at 300 °C for 1 h under vacuum showed a conversion efficiency in the range of 52.6–59.7% and selectivity of more than 97% for such semihydrogenation of internal alkynes. This finding indicates that ligand removal is essential for the progress of semihydrogenation of internal alkynes.

In 2017, Wang *et al.* succeeded in the precise synthesis of $[Au_{38}(PhC{\equiv}C)_{20}(PPh_3)_4]^{2+}$ (PhC≡C = phenylacetylene; Fig. 2J) and $[Au_{38}(m\text{-MBT})_{20}(PPh_3)_4]^{2+}$ (*m*-MBT = 3-methylbenzenethiolate; Fig. 2K). These two Au NCs have the same number of Au atoms and ligands. The authors conducted a catalytic study using these two NCs.[178] $Au_{38}(PhC{\equiv}C)_{20}(PPh_3)_4/TiO_2$ showed a conversion efficiency of more than 97% for

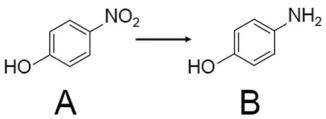


Scheme 8 Hydrogenation of nitrobenzene using metal NC catalysts. The reaction was conducted under a flow of H_2 in toluene. A = nitrobenzene, B = aniline.

semihydrogenation of both the terminal alkyne and internal alkyne. This result differs from the above result for $Au_{25}(PET)_{18}/TiO_2$: for $Au_{25}(PET)_{18}/TiO_2$, semihydrogenation of the internal alkyne proceeded only after ligand removal. This difference was interpreted to be caused by the differences in the mechanisms of the semi-hydrogenation reactions for the two systems. For $Au_{38}(m\text{-MBT})_{20}(PPh_3)_4/TiO_2$, only a very low conversion efficiency was observed. The authors also investigated the effect of calcination of $Au_{38}(PhC{\equiv}C)_{20}(PPh_3)_4/TiO_2$ on the semihydrogenation reaction of diphenylacetylene. For calcination at 130–340 °C, the selectivity of trans-stilbene improved with increasing temperature. It was interpreted that the elimination of part of the ligands formed a larger space on the surface of the metal NCs, which worked effectively for the formation of these bulky trans-stilbene.

2.2.2. Nitro-group reduction. The reduction of 4-nitrophenol to 4-aminophenol (Scheme 8) proceeds at room temperature in an aqueous solution using molten metal or loaded metal NPs as catalysts. This reaction is often used as a model reaction because the progress of the reaction can be easily traced using the decrease in absorption intensity at 400 nm *via* UV-visible absorption spectroscopy. In 2013, Scott *et al.* conducted a study on the catalytic activity of $Au_{25}(PET)_{18}$/carbon black (CB) for this reduction reaction.[237] Extended X-ray absorption fine structure (EXAFS) analysis showed that the ligands in this catalyst began to be removed at 125 °C and were completely removed at 250 °C. In contrast, when traced by TGA, the mass loss of the first stage was observed in the temperature range of 150–300 °C (the mass loss of the second stage above 300 °C was due to the oxidation of the support). These results are in good agreement with the later interpretation by other groups that the desorbed ligands are adsorbed on the support.[215–217,233] The average particle size of the loaded Au NCs increased with increasing calcination temperature. For catalytic activity, the sample calcined at 250 °C showed the highest conversion efficiency, indicating that it is very important to expose the surface of metal NCs while preventing aggregation as much as possible to achieve high catalytic activity.

In 2015, Yan *et al.* studied the catalysis for hydrogenation of nitrobenzene to aniline (Scheme 9).[223] Aniline is treated as an



Scheme 9 Reduction of 4-nitrophenol using metal NC catalysts. Generally, the reaction proceeds in the presence of $NaBH_4$. The reaction was conducted in a mixture of H_2O and tetrahydrofuran. A = 4-nitrophenol, B = 4-aminophenol.

Open Access Article. Published on 12 2021. Downloaded on 02.06.2026 12:22:59.
This article is licensed under a Creative Commons Attribution 3.0 Unported Licence.

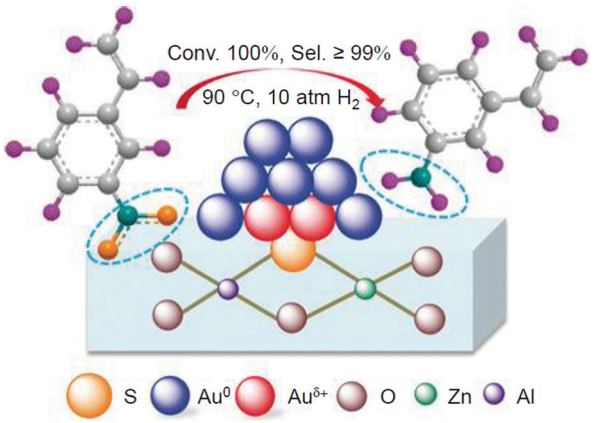
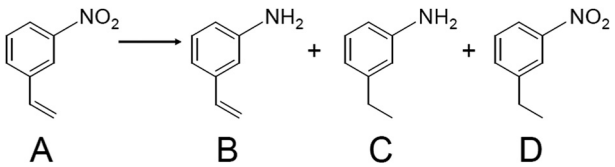


Fig. 24 Schematic of hydrogenation of 3-nitrostyrene using Au_{25}/ZnAl-HT. Reproduced with permission from ref. 238. Copyright 2017 Wiley-VCH.



Scheme 10 Hydrogenation of 3-nitrostyrene using metal catalysts. The reaction was conducted under H_2 atmosphere in toluene. A = 3-nitrostyrene, B = 3-vinylaniline, C = 3-ethylaniline, D = 3-ethylnitrobenzene.

intermediate in the manufacture of medical drugs, polymers, herbicides, and other substances. Aniline is often synthesized from the corresponding aromatic nitro compound by catalytic hydrogenation using a commercially available catalyst. Pt, Pd, and iridium (Ir) are mainly used as catalysts. However, in these catalytic reactions, not only the nitro group but also the carbonyl and other double bonds are reduced. Therefore, the development of a catalyst that selectively reduces nitro groups is required. In the study by Yan *et al.* described in Section 2.1.3, Au_{25}/HAP (more exactly, Au_{25} aggregates to a particle size of 2.4 nm on HAP in this study) showed a conversion efficiency and selectivity of more than 99% for the hydrogenation reaction from nitrobenzene to aniline. Almost no activity was observed for $Au_{25}(MHA)_{18}$/HAP without calcination. From this result, it was concluded that ligand removal is necessary for this reaction as well.

In 2017, Zhang and Liu *et al.* prepared the catalyst Au_{25}/ZnAl-HT (ZnAl-HT = hydrotalcite) using $Au_{25}(Cys)_{18}$ (Cys = cysteine) and ZnAl-HT. They found that it selectively reduces the nitro group of 3-nitrostyrene (Fig. 24 and Scheme 10).[238] This catalyst was prepared by calcination at a temperature above 300 °C. Based on TEM images, it was interpreted that calcination caused a slight increase in particle size from 1.4 to 1.7 nm. The obtained Au_{25}/ZnAl-HT showed a conversion efficiency of 100% and 3-vinylaniline selectivity of 99% at a reaction temperature of 90 °C (Fig. 24). 3-Nitrostyrene has two functional groups, the nitro group and the alkene (C=C). It was interpreted that Au_{25}/ZnAl-HT selectively reduced the nitro group because the former was easier to approach to ZnAl-HT

Scheme 11 Reaction of dehydrogenation of ammonia diborane using metal NC catalysts. The reaction was conducted in H_2O under air atmosphere.

than the latter. Because this catalyst showed no catalytic activity when uncalcined, it was interpreted that this catalytic reaction could only proceed by removing the ligand of Au_{25} NCs.

2.3. H_2 generation

Ammonia borane is attracting attention as a lightweight, highly stable, and highly efficient hydrogen storage agent. In 2015, Tsukuda *et al.* reported that Ag_{44}/MPC (MPC = mesoporous carbon) functions as a catalyst for dehydrogenation of ammonia borane (NH_3BH_3; Scheme 11).[239] In catalyst preparation, first, $[Ag_{44}(SPhF)_{30}](PPh_4)_4$ (SPhF = 4-(fluorophenyl)thiolate; Fig. 2L) was adsorbed on MPC, and then the obtained sample was calcined at 150 °C for 30 min and then at 300 °C for 2 h under vacuum. It was revealed that the Ag–S bond dissociated and the ligand was desorbed as SPhF or $(SPhF)_2$ by such calcination (Fig. 25A). This ligand desorption mechanism was largely

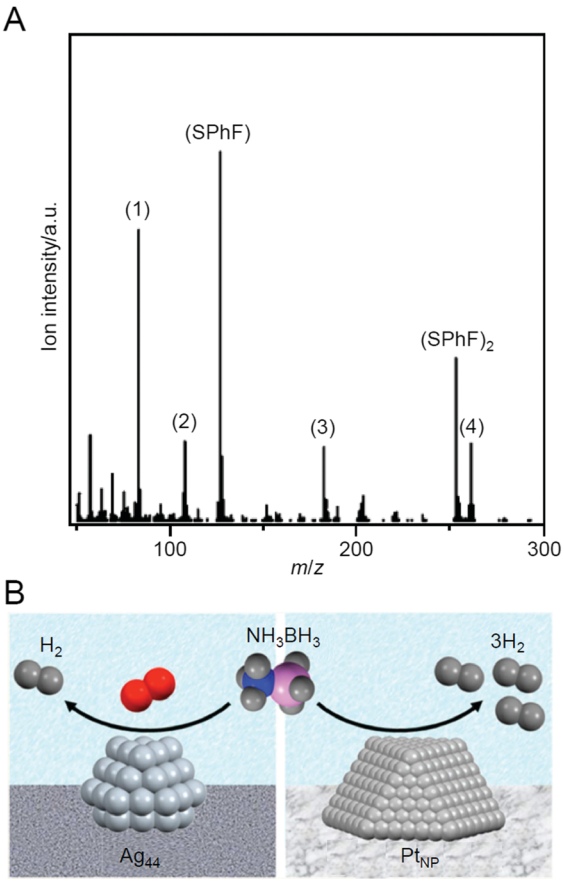


Fig. 25 (A) Typical mass spectrum of the desorbed species from $[Ag_{44}(SPhF)_{30}](PPh_4)_4$ at 297 °C. The mass peaks of (1) PhF, (2) PPh, (3) PPh_2, and (4) PPh_3 are fragments of PPh_4 and SPhF, produced by electron-impact ionization. (B) Comparison of H_2 generation from NH_3BH_3 in the presence of Ag_{44} NCs/MPC and Pt_{NP}/MPC. Reproduced with permission from ref. 239. Copyright 2015 American Chemical Society.

This journal is © The Royal Society of Chemistry 2021

Open Access Article. Published on 12 2021. Downloaded on 02.06.2026 12:22:59.
This article is licensed under a Creative Commons Attribution 3.0 Unported Licence.

different from that observed for SC12-protected Ag NCs ($Ag_n(SC12)_m$ NCs), in which S–C dissociation also proceeds at the same time. The S–C bond in $[Ag_{44}(SPhF)_{30}](PPh_4)_4$ is stronger than that in $Ag_n(SC12)_m$ NCs. This difference was interpreted to be related to the selective dissociation of the Ag–S bond and the complete desorption of S from the Ag_{44} surface. The obtained Ag_{44}/MPC showed high catalytic activity for the dehydrogenation reaction from ammonia borane under oxygen or air atmosphere. Some comparison experiments revealed that the dehydrogenation reaction using Ag_{44}/MPC as a catalyst proceeded *via* a mechanism different from that proceeding when NPs composed of other metals such as Pt and Pd were used as catalysts (Fig. 25B).

2.4. Photocatalytic water splitting

With global warming and the depletion of fossil resources, our fossil-fuel-dependent society is expected to shift to one that instead uses H_2 as a clean and renewable energy source. Water-splitting photocatalysts (Fig. 26A) can produce H_2 from water using sunlight, both of which are almost infinite on the earth.[274] Therefore, the photocatalytic water-splitting reaction is considered one of the cleanest energy-production reactions for humankind. However, further improvement of the activity is necessary to enable their practical application.

In many cases, water-splitting photocatalysts need to load metal NPs/NCs (cocatalysts) as active sites (Fig. 26A),[275] and their particle-size control is an extremely effective means for improving the water-splitting activity.[276,277] Several previous studies have shown that the use of atomically precise metal NCs as precursors could load metal NCs with controlled particle size on photocatalysts, which could lead to improvement of the water-splitting activity.[200,239–245,278–280]

In 2013, Negishi and Kudo *et al.* succeeded in loading Au_{25} on $BaLa_4Ti_4O_{15}$, which is one of the highly active photocatalysts. In the experiment, $Au_{25}(SG)_{18}$ was first adsorbed on $BaLa_4Ti_4O_{15}$ with high efficiency (>99%) by stirring them in water.[240] Glutathione has two carboxyl groups and one amino group. It can be considered that $Au_{25}(SG)_{18}$ was efficiently adsorbed on the photocatalyst because the polar functional groups of $Au_{25}(SG)_{18}$ formed hydrogen bonds with the –OH groups on the surface of $BaLa_4Ti_4O_{15}$. Then, the obtained $Au_{25}(SG)_{18}$/$BaLa_4Ti_4O_{15}$ was calcined at 300 °C for 2 h to remove the ligands from $Au_{25}(SG)_{18}$. TEM images and XPS spectra revealed that such calcination resulted in (1) removal of ligands from Au NCs and (2) little aggregation of the loaded Au NCs. The obtained $Au_{25}(SG)_{18}$/$BaLa_4Ti_4O_{15}$ exhibited higher water-splitting activity than Au_{NP}/$BaLa_4Ti_4O_{15}$ in which a large Au_{NP} was loaded by the impregnation method. In 2015, the same group clarified that (1) this loading method is also effective for loading other sizes of Au_n NCs; (2) however, to load Au_n NCs on $BaLa_4Ti_4O_{15}$ while preventing the increase in particle size, it is necessary to use stable $Au_n(SG)_m$ NCs as a precursor (Fig. 26B), and (3) it is essential to remove the ligands by calcination to obtain higher activity (Fig. 26C).[241] Furthermore, in 2018, the same group clarified that the precise loading of Au_{25} is also possible in the same way when $SrTiO_3$ is used as a photocatalyst.[242]

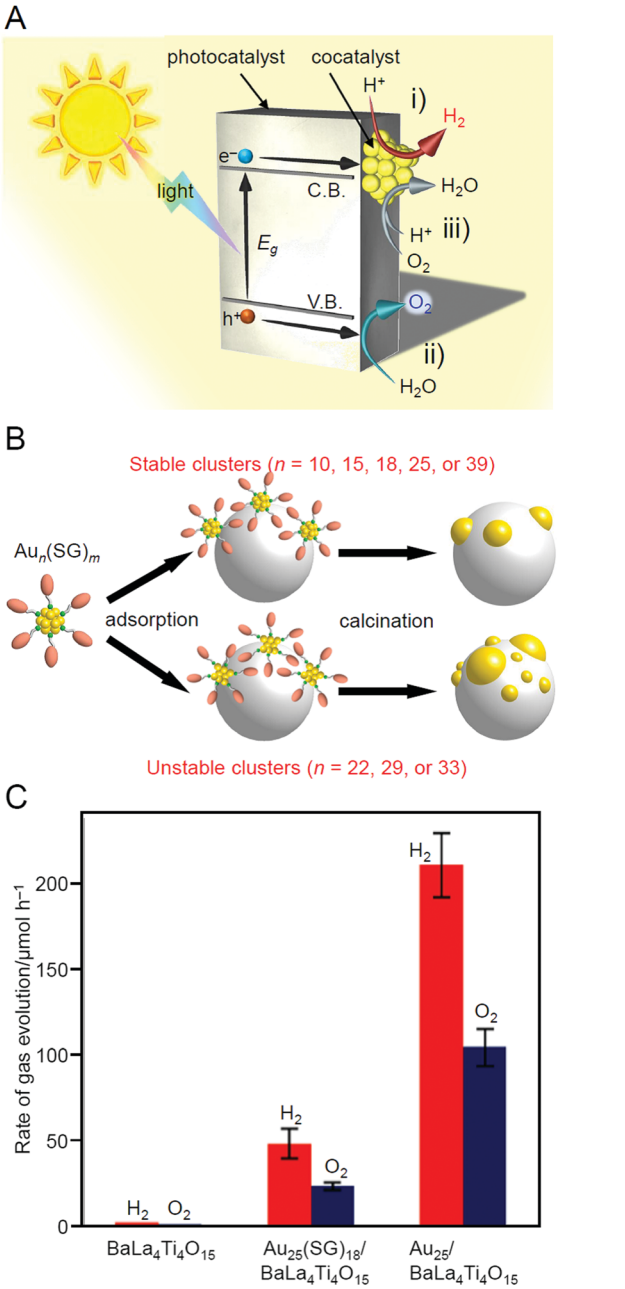


Fig. 26 (A) Schematic of photocatalytic water splitting using a one-step photoexcitation system (C.B., conduction band; V.B., valence band; E_g, band gap) showing the processes of (i) hydrogen evolution, (ii) oxygen evolution, and (iii) oxygen photoreduction. (B) Schematic of the aggregation of $Au_n(SG)_m$ on the photocatalyst depending on the cluster size (0.1 wt% Au). (C) Comparison of the photocatalytic activities of $BaLa_4Ti_4O_{15}$, $Au_{25}(SG)_{18}$/$BaLa_4Ti_4O_{15}$, and Au_{25}/$BaLa_4Ti_4O_{15}$. Reproduced with permission from ref. 241 and ref. 244. Copyright 2015 American Chemical Society and 2019 American Chemical Society.

Because such an overall water splitting is an uphill reaction (Fig. 27A),[281] the reverse reaction proceeds easily.[243] Therefore, to create a highly active photocatalyst in such a reaction system, it is necessary to efficiently suppress the reverse reaction. In addition, light irradiation of the photocatalyst promotes aggregation of the cocatalyst.[240] Therefore, to create a highly stable and active

Open Access Article. Published on 12 2021. Downloaded on 02.06.2026 12:22:59.
This article is licensed under a Creative Commons Attribution 3.0 Unported Licence.

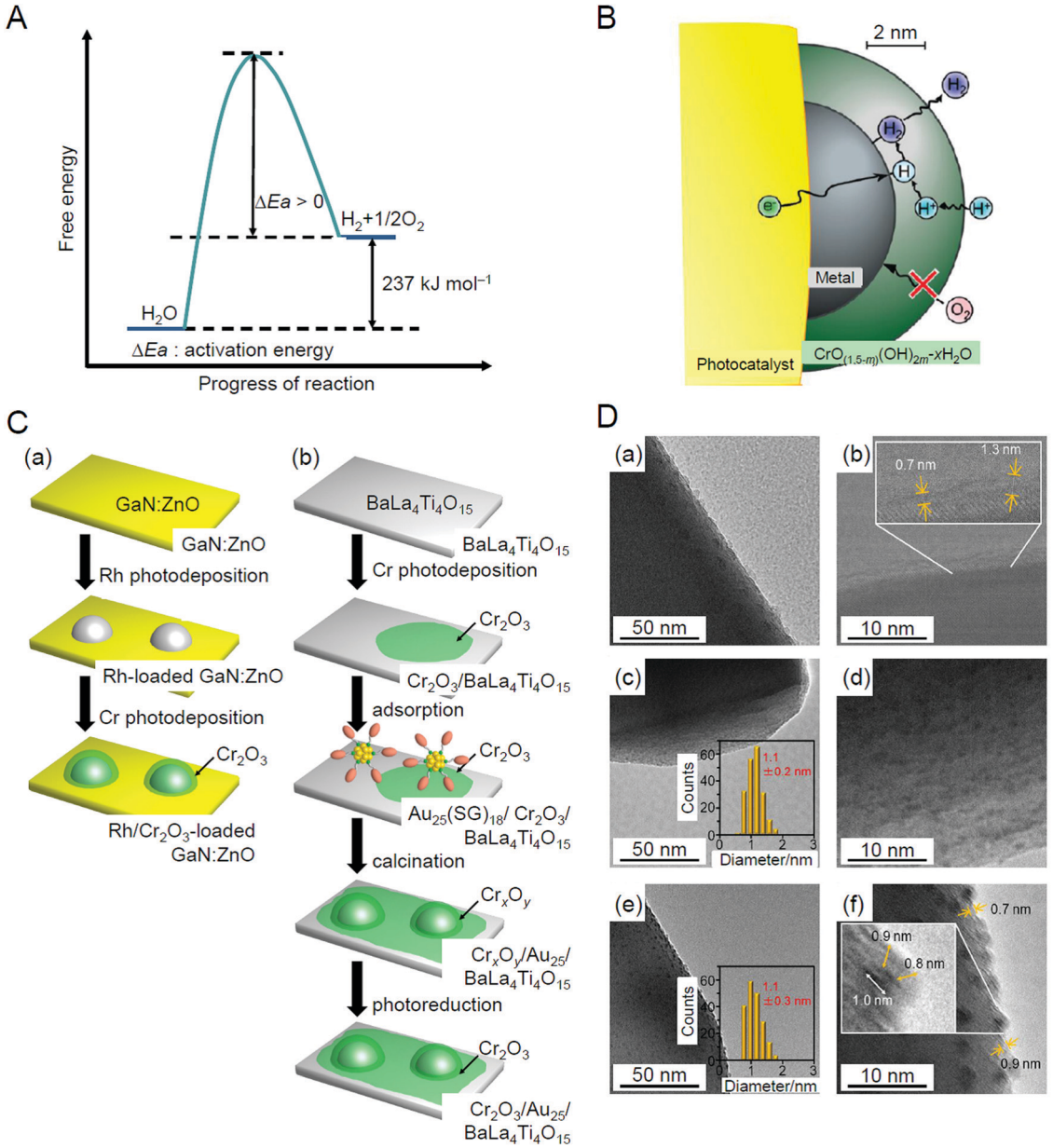


Fig. 27 (A) Activation energy of water-splitting reaction.[281] (B) Schematic model of H_2 evolution reaction on core/shell noble-metal/Cr_2O_3 particulate system as a cocatalyst for photocatalytic overall water splitting.[287] (C) Comparison of the procedures of Cr_2O_3 shell formation in (a) the literature[286] and (b) our work.[243] (D) TEM images (a, c and e) and HR-TEM images (b, d and f) of (a and b) $Cr_2O_3/BaLa_4Ti_4O_{15}$ (0.5 wt% Cr), (c and d) $Au_{25}(SG)_{18}/Cr_2O_3/BaLa_4Ti_4O_{15}$ (0.1 wt% Au; 0.5 wt% Cr), and (e and f) $Cr_2O_y/Au_{25}/BaLa_4Ti_4O_{15}$ (0.1 wt% Au; 0.5 wt% Cr). Cr_2O_y indicates the chromium oxide in which part of the chromium was oxidized to a highly oxidized state (>3+). In (c and e), the insets show the core-size distributions of the particles. In (b and f), the thicknesses of the Cr_2O_3 or Cr_2O_y shells are indicated by yellow double-pointed arrows. In (f), the particle size is also indicated by a white double-pointed arrow. Reproduced with permission from ref. 243 and ref. 287. Copyright 2018 American Chemical Society and 2009 American Chemical Society.

photocatalyst, it is necessary to take some measures to suppress the aggregation of the cocatalyst. One effective means to suppress the reverse reaction of water splitting is to form a chromium oxide (Cr_2O_3) shell on the surface of the loaded cocatalyst. This Cr_2O_3 shell is permeable to H^+ but not to O_2 approaching from the outside (Fig. 27B). Domen *et al.* reported that when the cocatalyst surface is covered by the Cr_2O_3 shell, it is possible to suppress only the progress of the reverse reaction while maintaining the H_2 evolution activity.[186,188–190,282–288] In their studies, they first loaded the cocatalysts and then formed the Cr_2O_3 shell on the cocatalysts using the photodeposition method (Fig. 27C(a)). However, when $Au_{25}/BaLa_4Ti_4O_{15}$ was irradiated with light, the loaded metal NCs aggregated.[240] Thus, when the method reported by Domen *et al.* is used as is, it is difficult to form the Cr_2O_3 shell on the surface of the loaded metal NCs while maintaining the number of atoms of the metal NCs. Meanwhile, studies in the field of surface science have revealed that when a metal oxide support loaded with metal NCs is heated under H_2 or O_2 atmosphere, a strong metal–support interaction (SMSI) is induced, thereby leading to the formation of an oxide film on the

 This journal is © The Royal Society of Chemistry 2021

Open Access Article. Published on 12 2021. Downloaded on 02.06.2026 12:22:59.
This article is licensed under a Creative Commons Attribution 3.0 Unported Licence.

metal NCs.[289–296] Therefore, Kurashige *et al.* attempted to form a Cr_2O_3 shell on the surface of the cocatalyst using such a SMSI effect (Fig. 27C(b)).[243] As a result, they created a highly functional water-splitting photocatalyst that addresses both the reverse reaction and the aggregation of Au_{25}.

In the Cr_2O_3-shell-formation process used in their study, the Cr_2O_3 layer was first formed on $BaLa_4Ti_4O_{15}$ using the photodeposition method before loading Au_{25} (Fig. 27D(a) and (b)). Then, $Au_{25}(SG)_{18}$ was adsorbed on the surface of the obtained $Cr_2O_3/BaLa_4Ti_4O_{15}$ (Fig. 27D(c) and (d)). The photocatalyst after the adsorption of $Au_{25}(SG)_{18}$ ($Au_{25}(SG)_{18}/Cr_2O_3/BaLa_4Ti_4O_{15}$) was calcined at 300 °C for 2 h under a reduced pressure. The Au_{25} was covered with a Cr_2O_3 shell during calcination *via* the SMSI effect (Fig. 27D(e) and (f)). Part of the chromium was oxidized to a highly oxidized state (>3+) by calcination; however, it was reduced to Cr_2O_3 by irradiation with UV light. The obtained $Cr_2O_3/Au_{25}/BaLa_4Ti_4O_{15}$ showed nearly 20 times higher water-splitting activity than $Au_{25}/BaLa_4Ti_4O_{15}$. Furthermore, even when the light irradiation was continued for 10 h, almost no aggregation of Au_{25} occurred.[243] In 2019, Kurashige *et al.* reported that substituting one Au atom of $Cr_2O_3/Au_{25}/BaLa_4Ti_4O_{15}$ with a Pt atom could induce even higher water-splitting activity.[244] In 2020, they succeeded in obtaining the highest quantum yield (16% at 270 nm) for $BaLa_4Ti_4O_{15}$ catalysts by using Rh instead of Au as the base element of the cocatalysts (Fig. 28).[245] For $Rh_{2-x}Cr_xO_3/BaLa_4Ti_4O_{15}$, the cocatalyst is not currently controlled with atomic precision. However, if a precise synthesis method is established for Rh_n NCs in the future, it may become possible to control cocatalysts with atomic precision for $Rh_{2-x}Cr_xO_3/BaLa_4Ti_4O_{15}$. It is expected that the establishment of such precise synthesis methods will enable us to create even more highly active $Rh_{2-x}Cr_xO_3/BaLa_4Ti_4O_{15}$.

The above studies used photocatalysts that can achieve the overall water-splitting reaction using UV light. However, to enable the practical application of water-splitting photocatalysts in the future, it is necessary to use visible light, which accounts for ~40% of solar energy, for the water-splitting reaction.[297] To completely decompose water, the positions of its conduction band (C. B.) and valence band (V. B.) must have sufficient energy for the H_2 evolution reaction (HER) and O_2 evolution reaction (OER) to proceed, respectively (Fig. 26A). Furthermore, to suppress the recombination of excited electrons and holes, the photocatalyst needs to have both high crystallinity and high specific surface area. Because of these requirements, there are currently only a few semiconductor photocatalysts that can completely split water in one step using visible light.[298] Nevertheless, overall water splitting can also be achieved by combining a semiconductor causing its half-reaction (HER and OER) and a redox couple responsible for the transfer of charges (electrons and holes) between them.[299] Such a system, which imitates the photosynthesis occurring in plants, is called the Z-scheme system (Fig. 29A).

In 2017, Yang *et al.* succeeded in highly activating the graphitic carbon nitride (g-C_3N_4), which functions as a HER photocatalyst in the Z-scheme system, by using atomically precise $Ag_{25}(2,4\text{-}SPhMe_2)_{18}PPh_4$ (Fig. 2G) and $[Ag_{24}Pt(2,4\text{-}SPhMe_2)_{18}](PPh_4)_2$

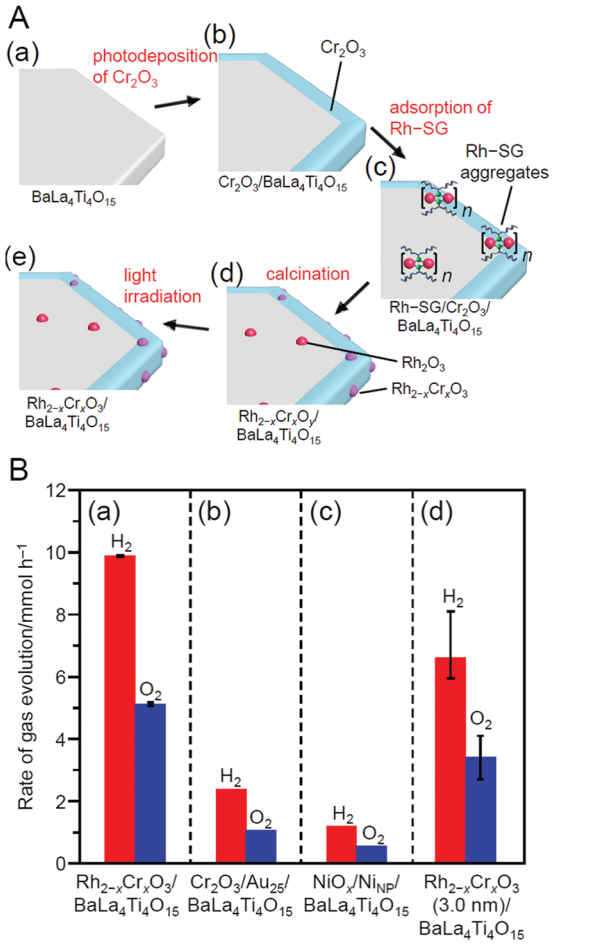


Fig. 28 (A) Schematic of the experimental procedure for the formation of $Rh_{2-x}Cr_xO_3/BaLa_4Ti_4O_{15}$. (a) $BaLa_4Ti_4O_{15}$, (b) $Cr_2O_3/BaLa_4Ti_4O_{15}$, (c) Rh–SG/$Cr_2O_3/BaLa_4Ti_4O_{15}$, (d) $Rh_{2-x}Cr_xO_y/BaLa_4Ti_4O_{15}$, and (e) $Rh_{2-x}Cr_xO_3/BaLa_4Ti_4O_{15}$. $Rh_{2-x}Cr_xO_y$ indicates $Rh_{2-x}Cr_xO_3$ including highly oxidized Cr (>3+). (B) Comparison of rates of H_2 and O_2 evolution by photocatalytic water-splitting over different photocatalysts (a) $Rh_{2-x}Cr_xO_3/BaLa_4Ti_4O_{15}$ (0.09 wt% Rh and 0.10 wt% Cr), (b) $Cr_2O_3/Au_{25}/BaLa_4Ti_4O_{15}$ (0.10 wt% Au and 0.50 wt% Cr), (c) $NiO_x/Ni_{NP}/BaLa_4Ti_4O_{15}$ (0.50 wt% Ni), and (d) $Rh_{2-x}Cr_xO_3$ (3.0 nm)/$BaLa_4Ti_4O_{15}$ (0.10 wt% Rh and 0.15 wt% Cr). In this study, $NiO_x/Ni_{NP}/BaLa_4Ti_4O_{15}$ and $Rh_{2-x}Cr_xO_3$ (3.0 nm)/$BaLa_4Ti_4O_{15}$ loaded with $Rh_{2-x}Cr_xO_3$ NPs of ~3.0 nm were prepared by the impregnation method. Reproduced with permission from ref. 245. Copyright 2020 Wiley-VCH.

(Fig. 2M) as precursors of cocatalysts.[200] In the experiment, each NC was first adsorbed on g-C_3N_4 by stirring them in mixed solvent of toluene and dichloromethane for 12 h. Then, the ligand was removed from Ag_{25} or $Ag_{24}Pt$ by calcination at 150 °C under argon (Ar) atmosphere for 2 h. These photocatalysts were dispersed in an aqueous solution containing triethanolamine (TEOA; sacrificial agent), and the HER was proceeded by irradiating the aqueous solution with visible light (>420 nm). As a result, Ag_{25}/g-C_3N_4 and $Ag_{24}Pt$/g-C_3N_4 generated 76 and 330 times more H_2 than g-C_3N_4 without the cocatalyst, respectively (Fig. 29B). The authors reported that $Ag_{24}Pt$/g-C_3N_4 showed higher activity than Ag_{25}/g-C_3N_4 because Pt substitution facilitated the transfer of photoexcited electrons from g-C_3N_4 to the cocatalyst

Open Access Article. Published on 12 2021. Downloaded on 02.06.2026 12:22:59.
This article is licensed under a Creative Commons Attribution 3.0 Unported Licence.

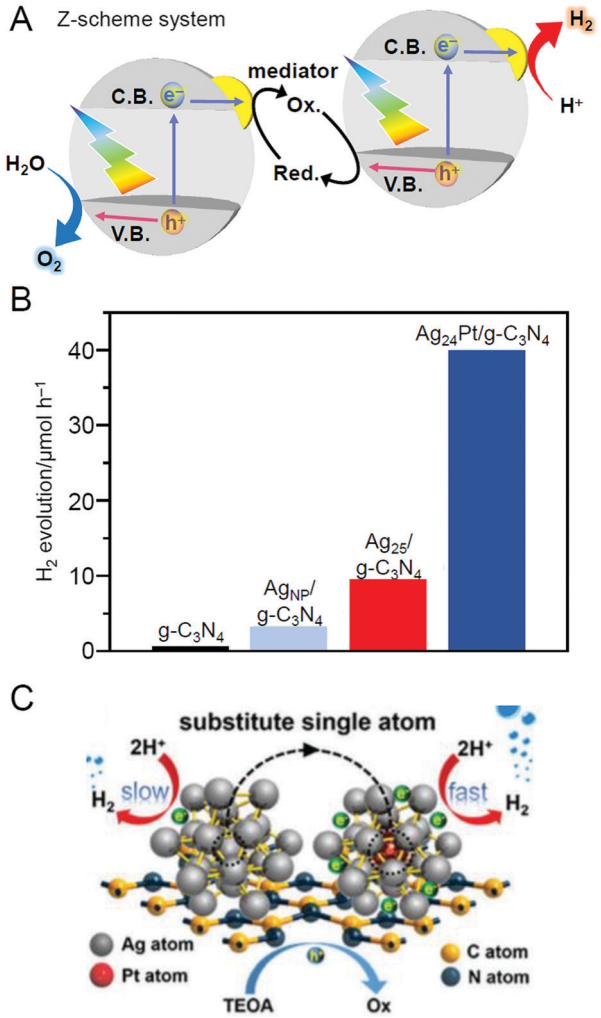


Fig. 29 (A) Schematics of Z-scheme system for overall water splitting. (B) Comparison of the photocatalytic H_2-evolution activities of g-C_3N_4, Ag_{NP}/g-C_3N_4, Ag_{25}/g-C_3N_4, and $Ag_{24}Pt$/g-C_3N_4. (C) Proposed photocatalytic H_2-evolution mechanism. Reproduced with permission from ref. 200 and ref. 297. Copyright 2017 Royal Society of Chemistry and 2020 Royal Society of Chemistry.

(Fig. 29C). Thus, it was shown that cocatalyst control using atomically precise metal NCs is also effective for high activation of the g-C_3N_4 HER photocatalyst.

2.5. Electrocatalytic reaction

In the photocatalytic water-splitting reaction described in Section 2.4, H_2 and O_2 are directly generated from water by sunlight. These reactions convert light into chemical energy and are therefore also called artificial photosynthesis. In contrast, the use of a solar cell[300] enables us to obtain electrical energy from sunlight. When water is electrolyzed using the obtained electrical energy,[301–304] it is possible to obtain chemical energy from sunlight and water, similar to the case of a photocatalytic reaction.[305,306]

The electrolysis of water consists of two half-reactions, the HER and OER. When a voltage is applied on the metal electrode, a reduction reaction proceeds at the cathode and an oxidation reaction proceeds at the anode, and water molecules are electrolyzed into H_2 and O_2. However, in reality, the reaction does not proceed even if a higher potential than the redox potential (HER: 0 V *vs.* SHE, OER: 1.23 V *vs.* SHE) in each reaction is applied onto the metal electrode. This is because the activation energy in each reaction is high. Therefore, precious-metal particles are loaded on the electrode as catalysts.[307] Previous studies have revealed that atomically precise metal NCs are also extremely promising as such electrode catalysts.[180,246,247]

In 2017, Chen *et al.* conducted a study using $Pd_6(SC12)_{12}$ as a precursor of an electrode catalyst (Fig. 30A).[246] In their experiment, $Pd_6(SC12)_{12}$ was first adsorbed on AC, and then the catalysts were calcined at 200 °C under reduced pressure. During adsorption and calcination (Fig. 30B), almost no aggregation of metal NCs occurred. In the HER measurement, 0.5 M sulfuric acid (H_2SO_4) was used as the electrolyte. The Pd_6/AC showed high HER activity and durability (Fig. 30C). For example, Pd_6/AC has 2.86 and 10.22 times higher current densities than $Pd_6(SC12)_{12}$/AC and commercially available Pt/carbon (C) catalysts, respectively, when comparing the HER activity at an applied voltage of −0.423 V. The removal of the ligand formed a wider space around Pd and reduced the charge density of Pd. It was interpreted that because the removal of the ligand made it easier for the reaction substrate (H^+) to approach Pd, it improved the HER activity. In contrast, $Pd_6(SC12)_{12}$/AC showed higher activity than Pd_6/AC and Pt/C for the OER. These results indicate that the presence or absence of ligand removal should be determined while taking the reaction mechanism into consideration.

In 2018, Zhu *et al.* used $Au_2Pd_6S_4(PPh_3)_4(SPhF_2)_6$ ($SPhF_2$ = 3,4-difluorobenzenethiolate; Fig. 2N), which was newly

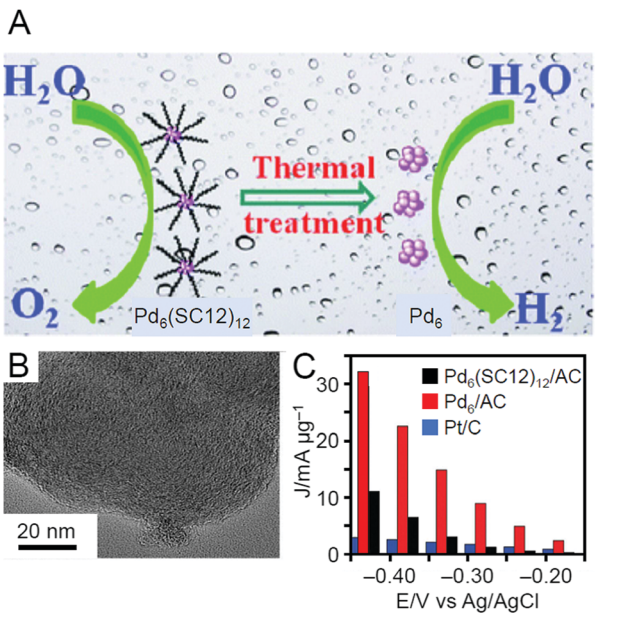


Fig. 30 (A) Schematic of difference in electrochemical reaction before and after thermal treatment of $Pd_6(SC12)_{12}$/AC (B) HR-TEM images of Pd_6/AC. (C) Comparison of the current densities of the HER on the samples at different potentials. Reproduced with permission from ref. 246. Copyright 2017 Royal Society of Chemistry.

This journal is © The Royal Society of Chemistry 2021

Open Access Article. Published on 12 2021. Downloaded on 02.06.2026 12:22:59.
This article is licensed under a Creative Commons Attribution 3.0 Unported Licence.

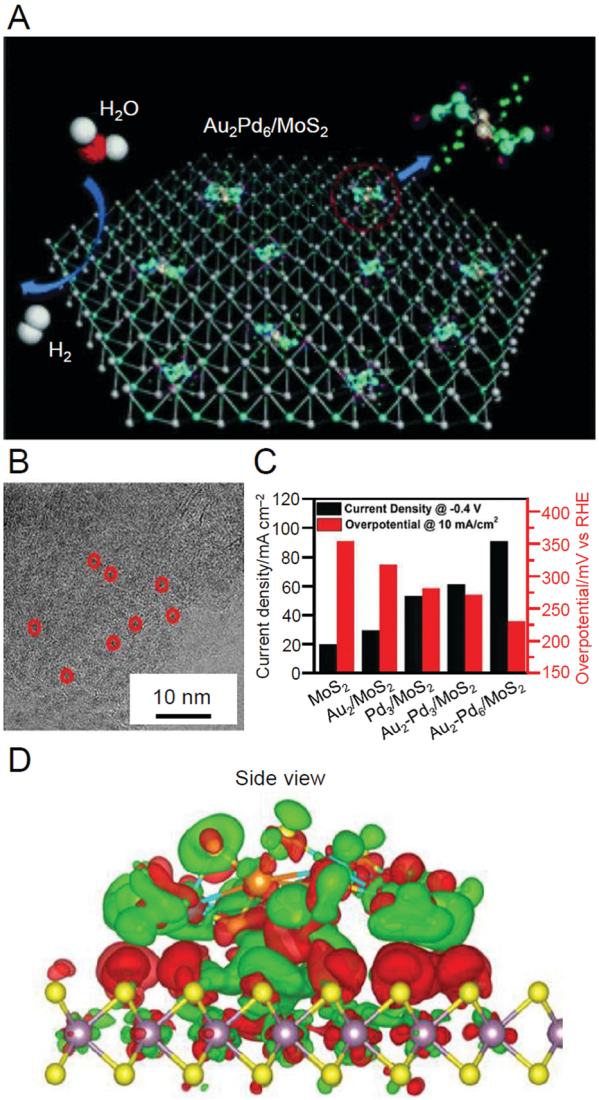


Fig. 31 (A) Schematic of HER on Au_2Pd_6/MoS_2 system. (B) HR-TEM image of Au_2Pd_6/MoS_2 system (Au_2Pd_6 NCs marked by red circles). (C) Comparison of the overpotential at a current density of 10 mA cm^{-2} (red column on the right) and the current density at −0.4 V *vs.* RHE (black column on the left). (D) Charge deformation density of Au_2Pd_6/MoS_2 system. The charge density of Au_2Pd_6 NC decreased while the charge density of MoS_2 increased, indicating the charge transfer from NC to MoS_2. Reproduced with permission from ref. 180. Copyright 2018 Royal Society of Chemistry.

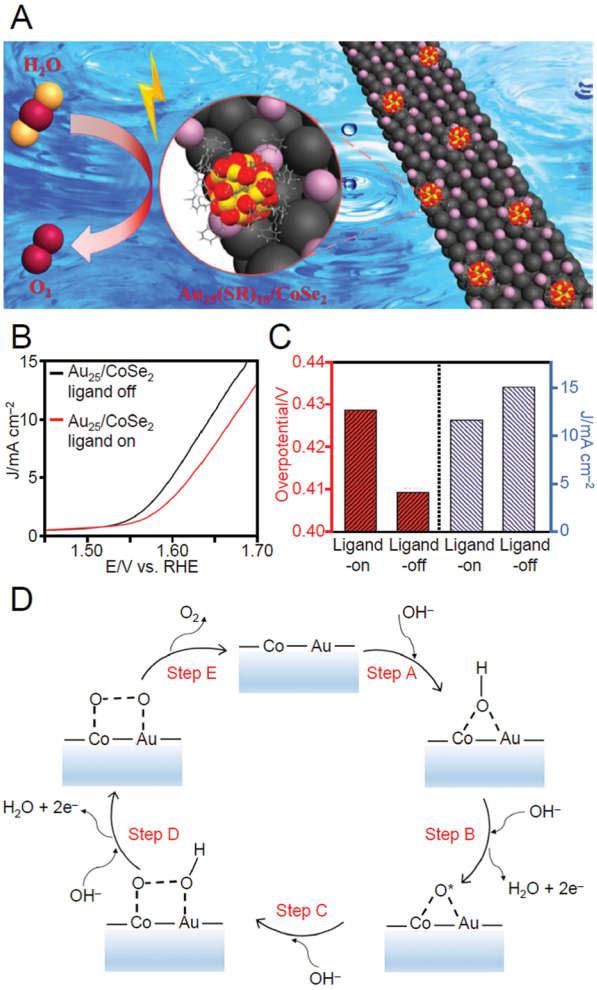


Fig. 32 (A) Schematic of OER on $Au_{25}/CoSe_2$ catalysts. (B) OER polarization curves for ligand-on and ligand-off $Au_{25}/CoSe_2$ catalysts. (C) Comparison of the overpotential (at 10 mA cm^{-2}) and the current density at the overpotential of 0.45 V for ligand-on and ligand-off $Au_{25}/CoSe_2$ catalysts. (D) Proposed mechanisms for OER in the presence of a Au atom on the $CoSe_2$ catalyst surface. Reproduced with permission from ref. 247. Copyright 2017 American Chemical Society.

synthesized in their study, as a metal NC and molybdenum disulfide (MoS_2) having high HER activity as a support.[180] The catalyst was obtained by first adsorbing $Au_2Pd_6S_4(PPh_3)_4(SPhF_2)_6$ on MoS_2 and then calcining the catalysts at 100 °C under Ar atmosphere (Fig. 31A and B). The paper did not refer to whether the ligand was removed by such calcination. The resulting catalyst (hereafter referred to as Au_2Pd_6/MoS_2 regardless of the existence of the ligand) showed higher HER activity than MoS_2, Au_2/MoS_2, Pd_3/MoS_2, and (Au_2 + Pd_3)/MoS_2 (Fig. 31C). Several experiments and density functional theory (DFT) calculation revealed that Au_2Pd_6/MoS_2 exhibited high HER activity because the adsorption site for H atom increased by the charge transfer from Au_2Pd_6 to MoS_2 (Fig. 31D). These results indicate that the loading (or adsorption) of atomically precise metal NCs is also effective for enhancing the functionality of existing HER catalysts.

On the other hand, in 2017, Jin *et al.* succeeded in promoting the OER, which is often a bottleneck in the electrolysis of water, using atomically precise metal NCs (Fig. 32A).[247] In this study, $Au_{25}(PET)_{18}$/diselenium cobalt nanosheets ($CoSe_2$) were first prepared. The obtained $Au_{25}(PET)_{18}/CoSe_2$ showed higher OER activity than catalysts such as $CoSe_2$ and Pt/C. Then, the authors showed that even higher OER activity could be achieved by calcining $Au_{25}(PET)_{18}/CoSe_2$ at 300 °C under N_2 atmosphere (Fig. 32B and C). They interpreted that the OER activity was improved because the electronic interaction between Au NCs (slightly increased in size by calcination) and $CoSe_2$ was increased by calcination of the ligand. They also investigated why the OER activity of the $CoSe_2$ catalyst was improved by

Open Access Article. Published on 12 2021. Downloaded on 02.06.2026 12:22:59.
This article is licensed under a Creative Commons Attribution 3.0 Unported Licence.

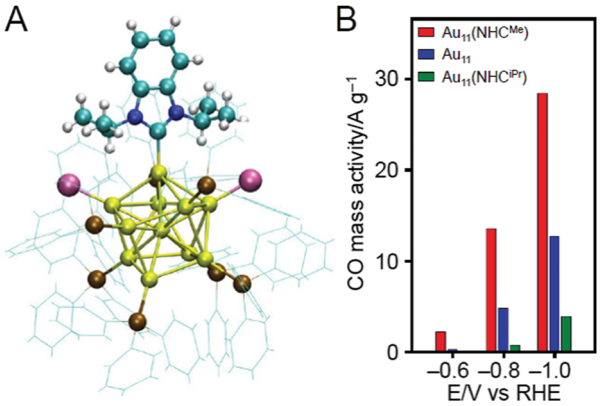


Fig. 33 (A) Geometrical structure of NHC-functionalized Au_{11} NCs. (B) Electrocatalytic activity for the reduction of CO_2 to CO; Au_{11} NCs bearing a methylated NHC (red), Au_{11} NCs without NHC (blue), and Au_{11} NCs bearing an isopropylated NHC (green). Reproduced with permission from ref. 308. Copyright 2019 Springer-Nature.

loading Au NCs by conducting additional experiments and DFT calculation (Fig. 32D). In addition, this study revealed that the OER activity increases with increasing size of Au NCs.

In addition to these photocatalytic water-splitting reactions, Crudden, Tsukuda, and Häkkinen reported the study on the electrocatalytic reduction of CO_2 to CO using N-heterocyclic carbene (NHC)-fuctionalized Au_{11} NCs (Fig. 33A), which was obtained by exchanging the ligand of $[Au_{11}(PPh_3)_8Cl_2]^+$ with N-heterocyclic carbene.[308] This reaction is an important one because CO is the key component in many high-volume carbon–carbon bond-formation reactions. Although the Au NCs did not show the catalytic activity before the calcination, when the phosphine was removed by the calcination at 180 °C for 2 h, the Au NCs showed the catalytic activity for this reaction (Fig. 33A). In this study, they found that Au_{11} NCs bearing a methylated NHC shows an especially high activity (Fig. 33B) and that this high activity is caused by high stability of this NC.

3. Toward the creation of functional heterogeneous catalysts

In this section, we discuss the suitable conditions for catalyst preparation (Section 3.1), the reaction mechanism during the preparation of catalysts (Section 3.2), and the mechanism of catalysis (Section 3.3), which have been clarified in previous studies.

3.1. Suitable experimental conditions

3.1.1. Type of support. The selection of the support is very important for creating highly functional catalysts because the support has a great effect on the electronic state and degree of aggregation of the loaded metal NCs (Fig. 34A).

In most of the previous studies, Au has been used as the base element of the loaded metal NCs. For such NCs, the catalytic activity for oxidation reactions is often improved when CeO_2 (Table 2) is used as a support.[215,217,221,226–233,255] CeO_2 changes the charge state of Au in metal NCs to be cationic and induces O_2

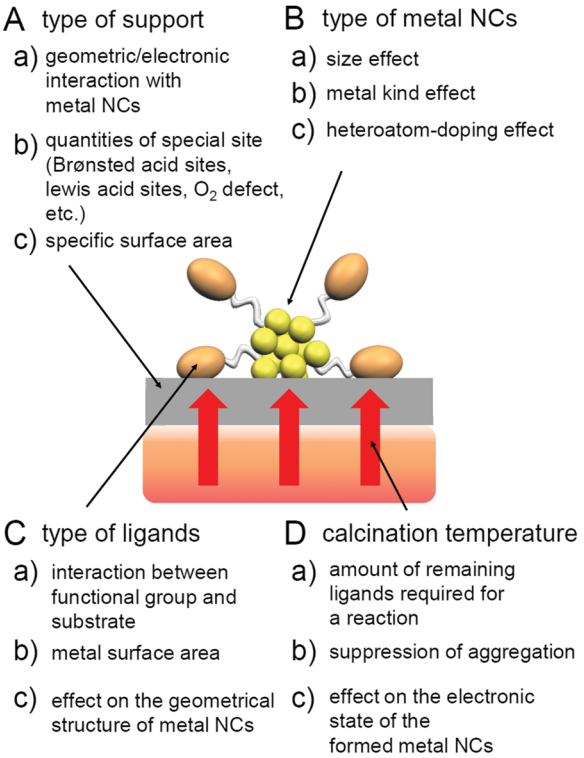


Fig. 34 Important factors to consider in creation of highly functional catalysts.

activation.[231,233] Because of these factors, the oxidation reaction is accelerated when CeO_2 is used as a support. In addition, the aggregation of Au NCs is suppressed on CeO_2 because of the strong interaction between Au NCs and CeO_2.[217,255] Through this means, the highly active Au NCs/CeO_2 can be created without decreasing the unique catalytic activity of small Au NCs. Similar effects were observed when HAP and TiO_2 were used as supports (Table 2).[178,214,216,218–220,223,225,232,236] In contrast, there is very little information on the selection of the support for the reduction reaction because of the limited number of study examples. However, because suppression of aggregation of Au NCs is extremely important in this case as well, a highly active catalyst is often obtained when HAP or TiO_2 is used as the support.[219,223]

Regarding the correlation between the support and the aggregation of Au NCs, Donoeva and Häkkinen *et al.* studied how the behavior of PPh_3-protected Au NCs during calcination changes depending on the type of the support in 2020.[255] In this study, they revealed the following about the behavior of $Au_9(PPh_3)_8$: (1) when SiO_2 containing a Brønsted acid site was used as the support, $Au_9(PPh_3)_8$ dissociated into Au–PPh_3 complexes during calcination because the interaction between $Au_9(PPh_3)_8$ and SiO_2 is weak; and (2) when CeO_2 containing Lewis acid sites was used at the support, the ligand could be removed by calcination from $Au_9(PPh_3)_8$ while maintaining the Au NC size because the interaction between $Au_9(PPh_3)_8$ and CeO_2 is strong. This interpretation was well supported by DFT calculations (Fig. 35A). This study also showed that when TiO_2 containing some Brønsted acid sites and small Lewis acid sites

 This journal is © The Royal Society of Chemistry 2021

Open Access Article. Published on 12 2021. Downloaded on 02.06.2026 12:22:59.
This article is licensed under a Creative Commons Attribution 3.0 Unported Licence.

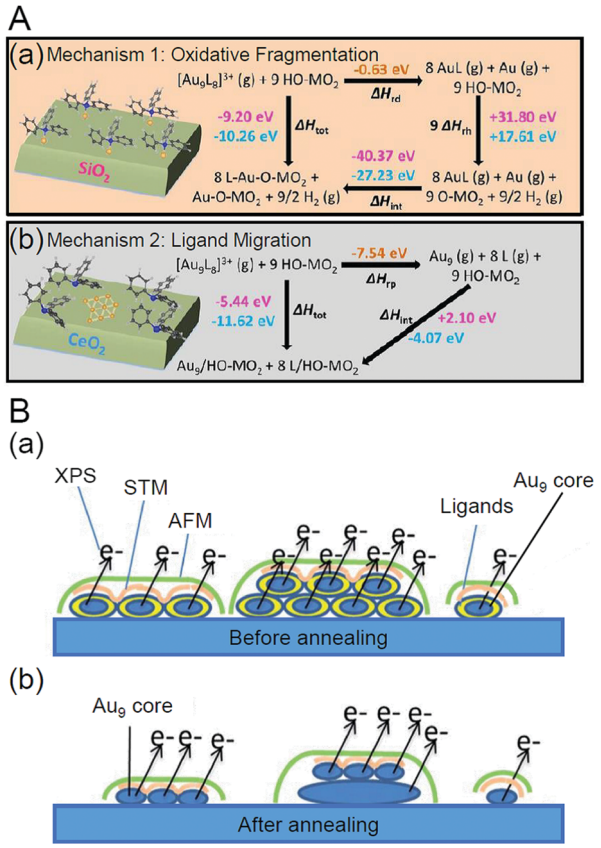


Fig. 35 (A) Born–Haber cycle for (a) oxidative fragmentation and (b) ligand migration for the two supports, HO–SiO_2 and HO–CeO_2. The numbers in pink correspond to values for the hydroxylated amorphous SiO_2 surface, and the numbers in blue correspond to energy values for the hydroxylated CeO_2(111) surface. ΔH_{tot} is the total reaction enthalpy for the processes, ΔH_{rd} is the energy to reduce and disintegrate the cluster into AuL species in the gas phase, ΔH_{rp} is the energy to reduce and peel the ligands from the cluster forming Au_9 and L species in the gas phase, ΔH_{rh} is the energy to remove a H atom from the surface, and ΔH_{int} is the energy due to the interaction between the end species and the surface. Note that the Born–Haber cycle implicitly takes into account the charge imbalance in the total reaction enthalpy ΔH_{tot}. (B) Schematic illustration of gold clusters deposited on titania nanosheet: (a) before annealing and (b) after annealing. The green and orange lines represent the results that can be obtained from atomic force microscopy and scanning tunnel microscopy, respectively. The lines indicating the emission of electrons represent the XPS results. Reproduced with permission from ref. 255 and ref. 311. Copyright 2020 Wiley-VCH and 2016 Royal Society of Chemistry.

was used as a support, little aggregation of Au NCs occurred. This result is generally in good agreement with the series of experimental results (Fig. 35B) reported by Anderson and Nakayama *et al.* from 2013 to 2016.[309–311]

To suppress the aggregation of metal NCs on the support, increasing the specific surface area of the support is also effective (Fig. 34A). As described in Section 2.1.1, Tsukuda *et al.* succeeded in loading ~1 nm Au NCs on SBA-15 without any aggregation.[183] SiO_2 has only weak interaction with Au. However, the SBA-15 used in this study had a high specific surface area (866 $m^2\ g^{-1}$; Table 2); therefore, Au NCs hardly aggregated on the support. The same authors have also successfully suppressed the aggregation of metal NCs on HPCSs (2300 $m^2\ g^{-1}$; Section 2.1.1) and MPC (2300 $m^2\ g^{-1}$; Section 2.1.1).[209,210] It is expected that increase of a high specific surface area leads to the increase of distance between Au NCs on the substrate and thereby the increase of the number of the defects, which well fix the Au NCs on the substrate, between Au NCs. These factors seem to be related to the suppression of the aggregation of the Au NCs on the substrate. Furthermore, Dai *et al.* succeeded in suppressing the aggregation of Au NCs on the support by loading CuO or Co_3O_4 as anchor particles on SBA-15 (395 $m^2\ g^{-1}$).[234] Because the metal NCs do not easily aggregate on these supports, it is possible to increase the amount of metal NCs loaded on them (Table 2). In the future, it is expected that techniques to create supports with high specific surface area will also be established for supports that show the strong interaction with metal NCs. In addition, recent studies have demonstrated that loading metal NCs on layered double hydroxides;[312–314] protecting each metal NC by a silica cage,[315–320] zinc oxide hollow cage,[321] or atomic-layer-deposition of alumina overlayers;[322] and including metal NCs in metal organic frameworks[323–328] are also effective for suppressing the aggregation of metal NCs. Therefore, these techniques are expected to be more widely employed for creating highly functional heterogeneous catalysts using atomically precise metal NCs in the future.

3.1.2. Type of metal NC. Most of the metal NCs used in the previous studies were SR-protected Au NCs,[209–213,215–218,221–231,233,234,236,238–244] most likely for the following reasons: (1) most of the precise synthesis methods established to date are for SR-protected Au NCs; (2) SR-protected Au NCs are stable in both solution and solid state and are easy to handle; and (3) because Au is an inactive metal, it is relatively stable even after ligand elimination.

In terms of the Au NC size that is effective for creating a highly active catalyst (Fig. 34B), previous studies have demonstrated that, overall, small Au NCs show high activity for catalytic reactions.[220,241] However, for benzyl alcohol oxidation, Au_{144} NCs showed highest conversion efficiency[211] and for cyclohexane oxidation, Au_n NCs in the n range of 40–80 showed the highest conversion efficiency.[212]

In terms of metal elements, there are only a few studies on metal NCs consisting of metal elements other than Au. However, for Ag[222,239] and Pt,[235] it has also been shown that when the number of constituent atoms of NCs is reduced to fewer than 50, higher activity can be achieved for some reactions than for NPs with large particle size. In addition, highly active catalysts have been created by heteroatom doping.[209,244] However, to discuss the generality of these effects, it is necessary to conduct studies on metal NCs of various sizes and metal elements in the future.

3.1.3. Type of ligand. The majority of the metal NC ligands used in previous studies have been SRs, most likely for the same reasons described in Section 3.1.2. Among the SRs, PET, alkanethiolate, SPhF, and 2,4-$SPhMe_2$, which are hydrophobic SR, have been most commonly used. Using these ligands, it is possible to size-selectively synthesize stable metal NCs, such as $Au_{25}(SR)_{18}$, $Au_{38}(SR)_{24}$, $Au_{144}(SR)_{60}$, $Ag_{25}(SR)_{18}$, and $Ag_{44}(SR)_{30}$,[200,209–211,213,215–218,220–222,224–229,231,233,234,236,237,239,244] which seems to promote the

Open Access Article. Published on 12 2021. Downloaded on 02.06.2026 12:22:59.
This article is licensed under a Creative Commons Attribution 3.0 Unported Licence.

use of these ligands. The obtained metal NCs are adsorbed on carbon materials such as MWCNTs, HPCSs, and AC in solution with high efficiency *via* hydrophobic or π–π interactions (Fig. 34C). Hydrophobic SR-protected metal NCs also easily adsorb on metal-oxide supports such as CeO_2, Fe_2O_3, TiO_2, and Al_2O_3 in solution *via* dipole-induced dipole interaction. As opposed to metal NCs adsorbed on the support in solution, there have been some cases where metal NCs are deposited on the support by drying the solution containing the metal NCs and support.[215,224,227]

In some studies, hydrophilic SRs, such as SG, have been used as a ligand of metal NCs.[32,96,240–243] When these ligands are used, metal NCs can adsorb on the metal-oxide support with high efficiency *via* hydrogen bond formation in solution. Even for the hydrophobic SR-protected metal NC, when part of the ligands is replaced by hydrophilic ligands, they can be adsorbed and loaded on the metal-oxide support with high efficiency.[244] The catalysts obtained using these methods have the following advantages: (1) it is easy to estimate the quantities of the loaded metal atoms; (2) there is high reproducibility of the metal loading; and (3) it is possible to improve the quantity of the loaded metal atoms.

Meanwhile, when metal NCs are used as catalysts by allowing some or all of the ligands to remain as opposed to removing all of them, the design and selection of the functional group structure of the ligands is more important. In this case, it is necessary to design and select a ligand that can create a suitable structure of the metal NCs[178,221,222,229–231,236] and suitable vacancy size on the surface of metal NCs[231,236] for the desired reaction to proceed (Fig. 34C).

3.1.4. Calcination temperature. The appropriate calcination temperature is strongly related to the type of the proceeded reaction. For example, the presence of ligands leads to reduced activity for alcohol oxidation (Section 2.1.1) and hydrocarbon oxidation (Section 2.1.2) and epoxidation of alkenes (Section 2.1.3).[209,210,212,215,220,222] These phenomena have also been observed in the application of metal NCs as photocatalysts.[241] In contrast, for CO oxidation, the elimination of part of the ligands at moderate calcination temperature tends to induce higher activity than the elimination of all the ligands.[226–229,233] In addition, the selectivity of several reactions has been reported to vary depending on the extent of ligand elimination.[178,209,210] Therefore, the calcination temperature should be selected depending on whether the desired reaction requires ligands (Fig. 34D).

Previous studies have also shown that the temperature required for the ligand elimination varies depending on the type of ligand and support. Thus, in catalyst preparation, it is necessary to know the start temperature of the ligand elimination and the temperature at which the ligand elimination is completed in the studied system in advance.[178,183,209,212,215,218–222,224,226,227] Typically, TGA of unsupported metal NCs is used for this purpose. However, since the support might affect the ligand elimination temperature, it seems to be better to check the presence/absence of metal–ligand bonds by XAFS on the supported metal NCs obtained by the calcination at each temperature. In the calcination, the temperature is typically increased at a heating rate of 10 °C min^{-1} and kept at a certain temperature in the range of 150–500 °C for several hours. The finish temperature should be determined while checking the particle size at each calcination temperature using TEM, HR-TEM, HAADF-STEM, and XPS[309,310] because too high temperature induces the aggregation of metal NCs (Table 3).[178,183,209,210,212,214,216–219,223–225,233,234,236,237,239] It is expected that the elimination speed of the ligands and the electronic state of the formed metal NCs change depending on the calcination atmospheres.[215,222,226,229] In the previous studies, calcination atmospheres such as vacuum, reduced pressure, air, O_2, H_2, and inert gas have been used. However, at present, the effects of the calcination atmosphere on the elimination speed of the ligands and the electronic state of the formed metal NCs remain unclear. Therefore, it is expected that more studies will be conducted to clarify these points in the future.

3.2. Mechanism of calcination

3.2.1. Ligand elimination. In most cases, the purpose of calcination is to remove the ligands from the metal NCs. The ligand-elimination temperature must be determined using TGA with a similar system before the calcination. Then, the temperature is raised to the ligand-elimination temperature using a temperature control program, and heating is continued at an appropriate temperature for several hours. TGA-MS provides information about the chemical composition of the desorbed compounds at each temperature.[226] The ligand elimination is generally confirmed by methods such as XAFS, XPS, STEM-energy dispersive X-ray spectroscopy (EDX), and ICP analyses (Table 3). Weight-loss measurement using TGA can provide information on whether the desorbed ligand has been removed from the system.[178,183,209,212,215,218–222,224,226,227] In recent years, these measurements have revealed that the actual calcination process includes complex processes that were not previously anticipated.[181,329]

As an example, herein, we focus on a system that uses SR-protected Au NCs as the metal NCs. In this case, two patterns of dissociation have been reported on the surface of the Au NCs upon calcination: dissociation of Au–S bonds[209] and dissociation of both Au–S and S–C bonds[210,216] (Fig. 36B). It has been reported in several papers that the ligand elimination occurs in two steps.[209,210,215,216,330] In each paper, different factors have been proposed, such as the difference in the desorption temperature of the ligand between the Au NC–support interface and the surface of the Au NCs[232] or the difference in the desorption temperature of the ligand depending on the S environment owing to the presence of two types of S atom in Au NCs.[184,215] It was previously thought that the dissociated SR or S would be vaporized and eliminated from the system by further heating. However, based on recent results, it is interpreted that SR or S migrate from the surface of the Au NCs onto the support during calcination (Fig. 36B)[216] and are then oxidized to SO_3 or SO_4 on the support (Fig. 36C).[216–218,224] The generated sulfur oxides appear to adsorb on the support *via* dipole–dipole interaction.[314] Tsukuda *et al.* pointed out that desorbed alkyl chains are also adsorbed on carbon supports (Fig. 36B).[209] Barrabés *et al.* noted that Au^+–S^- migrates from Au NCs to the support during calcination (Fig. 36C).[233] When the

 This journal is © The Royal Society of Chemistry 2021

Open Access Article. Published on 12 2021. Downloaded on 02.06.2026 12:22:59.
This article is licensed under a Creative Commons Attribution 3.0 Unported Licence.

Table 3 Characterization methods used in catalyst preparation

Method	Representative purpose
TGA	Check of the temperature at which mass loss starts and finishes
TG/TPD-MS	Track of the desorbed species at each temperature
XPS	Check of the presence and elimination of ligands
	Elucidation of the charge states of metal NCs
	Estimation of the occurring of the aggregation
XAFS	Check of the presence and elimination of ligands
	Elucidation of the charge states of metal NCs
	Elucidation of the interaction between metal NCs and substrate
	Estimation of the particle size and atomic packing structure of the metal NCs (from the average coordination number)
STEM-EDX	Check of the presence and elimination of ligands
	Check of the dispersion of metal NCs on the substrate
TEM	Determination of particle size of metal NCs
HR-TEM/HAADF-STEM	Determination of particle size of metal NCs
	Determination of atomic packing structure of metal NCs
FT-IR/DRIFTS	Estimation of the charge states of each element
	Confirmation of the presence of certain bonds
	Estimation of the specific surface area of metal NCs
ICP-MS/AES/OES	Determination of the quantities of the ligands included in catalysts
	Determination of chemical composition of alloy NCs

calcination temperature is further increased, the S oxides vaporize and are removed from the support (Fig. 36D).[331] Although the results described above were obtained for Au NCs, similar adsorption of S oxides on the support has also been reported by Scott *et al.* during the calcination of $Ag_{25}(2,4\text{-}SPhMe_2)_{18}$/AC.[224] In addition, Adnan *et al.* reported NO_3^- counter anions were also adsorbed on the support when $Au_8(PPh_3)(NO_3)_2$ was used as a precursor.[332]

As shown in Fig. 35A, the behavior of the ligand and metal core during calcination strongly depends on the nature of the support. Therefore, the ligand-elimination mechanism should vary depending on the system used. However, researchers working on other systems should know the above phenomena and the factors that contribute to their occurrence.

3.2.2. Dynamics of metal-core structure. The ligand elimination by calcination also changes the geometrical structure of metal NCs. Kurashige *et al.* reported that bare Au_{25} formed by calcination has a two-dimensionally expanded geometrical structure on $BaLa_4Ti_4O_{15}$ in their study of $Au_{25}/BaLa_4Ti_4O_{15}$, unlike that of the precursor $Au_{25}(PET)_{18}$.[244] The same group also found that in $Au_{24}Pd/BaLa_4Ti_4O_{15}$ and $Au_{24}Pt/BaLa_4Ti_4O_{15}$, where one Au atom in Au_{25} was replaced by Pd or Pt, Pd (Fig. 37A) and Pt (Fig. 37B) were located at the surface of metal NCs and at the interface between metal NCs and $BaLa_4Ti_4O_{15}$, respectively.[244] In the $Au_{24}Pd(SR)_{18}$ and $Au_{24}Pt(SR)_{18}$ precursors, Pd and Pt were located in the center of the metal core (Fig. 2C and O).[26,33,172]

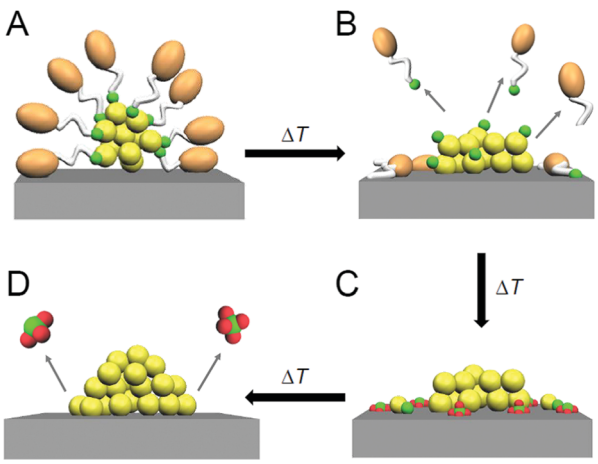


Fig. 36 Schematic of proposed desorption mechanism of the ligand: (A) adsorption of metal NCs on a support, (B) S–C or metal–S dissociation and migration of organic and S-compounds from metal NCs to support, (C) oxidation of S on a support, and (D) desorption of S oxides from a support.

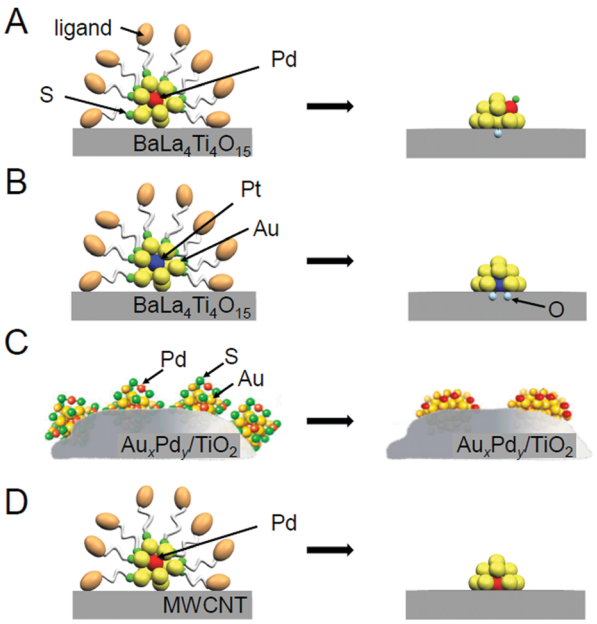


Fig. 37 Illustration of the structure evolution of (A) $Au_{24}Pd$ NCs and (B) $Au_{24}Pt$ NCs supported on $BaLa_4Ti_4O_{15}$ upon calcination, (C) Au_xPd_y NCs supported on TiO_2 upon calcination, and (D) $Au_{24}Pd$ NCs supported on MWCNTs upon calcination. Reproduced with permission from ref. 211, ref. 244 and ref. 335. Copyright 2019 American Chemical Society, 2020 American Chemical Society, and 2013 Royal Society of Chemistry.

Open Access Article. Published on 12 2021. Downloaded on 02.06.2026 12:22:59.
This article is licensed under a Creative Commons Attribution 3.0 Unported Licence.

These results indicate Pd and Pt migrated in the metal NCs during calcination (Fig. 37). Compared with Au, Pt forms a stronger bond with O (318.4 ± 6.7 kJ mol^{-1} for Pt–O *vs.* 223 ± 21.1 kJ mol^{-1} for Au–O) and can bind with a large number of O atoms.[331] This seems to be why Pt migrates to the interface between $Au_{24}Pt$ and $BaLa_4Ti_4O_{15}$ in $Au_{24}Pt/BaLa_4Ti_4O_{15}$ (Fig. 37A). In contrast, Pd forms weaker bonds with O than Au (145 ± 11.1 kJ mol^{-1} for Pd–O *vs.* 223 ± 21.1 kJ mol^{-1} for Au–O).[333] Therefore, the location of Pd at the interface is considered thermodynamically undesirable. However, because Pd has a larger surface energy than Au (2.003 J m^{-2} for Pd (111) surface *vs.* 1.506 J m^{-2} for Au (111) surface),[334] the location of Pd at the metal NC surface is also thermodynamically disadvantageous. In $Au_{24}Pd/BaLa_4Ti_4O_{15}$, the S atom that dissociated from Au during calcination attached on Pd (Fig. 37B),[244] which appears to suppress the destabilization caused by exposure of Pd atom at the NC surface. For $Au_{24}Pd(SR)_{18}$, Barrabés *et al.* also tracked the structural changes of $Au_{24}Pd(SR)_{18}/TiO_2$ during calcination in 2020.[335] In their study, the Pd position within the metal NCs was tracked by operando diffuse reflectance Fourier-transform infrared spectroscopy (DRIFTS), and the results also showed that Pd migrates from the center of the metal core to the surface of the metal core during calcination (Fig. 37C). In contrast, Tsukuda *et al.* reported that in $Au_{24}Pd$/MWCNTs, Pd is located at the interface between $Au_{24}Pd$ and MWCNTs (Fig. 37D).[211] They proposed that because Pd interacts more strongly with C than Au (104.2 kJ mol^{-1} for Pd–C *vs.* 8.68 kJ mol^{-1} for Au–C),[336] such a geometrical structure was formed in the case of $Au_{24}Pd$/MWCNTs. Thus, the ligand elimination induces the reconstruction of metal core and the resulting geometrical structure of metal NCs is largely related to the nature of the used support.

3.3. Mechanism in catalysis

3.3.1. Heterogeneous catalysts with ligands. As described in Section 1.2, the use of atomically precise metal NCs in heterogeneous catalysts is expected to facilitate the identification of active sites and the understanding of reaction mechanisms. The expected results have been obtained for reaction systems that require only a small amount of the ligand elimination. For example, in the case of CO oxidation, when the conventional Au_{NP}/metal oxide with distributed Au_{NP} was used, the complete determination of the active sites was not easy, as it was pointed out that the Au ions on the support may function as the active sites. However, the use of impurity-free Au NCs/metal oxide as catalysts facilitated the determination of the active sites, and the results demonstrated that the reaction was certainly promoted by metallic Au.[226,231,232] For CO oxidation in $Au_n(PET)_m/CeO_2$, several studies have shown that the reaction occurs at the $Au_n(PET)_m$–CeO_2 interface (Fig. 16B)[226,231] and proceeds mainly by the Mars–van Krevelen mechanism (reduction mechanism)[231] (Fig. 18C; Section 2.1.4). In addition, based on the geometrical structures determined by SC-XRD, the details of the reaction mechanisms have been clarified for the styrene oxidation by $Au_n(PET)_m$/HAP (Fig. 13C)[220] and semi-hydrogenation of terminal alkyne compounds by $Au_{25}(PET)_{18}/TiO_2$ (Fig. 23).[236]

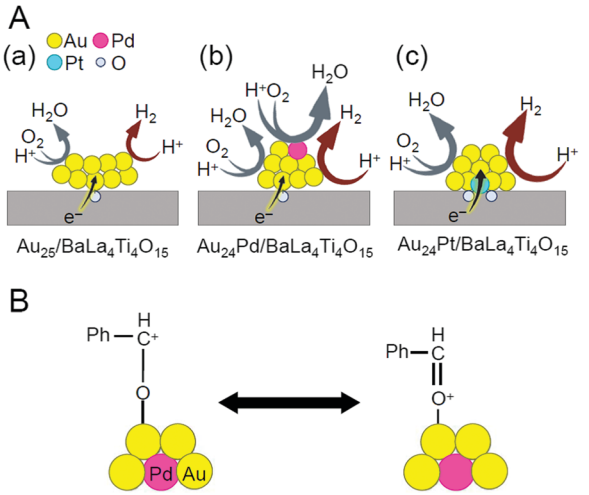


Fig. 38 (A) Proposed structures of $Au_{24}M/BaLa_4Ti_4O_{15}$ for M = (a) Au, (b) Pd, and (c) Pt during the water-splitting reaction. (B) Resonance structures of carbocationic intermediate. Reproduced with permission from ref. 211 and ref. 244. Copyright 2016 Wiley-VCH and 2019 American Chemical Society.

3.3.2. Heterogeneous catalysts without ligands. Even for reaction systems that require ligand elimination, it is possible to identify the metal NCs that induce high activity because the chemical composition of the loaded metal NCs is regulated. In this case, the geometrical structure can also be estimated using methods such as HR-TEM, XAFS, and DRIFTS, which allows for a detailed discussion of the reaction mechanism occurring on the catalyst surface. For the water-splitting reaction over $Au_{25}/BaLa_4Ti_4O_{15}$, it has been revealed that the O_2-photoreduction reaction, which is one of the reverse reactions, proceeds much more easily than the H_2 formation, and therefore suppression of the O_2-photoreduction reaction is extremely important to achieve high activity in this case (Fig. 27).[243–245,286,287] It was also found that in $Au_{24}Pt/BaLa_4Ti_4O_{15}$, Pt located at the interface between $Au_{24}Pt$ and $BaLa_4Ti_4O_{15}$ increases the charge density of Au in the metal NCs and promotes the electron transfer from $BaLa_4Ti_4O_{15}$ to metal NCs; therefore, $Au_{24}Pt/BaLa_4Ti_4O_{15}$ shows higher water-splitting activity than $Au_{25}/BaLa_4Ti_4O_{15}$ (Fig. 38A).[244] For the benzyl alcohol oxidation catalyzed by $Au_{24}Pd$/MWCNTs, electronic/geometrical structures based on experimental and theoretical results imply that the charge transfer from Pd to Au facilitates the stabilization of the reaction intermediates (Fig. 38B); therefore, $Au_{24}Pd$/MWCNTs shows high conversion for this reaction.[211] However, the geometrical structure of metal NCs obtained for these systems is not as certain as that of metal NCs obtained for heterogeneous catalysts containing ligands. In addition, because there are no ligands in these systems, the geometrical structure of the metal NCs is assumed to be largely fluctuating during the reaction. In the future, it is expected that the geometrical structure during the reaction will be clarified through the use of operand measurements and other methods, which will lead to a deeper understanding of the reaction mechanism in such systems (Fig. 39).[335]

 This journal is © The Royal Society of Chemistry 2021

Open Access Article. Published on 12 2021. Downloaded on 02.06.2026 12:22:59.
This article is licensed under a Creative Commons Attribution 3.0 Unported Licence.

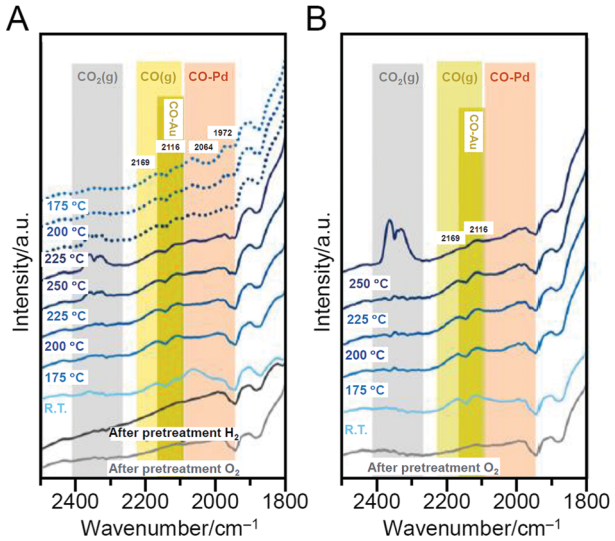


Fig. 39 Results of operando DRIFTS of $Au_{24}Pd/TiO_2$ catalysts during CO oxidation: (A) after the calcination under O_2 atmosphere, followed under H_2 atmosphere and (B) just after the calcination under O_2 atmosphere. Spectra taken upon cooling are indicated by dotted lines. These spectra were acquired in helium at room temperature. Note that the absolute intensities of different samples cannot be compared. Reproduced with permission from ref. 335. Copyright 2020 American Chemical Society.

4. Conclusion

It is essential to continue to develop high-performance catalysts to solve the problems that our society is currently facing and to enrich our lives in the future. From this point of view, atomically precise metal NCs have high potential as components of new functional catalysts. In this review, we have summarized previous studies on the creation of heterogeneous catalysts using atomically precise metal NCs. Through this summary, the current state of research on the development of catalysts using atomically precise metal NCs became clear, as described in the following.

Validity of the use of atomically precise metal NCs

The use of atomically precise metal NCs is effective in elucidating the mechanism of catalytic reactions. Using this route, a deep understanding of the mechanism has been obtained for many reactions, such as CO oxidation by $Au_n(SR)_m/CeO_2$, styrene oxidation by $Au_n(SR)_m$/HAP, semihydrogenation of terminal alkyne compounds by $Au_{25}(PET)_{18}/TiO_2$, photocatalytic water splitting by $Au_{25}/BaLa_4Ti_4O_{15}$, and oxidation of benzyl alcohol by $Au_{24}Pd$/MWCNTs.

Necessity of ligand elimination

The effect of ligand elimination on the conversion efficiency depends on the type of catalytic reaction. However, overall, the ligand-desorbed catalyst exhibits a higher conversion efficiency than the ligand-remaining catalyst. Several recent DFT calculations have predicted that higher activity can be achieved through the elimination of ligands also in the application of metal NCs as electrocatalysts.[337–342] However, there are also reactions in which the presence of ligands leads to an improvement of the conversion efficiency. In addition, the presence of ligands has advantages in changing the reaction selectivity and suppressing aggregation of metal NCs, thereby improving the catalyst durability. Even in these cases, calcination at a low temperature, which does not cause ligand elimination, often induces an improvement in catalytic activity.

Selection of support

To remove the ligands while maintaining the size of the metal NCs, it is necessary to use a support that strongly interacts with the metal NCs. In addition, if a material with a high specific surface area and/or a porous material with an appropriate pore size is used as a support, it is possible to suppress the aggregation of metal NCs. Regarding the suppression of aggregation of metal NCs, the introduction of anchor nanomaterials or atoms,[244] which strongly fix the loaded metal NCs on the support, is also an effective means.

Selection of metal NCs

The appropriate size of Au NCs depends on the type of catalytic reaction. However, overall, a smaller size results in higher activity. Nevertheless, in reactions such as benzyl alcohol oxidation and cyclohexane oxidation, an appropriate Au NC size exists. It is difficult to discuss the size effects of metal NCs other than Au NCs, as well as the doping effects, because of the small number of study examples.

Mechanism in calcination

The calcination process involves a complex process that was not initially predicted. Specifically, calcination first causes dissociation of Au–S bonds and/or S–C bonds on the surface of metal NCs. The dissociated SR or S moves from the Au NC surface to the support during calcination and is then oxidized to SO_3^{2-} and SO_4^{2-} on the support. In a specific system, not only SR and S but also the alkyl chain and Au^+–S^- are transferred to the support. When the calcination temperature is further increased, the sulfur oxide is vaporized and removed from the support. In addition to these processes, when the precursor contains NO_3^-, NO_3^- is also adsorbed on the support. Ligand calcination also induces structural deformation of metal NCs. Along with this, in alloy NCs, heteroatoms change the positions in metal NCs depending on the binding energy with the support.

The above insight is expected to lead to clear design guidelines for the creation of novel heterogeneous catalysts. However, the current knowledge is not presented as a unified view but as a collection of case studies. In the future, it is expected that researchers studying catalysts using metal NCs and/or metal NPs (such as thermal catalysts, photocatalysts, and electrocatalysts) will exchange more information. Such cooperation beyond the fields would enable us to obtain further knowledge on the creation of novel heterogeneous catalysts and make the practical application of heterogeneous catalysts using atomically precise metal NCs more realistic.

Open Access Article. Published on 12 2021. Downloaded on 02.06.2026 12:22:59.
This article is licensed under a Creative Commons Attribution 3.0 Unported Licence.

5. Outlook

It is expected that the following issues will be overcome in the future to enable the creation of various highly functional heterogeneous catalysts using atomically precise metal NCs.

Use of various precise metal NCs

Most of the metal NCs used in the studies of catalysts are the metal NCs shown in Fig. 2. However, in recent years, it has become possible to precisely synthesize metal NCs of various sizes and chemical compositions for both pure metal and alloy NCs.[24,25,87,88] In the future, it is expected that a deeper understanding will be obtained on (1) the correlations among the metal element, size, and catalytic activity, (2) the heteroatom substitution effect,[343] (3) the mechanism in each reaction, (4) the correlations among the metal element, size, and durability by using various metal NCs from such a present ''library'' of atomically precise metal NCs.

Improvement of durability

In most studies, metal NCs aggregate during calcination. In addition, even when the metal NCs can be loaded on the support with the same particle size, the particle size often increases after the catalytic reaction. As described above, increasing the specific surface area of the support is effective in suppressing the aggregation of metal NCs. In the future, it is expected that such ingenious attempts will be applied to various metal-oxide supports. For this purpose, it may be necessary to establish a new preparation method for the support. In addition, it has been reported that the formation of a protective shell on the surface of metal NCs suppresses the aggregation of metal NCs as well as the reverse reaction.[243,275,297] In the future, many protective shells with high transparency of reactants and a small contact area between the metal NCs and films are expected to be newly produced. Also, it is expected that the information about whether further calcination/heat treatment is needed or not before recycling, which is not well understood at present, will be obtained in future study.

Elucidation of geometrical structures of loaded metal NCs

To understand the structure–physical property relationship, it is essential to obtain a deeper understanding of the geometrical structure of the loaded metal NCs. Therefore, it is expected that the geometrical structures of loaded metal NCs will be elucidated by direct observation using spherical aberration-corrected (Cs-corrected) TEM[344] and STEM. In addition, the geometrical structure determined using those methods is not necessarily the same as that present during the catalytic reaction. Therefore, it is expected that operand XAFS measurement[345] will also be widely used for understanding the geometrical structure during catalytic reactions.

Structural control of loaded metal NCs

Regarding the geometrical structure, even if atomically precise metal NCs having no variation in the geometrical structure are used as precursors, variation of the geometrical structure of the loaded metal NCs appears to exist. To identify the geometrical structure of metal NCs that create high activity and thereby selectively load such superior NCs as a catalyst on the support, it is necessary to establish a new method for controlling the geometrical structure of the loaded NCs. Previous studies have established many methods to control the size and geometrical structure of metal NCs dispersed in solution (after-treatment method for as-prepared metal NCs in solution).[87,91,346,347] In the future, it is expected that such after-treatment methods will also be established for the loaded NCs, and thereby control of the geometrical structure could also be realized for the loaded metal NCs.

Perfect elimination of ligands from catalysts

Recent studies have revealed that compounds produced by calcination are not easily removed through vaporization once adsorbed on the support. These compounds seem to (1) cause direct reaction with the reactants to produce by-products, (2) result in the catalyst poisoning that suppresses charge transfer between the support and metal, and (3) affect the catalyst properties. Previous studies have shown that further calcination leads to vaporization of the final products of these compounds (such as SO_3^{2-} and SO_4^{2-}) from supports;[331] however, excessive heating promotes aggregation of metal NCs. Therefore, in the future, it is expected that new elimination methods will be established for compounds generated by calcination, such as chemical washing.

Synthesis of platinum group metal NCs stable in air

In most previous studies, Au has been used as the base element for metal NCs. The superiority of using Au as a catalyst relates to the following factors: (1) Au NCs show high catalytic activity at low temperature; (2) Au NCs exhibit catalytic selectivity different from that of other precious metals; and (3) Au NCs have very low toxicity. However, Au NCs have a low melting point, and their catalytic activities do not improve dramatically even at high temperature. Therefore, it is not suitable to use Au NCs as catalysts at high temperature. For catalysts that must be used at high temperatures, such as catalysts for eliminating automobile exhaust gas, it will be necessary to use metal NCs consisting of elements such as Pt, Pd, and Rh. Although there are many reports of the synthesis of atomically precise metal NCs composed of these metal elements,[53–59] they are difficult to synthesize in the atmosphere. In the future, it is expected that many metal NCs that are stable in the atmosphere will be found for metal NCs consisting of elements such as Pt, Pd, and Rh.

Guidance by DFT calculation

As described above, it has become possible to control the chemical composition of loaded metal NCs with atomic accuracy in recent years. For such heterogeneous catalysts composed of atomically precise metal NCs, DFT calculations may be able to predict highly functional catalyst systems.[337–342,348] Thus, in the future, it is expected that studies for improving the functionality of heterogeneous catalysts will shift from searching for the optimum system based on trial-and-error experiments to prediction by DFT calculation.

 This journal is © The Royal Society of Chemistry 2021

Open Access Article. Published on 12 2021. Downloaded on 02.06.2026 12:22:59.
This article is licensed under a Creative Commons Attribution 3.0 Unported Licence.

If the above problems are overcome, it will be possible to create a heterogeneous catalyst with high activity, selectivity, stability, and durability with a smaller amount of precious metal used, which would help address the resource, energy, and environmental problems currently facing modern society.

Author contributions

Y. N. constructed the structure of this review. T. K., Y. K., M. H., and Y. I. surveyed the literature, compiled figures and tables, and wrote the manuscript. Y. N. and S. H. revised the entire draft before submission. All authors have approved the final version of the manuscript.

Conflicts of interest

There are no conflicts to declare.

Acknowledgements

This work was supported by the Japan Society for the Promotion of Science (JSPS) KAKENHI (grant number 20H02698, 20H02552), Scientific Research on Innovative Areas "Coordination Asymmetry" (grant number 17H05385 and 19H04595), and Scientific Research on Innovative Areas "Innovations for Light-Energy Conversion" (grant number 18H05178 and 20H05115). Funding from Asahi Glass Foundation, TEPCO Memorial Foundation Research Grant (Basic Research), Kato Foundation for Promotion of Science (grant number KJ-2904), and Nissanken are gratefully acknowledged.

References

1 J. N. Galloway, F. J. Dentener, D. G. Capone, E. W. Boyer, R. W. Howarth, S. P. Seitzinger, G. P. Asner, C. C. Cleveland, P. A. Green, E. A. Holland, D. M. Karl, A. F. Michaels, J. H. Porter, A. R. Townsend and C. J. Vörösmarty, *Biogeochemistry*, 2004, **70**, 153–226.
2 J. J. Berzelius, *Ann. Chim.*, 1836, **61**, 146–151.
3 W. Z. Ostwald, *Phys. Chem.*, 1901, **37**, 385.
4 J. T. Richardson, *Principles of Catalyst Development*, Springer, New York, 1989.
5 A. Miyashita, A. Yasuda, H. Takaya, K. Toriumi, T. Ito, T. Souchi and R. Noyori, *J. Am. Chem. Soc.*, 1980, **102**, 7932–7934.
6 M. Haruta, *Catal. Today*, 1997, **36**, 153–166.
7 M. Haruta, N. Yamada, T. Kobayashi and S. Iijima, *J. Catal.*, 1989, **115**, 301–309.
8 J. M. Thomas, R. Raja and D. W. Lewis, *Angew. Chem., Int. Ed.*, 2005, **44**, 6456–6482.
9 U. Hanefeld, *Catalysis: An Integrated Textbook for Students*, ed. L. Lefferts, 2018.
10 T. Tsukuda and H. Häkkinen, *Protected Metal Clusters, From Fundamentals to Applications*, Elsevier, Amsterdam, 2015.
11 M. Agrachev, M. Ruzzi, A. Venzo and F. Maran, *Acc. Chem. Res.*, 2019, **52**, 44–52.
12 K. Kwak and D. Lee, *Acc. Chem. Res.*, 2019, **52**, 12–22.
13 B. Nieto-Ortega and T. Bürgi, *Acc. Chem. Res.*, 2018, **51**, 2811–2819.
14 H. Qian, M. Zhu, Z. Wu and R. Jin, *Acc. Chem. Res.*, 2012, **45**, 1470–1479.
15 N. A. Sakthivel and A. Dass, *Acc. Chem. Res.*, 2018, **51**, 1774–1783.
16 R. L. Whetten, H.-C. Weissker, J. J. Pelayo, S. M. Mullins, X. López-Lozano and I. L. Garzón, *Acc. Chem. Res.*, 2019, **52**, 34–43.
17 T. Tsukuda, *Bull. Chem. Soc. Jpn.*, 2012, **85**, 151–168.
18 B. Bhattarai, Y. Zaker, A. Atnagulov, B. Yoon, U. Landman and T. P. Bigioni, *Acc. Chem. Res.*, 2018, **51**, 3104–3113.
19 Z. Gan, N. Xia and Z. Wu, *Acc. Chem. Res.*, 2018, **51**, 2774–2783.
20 A. Ghosh, O. F. Mohammed and O. M. Bakr, *Acc. Chem. Res.*, 2018, **51**, 3094–3103.
21 S. Hossain, Y. Niihori, L. V. Nair, B. Kumar, W. Kurashige and Y. Negishi, *Acc. Chem. Res.*, 2018, **51**, 3114–3124.
22 J. Yan, B. K. Teo and N. Zheng, *Acc. Chem. Res.*, 2018, **51**, 3084–3093.
23 T. Kawawaki, Y. Imai, D. Suzuki, S. Kato, I. Kobayashi, T. Suzuki, R. Kaneko, S. Hossain and Y. Negishi, *Chem. – Eur. J.*, 2020, **26**, 16150–16193.
24 X. Kang, Y. Li, M. Zhu and R. Jin, *Chem. Soc. Rev.*, 2020, **49**, 6443–6514.
25 S. Bhat, A. Baksi, S. K. Mudedla, G. Natarajan, V. Subramanian and T. Pradeep, *J. Phys. Chem. Lett.*, 2017, **8**, 2787–2793.
26 S. Tian, L. Liao, J. Yuan, C. Yao, J. Chen, J. Yang and Z. Wu, *Chem. Commun.*, 2016, **52**, 9873–9876.
27 S. Yamazoe, W. Kurashige, K. Nobusada, Y. Negishi and T. Tsukuda, *J. Phys. Chem. C*, 2014, **118**, 25284–25290.
28 C. Kumara, C. M. Aikens and A. Dass, *J. Phys. Chem. Lett.*, 2014, **5**, 461–466.
29 C. Yao, Y.-j. Lin, J. Yuan, L. Liao, M. Zhu, L.-h. Weng, J. Yang and Z. Wu, *J. Am. Chem. Soc.*, 2015, **137**, 15350–15353.
30 W. Fei, S. Antonello, T. Dainese, A. Dolmella, M. Lahtinen, K. Rissanen, A. Venzo and F. Maran, *J. Am. Chem. Soc.*, 2019, **141**, 16033–16045.
31 C. Sun, N. Mammen, S. Kaappa, P. Yuan, G. Deng, C. Zhao, J. Yan, S. Malola, K. Honkala, H. Häkkinen, B. K. Teo and N. Zheng, *ACS Nano*, 2019, **13**, 5975–5986.
32 S. Lee, M. S. Bootharaju, G. Deng, S. Malola, W. Baek, H. Häkkinen, N. Zheng and T. Hyeon, *J. Am. Chem. Soc.*, 2020, **142**, 13974–13981.
33 W. Kurashige, S. Yamazoe, M. Yamaguchi, K. Nishido, K. Nobusada, T. Tsukuda and Y. Negishi, *J. Phys. Chem. Lett.*, 2014, **5**, 2072–2076.
34 S. Sharma, W. Kurashige, K. Nobusada and Y. Negishi, *Nanoscale*, 2015, **7**, 10606–10612.
35 Y. Niihori, M. Eguro, A. Kato, S. Sharma, B. Kumar, W. Kurashige, K. Nobusada and Y. Negishi, *J. Phys. Chem. C*, 2016, **120**, 14301–14309.

Open Access Article. Published on 12 2021. Downloaded on 02.06.2026 12:22:59.
This article is licensed under a Creative Commons Attribution 3.0 Unported Licence.

36 Y. Niihori, S. Hossain, B. Kumar, L. V. Nair, W. Kurashige and Y. Negishi, *APL Mater.*, 2017, **5**, 053201.
37 L. V. Nair, S. Hossain, S. Takagi, Y. Imai, G. Hu, S. Wakayama, B. Kumar, W. Kurashige, D.-e. Jiang and Y. Negishi, *Nanoscale*, 2018, **10**, 18969–18979.
38 S. Hossain, Y. Imai, D. Suzuki, W. Choi, Z. Chen, T. Suzuki, M. Yoshioka, T. Kawawaki, D. Lee and Y. Negishi, *Nanoscale*, 2019, **11**, 22089–22098.
39 S. Hossain, Y. Imai, Y. Motohashi, Z. Chen, D. Suzuki, T. Suzuki, Y. Kataoka, M. Hirata, T. Ono, W. Kurashige, T. Kawawaki, T. Yamamoto and Y. Negishi, *Mater. Horiz.*, 2020, **7**, 796–803.
40 S. Hossain, T. Ono, M. Yoshioka, G. Hu, M. Hosoi, Z. Chen, L. V. Nair, Y. Niihori, W. Kurashige, D.-e. Jiang and Y. Negishi, *J. Phys. Chem. Lett.*, 2018, **9**, 2590–2594.
41 P. D. Jadzinsky, G. Calero, C. J. Ackerson, D. A. Bushnell and R. D. Kornberg, *Science*, 2007, **318**, 430–433.
42 M. Zhu, C. M. Aikens, F. J. Hollander, G. C. Schatz and R. Jin, *J. Am. Chem. Soc.*, 2008, **130**, 5883–5885.
43 C. P. Joshi, M. S. Bootharaju, M. J. Alhilaly and O. M. Bakr, *J. Am. Chem. Soc.*, 2015, **137**, 11578–11581.
44 H. Yang, Y. Wang, H. Huang, L. Gell, L. Lehtovaara, S. Malola, H. Häkkinen and N. Zheng, *Nat. Commun.*, 2013, **4**, 2422.
45 B. Kumar, T. Kawawaki, N. Shimizu, Y. Imai, D. Suzuki, S. Hossain, L. V. Nair and Y. Negishi, *Nanoscale*, 2020, **12**, 9969–9979.
46 Y. Negishi, S. Hashimoto, A. Ebina, K. Hamada, S. Hossain and T. Kawawaki, *Nanoscale*, 2020, **12**, 8017–8039.
47 C. E. Briant, B. R. C. Theobald, J. W. White, L. K. Bell, D. M. P. Mingos and A. J. Welch, *J. Chem. Soc., Chem. Commun.*, 1981, 201–202.
48 M. McPartlin, R. Mason and L. Malatesta, *J. Chem. Soc. D*, 1969, 334.
49 G. Schmid, *Chem. Rev.*, 1992, **92**, 1709–1727.
50 M. Schulz-Dobrick and M. Jansen, *Z. Anorg. Allg. Chem.*, 2007, **633**, 2326–2331.
51 B. K. Teo, X. Shi and H. Zhang, *J. Am. Chem. Soc.*, 1992, **114**, 2743–2745.
52 J. D. Roth, G. J. Lewis, L. K. Safford, X. Jiang, L. F. Dahl and M. J. Weaver, *J. Am. Chem. Soc.*, 1992, **114**, 6159–6169.
53 Y. Shichibu and K. Konishi, *Small*, 2010, **6**, 1216–1220.
54 H. Hirai, S. Takano, T. Nakamura and T. Tsukuda, *Inorg. Chem.*, 2020, **59**, 17889–17895.
55 K. Konishi, M. Iwasaki and Y. Shichibu, *Acc. Chem. Res.*, 2018, **51**, 3125–3133.
56 B. K. Teo and H. Zhang, *Proc. Natl. Acad. Sci. U. S. A.*, 1991, **88**, 5067–5071.
57 V. G. Albano, P. L. Bellon, M. Manassero and M. Sansoni, *J. Chem. Soc. D*, 1970, 1210–1211.
58 G. Schmid, R. Pfeil, R. Boese, F. Bandermann, S. Meyer, G. H. M. Calis and J. W. A. van der Velden, *Chem. Ber.*, 1981, **114**, 3634–3642.
59 E. G. Mednikov and L. F. Dahl, *Philos. Trans. R. Soc., A*, 2010, **368**, 1301–1332.
60 A. Ceriotti, N. Masciocchi, P. Macchi and G. Longoni, *Angew. Chem., Int. Ed.*, 1999, **38**, 3724–3727.
61 I. Ciabatti, C. Femoni, M. C. Iapalucci, G. Longoni and S. Zacchini, *J. Cluster Sci.*, 2014, **25**, 115–146.
62 S. S. Kurasov, N. K. Eremenko, Y. L. Slovokhotov and Y. T. Struchkov, *J. Organomet. Chem.*, 1989, **361**, 405–408.
63 L. Hao, G. J. Spivak, J. Xiao, J. J. Vittal and R. J. Puddephatt, *J. Am. Chem. Soc.*, 1995, **117**, 7011–7012.
64 E. Cattabriga, I. Ciabatti, C. Femoni, T. Funaioli, M. C. Iapalucci and S. Zacchini, *Inorg. Chem.*, 2016, **55**, 6068–6079.
65 C. Cesari, I. Ciabatti, C. Femoni, M. C. Iapalucci, F. Mancini and S. Zacchini, *Inorg. Chem.*, 2017, **56**, 1655–1668.
66 P. Chini, *J. Organomet. Chem.*, 1980, **200**, 37–61.
67 M. Paolieri, I. Ciabatti and M. Fontani, *J. Cluster Sci.*, 2019, **30**, 1623–1631.
68 M. Brust, M. Walker, D. Bethell, D. J. Schiffrin and R. Whyman, *J. Chem. Soc., Chem. Commun.*, 1994, 801–802.
69 Y. Negishi, K. Nobusada and T. Tsukuda, *J. Am. Chem. Soc.*, 2005, **127**, 5261–5270.
70 A. Baksi, M. S. Bootharaju, X. Chen, H. Häkkinen and T. Pradeep, *J. Phys. Chem. C*, 2014, **118**, 21722–21729.
71 I. Chakraborty, W. Kurashige, K. Kanehira, L. Gell, H. Häkkinen, Y. Negishi and T. Pradeep, *J. Phys. Chem. Lett.*, 2013, **4**, 3351–3355.
72 K. S. Sugi, I. Chakraborty, T. Udayabhaskararao, J. S. Mohanty and T. Pradeep, *Part. Part. Syst. Charact.*, 2013, **30**, 241–243.
73 Z. Lei, X.-K. Wan, S.-F. Yuan, Z.-J. Guan and Q.-M. Wang, *Acc. Chem. Res.*, 2018, **51**, 2465–2474.
74 J.-J. Li, Z.-J. Guan, Z. Lei, F. Hu and Q.-M. Wang, *Angew. Chem., Int. Ed.*, 2019, **58**, 1083–1087.
75 X.-K. Wan, Q. Tang, S.-F. Yuan, D.-e. Jiang and Q.-M. Wang, *J. Am. Chem. Soc.*, 2015, **137**, 652–655.
76 S. Ito, S. Takano and T. Tsukuda, *J. Phys. Chem. Lett.*, 2019, **10**, 6892–6896.
77 Y. Negishi, W. Kurashige and U. Kamimura, *Langmuir*, 2011, **27**, 12289–12292.
78 W. Kurashige, M. Yamaguchi, K. Nobusada and Y. Negishi, *J. Phys. Chem. Lett.*, 2012, **3**, 2649–2652.
79 W. Kurashige, K. Munakata, K. Nobusada and Y. Negishi, *Chem. Commun.*, 2013, **49**, 5447–5449.
80 W. Kurashige, S. Yamazoe, K. Kanehira, T. Tsukuda and Y. Negishi, *J. Phys. Chem. Lett.*, 2013, **4**, 3181–3185.
81 W. Kurashige, Y. Niihori, S. Sharma and Y. Negishi, *J. Phys. Chem. Lett.*, 2014, **5**, 4134–4142.
82 S. Hossain, W. Kurashige, S. Wakayama, B. Kumar, L. V. Nair, Y. Niihori and Y. Negishi, *J. Phys. Chem. C*, 2016, **120**, 25861–25869.
83 Y. Niihori, S. Hossain, S. Sharma, B. Kumar, W. Kurashige and Y. Negishi, *Chem. Rec.*, 2017, **17**, 473–484.
84 X. Kang and M. Zhu, *Small*, 2019, **15**, 1902703.
85 T. Kawawaki, A. Ebina, Y. Hosokawa, S. Ozaki, D. Suzuki, S. Hossain and Y. Negishi, *Small*, 2021, 2005328.
86 Y. Du, H. Sheng, D. Astruc and M. Zhu, *Chem. Rev.*, 2020, **120**, 526–622.
87 R. Jin, C. Zeng, M. Zhou and Y. Chen, *Chem. Rev.*, 2016, **116**, 10346–10413.

 This journal is © The Royal Society of Chemistry 2021

Open Access Article. Published on 12 2021. Downloaded on 02.06.2026 12:22:59.
This article is licensed under a Creative Commons Attribution 3.0 Unported Licence.

88 I. Chakraborty and T. Pradeep, *Chem. Rev.*, 2017, **117**, 8208–8271.
89 A. Ebina, S. Hossain, H. Horihata, S. Ozaki, S. Kato, T. Kawawaki and Y. Negishi, *Nanomaterials*, 2020, **10**, 1105.
90 X. Kang, H. Chong and M. Zhu, *Nanoscale*, 2018, **10**, 10758–10834.
91 X. Kang and M. Zhu, *Chem. Mater.*, 2019, **31**, 9939–9969.
92 X. Kang and M. Zhu, *Coord. Chem. Rev.*, 2019, **394**, 1–38.
93 X. Kang and M. Zhu, *Chem. Soc. Rev.*, 2019, **48**, 2422–2457.
94 H. Yu, B. Rao, W. Jiang, S. Yang and M. Zhu, *Coord. Chem. Rev.*, 2019, **378**, 595–617.
95 T. Omoda, S. Takano and T. Tsukuda, *Small*, 2020, 2001439.
96 Y. Zhu, H. Qian, B. A. Drake and R. Jin, *Angew. Chem., Int. Ed.*, 2010, **49**, 1295–1298.
97 G. Li, C. Zeng and R. Jin, *J. Am. Chem. Soc.*, 2014, **136**, 3673–3679.
98 Y. Negishi, W. Kurashige, Y. Niihori, T. Iwasa and K. Nobusada, *Phys. Chem. Chem. Phys.*, 2010, **12**, 6219–6225.
99 Y. Negishi, T. Iwai and M. Ide, *Chem. Commun.*, 2010, **46**, 4713–4715.
100 Y. Negishi, R. Arai, Y. Niihori and T. Tsukuda, *Chem. Commun.*, 2011, **47**, 5693–5695.
101 Y. Negishi, K. Igarashi, K. Munakata, W. Ohgake and K. Nobusada, *Chem. Commun.*, 2012, **48**, 660–662.
102 W. Kurashige and Y. Negishi, *J. Cluster Sci.*, 2012, **23**, 365–374.
103 Y. Negishi, U. Kamimura, M. Ide and M. Hirayama, *Nanoscale*, 2012, **4**, 4263–4268.
104 Y. Negishi, K. Munakata, W. Ohgake and K. Nobusada, *J. Phys. Chem. Lett.*, 2012, **3**, 2209–2214.
105 Y. Niihori, W. Kurashige, M. Matsuzaki and Y. Negishi, *Nanoscale*, 2013, **5**, 508–512.
106 Y. Negishi, W. Kurashige, Y. Kobayashi, S. Yamazoe, N. Kojima, M. Seto and T. Tsukuda, *J. Phys. Chem. Lett.*, 2013, **4**, 3579–3583.
107 Y. Negishi, W. Kurashige, Y. Niihori and K. Nobusada, *Phys. Chem. Chem. Phys.*, 2013, **15**, 18736–18751.
108 A. Puls, P. Jerabek, W. Kurashige, M. Förster, M. Molon, T. Bollermann, M. Winter, C. Gemel, Y. Negishi, G. Frenking and R. A. Fischer, *Angew. Chem., Int. Ed.*, 2014, **53**, 4327–4331.
109 D. Bahnemann, A. Henglein, J. Lilie and L. Spanhel, *J. Phys. Chem.*, 1984, **88**, 709–711.
110 H. N. Ghosh, J. B. Asbury and T. Lian, *J. Phys. Chem. B*, 1998, **102**, 6482–6486.
111 B. Ohtani, R. M. Bowman, D. P. Colombo Jr., H. Kominami, H. Noguchi and K. Uosaki, *Chem. Lett.*, 1998, 579–580.
112 A. Yamakata, T.-a. Ishibashi and H. Onishi, *Chem. Phys. Lett.*, 2001, **333**, 271–277.
113 T. Yoshihara, R. Katoh, A. Furube, Y. Tamaki, M. Murai, K. Hara, S. Murata, H. Arakawa and M. Tachiya, *J. Phys. Chem. B*, 2004, **108**, 3817–3823.
114 J. Lee, H. S. Shim, M. Lee, J. K. Song and D. Lee, *J. Phys. Chem. Lett.*, 2011, **2**, 2840–2845.
115 X.-Q. Gong, A. Selloni, O. Dulub, P. Jacobson and U. Diebold, *J. Am. Chem. Soc.*, 2008, **130**, 370–381.
116 M. R. Nellist, F. A. L. Laskowski, J. Qiu, H. Hajibabaei, K. Sivula, T. W. Hamann and S. W. Boettcher, *Nat. Energy*, 2018, **3**, 46–52.
117 M. R. Nellist, J. Qiu, F. A. L. Laskowski, F. M. Toma and S. W. Boettcher, *ACS Energy Lett.*, 2018, **3**, 2286–2291.
118 G. N. Vayssilov, Y. Lykhach, A. Migani, T. Staudt, G. P. Petrova, N. Tsud, T. Skála, A. Bruix, F. Illas, K. C. Prince, V. Matolin, K. M. Neyman and J. Libuda, *Nat. Mater.*, 2011, **10**, 310–315.
119 K. He, J. Xie, Z.-Q. Liu, N. Li, X. Chen, J. Hu and X. Li, *J. Mater. Chem. A*, 2018, **6**, 13110–13122.
120 Y. Niihori, K. Yoshida, S. Hossain, W. Kurashige and Y. Negishi, *Bull. Chem. Soc. Jpn.*, 2019, **92**, 664–695.
121 S. Wang, X. Meng, A. Das, T. Li, Y. Song, T. Cao, X. Zhu, M. Zhu and R. Jin, *Angew. Chem., Int. Ed.*, 2014, **53**, 2376–2380.
122 J. Chen, L. Liu, X. Liu, L. Liao, S. Zhuang, S. Zhou, J. Yang and Z. Wu, *Chem. – Eur. J.*, 2017, **23**, 18187–18192.
123 R. Anumula, P. Xiao, C. Cui, H. Wu, G. Cui, W.-H. Fang, Z. Luo and J. Yao, *Nanoscale*, 2020, **12**, 7864–7869.
124 S. R. Biltek, A. C. Reber, S. N. Khanna and A. Sen, *J. Phys. Chem. A*, 2017, **121**, 5324–5331.
125 G. Sun, X. Kang, S. Jin, X. Li, D. Hu, S. Wang and M. Zhu, *Acta Phys.-Chim. Sin.*, 2018, **34**, 799–804.
126 X. Liu, J. Yuan, J. Chen, J. Yang and Z. Wu, *Part. Part. Syst. Charact.*, 2019, **36**, 1900003.
127 X. Kang, S. Wang, Y. Song, S. Jin, G. Sun, H. Yu and M. Zhu, *Angew. Chem., Int. Ed.*, 2016, **55**, 3611–3614.
128 H. Yang, Y. Wang, J. Lei, L. Shi, X. Wu, V. Mäkinen, S. Lin, Z. Tang, J. He, H. Häkkinen, L. Zheng and N. Zheng, *J. Am. Chem. Soc.*, 2013, **135**, 9568–9571.
129 M.-b. Li, S.-k. Tian and Z. Wu, *Chin. J. Chem.*, 2017, **35**, 567–571.
130 C. Zhou, H. Li, Y. Song, F. Ke, W. W. Xu and M. Zhu, *Nanoscale*, 2019, **11**, 19393–19397.
131 R. Anumula, A. C. Reber, P. An, C. Cui, M. Guo, H. Wu, Z. Luo and S. N. Khanna, *Nanoscale*, 2020, **12**, 14801–14807.
132 X. Kang, L. Xiong, S. Wang, Y. Pei and M. Zhu, *Inorg. Chem.*, 2018, **57**, 335–342.
133 J. Xiang, P. Li, Y. Song, X. Liu, H. Chong, S. Jin, Y. Pei, X. Yuan and M. Zhu, *Nanoscale*, 2015, **7**, 18278–18283.
134 X. Kang, C. Silalai, Y. Lv, G. Sun, S. Chen, H. Yu, F. Xu and M. Zhu, *Eur. J. Inorg. Chem.*, 2017, 1414–1419.
135 Y. Song, S. Weng, H. Li, H. Yu and M. Zhu, *Inorg. Chem.*, 2019, **58**, 7136–7140.
136 Q. Li, K. J. Lambright, M. G. Taylor, K. Kirschbaum, T.-Y. Luo, J. Zhao, G. Mpourmpakis, S. Mokashi-Punekar, N. L. Rosi and R. Jin, *J. Am. Chem. Soc.*, 2017, **139**, 17779–17782.
137 S. Yang, J. Chai, Y. Song, J. Fan, T. Chen, S. Wang, H. Yu, X. Li and M. Zhu, *J. Am. Chem. Soc.*, 2017, **139**, 5668–5671.
138 T.-H. Chiu, J.-H. Liao, F. Gam, I. Chantrenne, S. Kahlal, J.-Y. Saillard and C. W. Liu, *J. Am. Chem. Soc.*, 2019, **141**, 12957–12961.
139 C. Yao, C.-Q. Xu, I.-H. Park, M. Zhao, Z. Zhu, J. Li, X. Hai, H. Fang, Y. Zhang, G. Macam, J. Teng, L. Li, Q.-H. Xu, F.-C. Chuang, J. Lu, C. Su, J. Li and J. Lu, *Angew. Chem., Int. Ed.*, 2020, **59**, 8270–8276.

Open Access Article. Published on 12 2021. Downloaded on 02.06.2026 12:22:59.
This article is licensed under a Creative Commons Attribution 3.0 Unported Licence.

140 Q. Li, T.-Y. Luo, M. G. Taylor, S. Wang, X. Zhu, Y. Song, G. Mpourmpakis, N. L. Rosi and R. Jin, *Sci. Adv.*, 2017, **3**, e1603193.
141 Y. Li, M. J. Cowan, M. Zhou, M. G. Taylor, H. Wang, Y. Song, G. Mpourmpakis and R. Jin, *ACS Nano*, 2020, **14**, 6599–6606.
142 Q. Li, M. G. Taylor, K. Kirschbaum, K. J. Lambright, X. Zhu, G. Mpourmpakis and R. Jin, *J. Colloid Interface Sci.*, 2017, **505**, 1202–1207.
143 S. Takano, S. Ito and T. Tsukuda, *J. Am. Chem. Soc.*, 2019, **141**, 15994–16002.
144 H. Yang, Y. Wang, J. Yan, X. Chen, X. Zhang, H. Häkkinen and N. Zheng, *J. Am. Chem. Soc.*, 2014, **136**, 7197–7200.
145 L. Liao, S. Zhou, Y. Dai, L. Liu, C. Yao, C. Fu, J. Yang and Z. Wu, *J. Am. Chem. Soc.*, 2015, **137**, 9511–9514.
146 J. Yan, H. Su, H. Yang, S. Malola, S. Lin, H. Häkkinen and N. Zheng, *J. Am. Chem. Soc.*, 2015, **137**, 11880–11883.
147 Q. Li, S. Wang, K. Kirschbaum, K. J. Lambright, A. Das and R. Jin, *Chem. Commun.*, 2016, **52**, 5194–5197.
148 N. Yan, L. Liao, J. Yuan, Y.-j. Lin, L.-h. Weng, J. Yang and Z. Wu, *Chem. Mater.*, 2016, **28**, 8240–8247.
149 M. S. Bootharaju, C. P. Joshi, M. R. Parida, O. F. Mohammed and O. M. Bakr, *Angew. Chem., Int. Ed.*, 2016, **55**, 922–926.
150 S. Wang, H. Abroshan, C. Liu, T.-Y. Luo, M. Zhu, H. J. Kim, N. L. Rosi and R. Jin, *Nat. Commun.*, 2017, **8**, 848.
151 S. Yang, J. Chai, T. Chen, B. Rao, Y. Pan, H. Yu and M. Zhu, *Inorg. Chem.*, 2017, **56**, 1771–1774.
152 L. He, J. Yuan, N. Xia, L. Liao, X. Liu, Z. Gan, C. Wang, J. Yang and Z. Wu, *J. Am. Chem. Soc.*, 2018, **140**, 3487–3490.
153 G. Soldan, M. A. Aljuhani, M. S. Bootharaju, L. G. AbdulHalim, M. R. Parida, A.-H. Emwas, O. F. Mohammed and O. M. Bakr, *Angew. Chem., Int. Ed.*, 2016, **55**, 5749–5753.
154 X. Kang, H. Abroshan, S. Wang and M. Zhu, *Inorg. Chem.*, 2019, **58**, 11000–11009.
155 X. Kang, X. Wei, S. Wang and M. Zhu, *Inorg. Chem.*, 2020, **59**, 8736–8743.
156 J. Chai, S. Yang, Y. Lv, H. Chong, H. Yu and M. Zhu, *Angew. Chem., Int. Ed.*, 2019, **58**, 15671–15674.
157 W. Zhang, S. Zhuang, L. Liao, H. Dong, N. Xia, J. Li, H. Deng and Z. Wu, *Inorg. Chem.*, 2019, **58**, 5388–5392.
158 X. Zou, S. Jin, S. Wang, M. Zhu and R. Jin, *Nano Futures*, 2018, **2**, 045004.
159 J. Fan, Y. Song, J. Chai, S. Yang, T. Chen, B. Rao, H. Yu and M. Zhu, *Nanoscale*, 2016, **8**, 15317–15322.
160 B. Rao, T. Zhao, S. Yang, J. Chai, Y. Pan, S. Weng, H. Yu, X. Li and M. Zhu, *Dalton Trans.*, 2018, **47**, 475–480.
161 N. A. Sakthivel, M. Stener, L. Sementa, M. Medves, G. Ramakrishna, A. Fortunelli, A. G. Oliver and A. Dass, *J. Phys. Chem. C*, 2019, **123**, 29484–29494.
162 C. Kumara, K. J. Gagnon and A. Dass, *J. Phys. Chem. Lett.*, 2015, **6**, 1223–1228.
163 J. Chai, Y. Lv, S. Yang, Y. Song, X. Zan, Q. Li, H. Yu, M. Wu and M. Zhu, *J. Phys. Chem. C*, 2017, **121**, 21665–21669.
164 J. Yan, H. Su, H. Yang, C. Hu, S. Malola, S. Lin, B. K. Teo, H. Häkkinen and N. Zheng, *J. Am. Chem. Soc.*, 2016, **138**, 12751–12754.
165 L. Huang, J. Yan, L. Ren, B. K. Teo and N. Zheng, *Dalton Trans.*, 2017, **46**, 1757–1760.
166 J. Yan, S. Malola, C. Hu, J. Peng, B. Dittrich, B. K. Teo, H. Häkkinen, L. Zheng and N. Zheng, *Nat. Commun.*, 2018, **9**, 3357.
167 S. Zhuang, D. Chen, L. Liao, Y. Zhao, N. Xia, W. Zhang, C. Wang, J. Yang and Z. Wu, *Angew. Chem., Int. Ed.*, 2020, **59**, 3073–3077.
168 S. Jin, M. Zhou, X. Kang, X. Li, W. Du, X. Wei, S. Chen, S. Wang and M. Zhu, *Angew. Chem., Int. Ed.*, 2020, **59**, 3891–3895.
169 S. Wang, S. Jin, S. Yang, S. Chen, Y. Song, J. Zhang and M. Zhu, *Sci. Adv.*, 2015, **1**, e1500441.
170 T. Higaki, C. Liu, D. J. Morris, G. He, T.-Y. Luo, M. Y. Sfeir, P. Zhang, N. L. Rosi and R. Jin, *Angew. Chem., Int. Ed.*, 2019, **58**, 18798–18802.
171 L. C. McKenzie, T. O. Zaikova and J. E. Hutchison, *J. Am. Chem. Soc.*, 2014, **136**, 13426–13435.
172 M. A. Tofanelli, T. W. Ni, B. D. Phillips and C. J. Ackerson, *Inorg. Chem.*, 2016, **55**, 999–1001.
173 H. Qian, W. T. Eckenhoff, Y. Zhu, T. Pintauer and R. Jin, *J. Am. Chem. Soc.*, 2010, **132**, 8280–8281.
174 N. Yan, N. Xia, L. Liao, M. Zhu, F. Jin, R. Jin and Z. Wu, *Sci. Adv.*, 2018, **4**, eaat7259.
175 Y. Shichibu, Y. Negishi, T. Watanabe, N. K. Chaki, H. Kawaguchi and T. Tsukuda, *J. Phys. Chem. C*, 2007, **111**, 7845–7847.
176 J. Chen, Q.-F. Zhang, T. A. Bonaccorso, P. G. Williard and L.-S. Wang, *J. Am. Chem. Soc.*, 2014, **136**, 92–95.
177 L. V. Nair, S. Hossain, S. Wakayama, S. Takagi, M. Yoshioka, J. Maekawa, A. Harasawa, B. Kumar, Y. Niihori, W. Kurashige and Y. Negishi, *J. Phys. Chem. C*, 2017, **121**, 11002–11009.
178 X.-K. Wan, J.-Q. Wang, Z.-A. Nan and Q.-M. Wang, *Sci. Adv.*, 2017, **3**, e1701823.
179 X. Liu, J. Yuan, C. Yao, J. Chen, L. Li, X. Bao, J. Yang and Z. Wu, *J. Phys. Chem. C*, 2017, **121**, 13848–13853.
180 Y. Du, J. Xiang, K. Ni, Y. Yun, G. Sun, X. Yuan, H. Sheng, Y. Zhu and M. Zhu, *Inorg. Chem. Front.*, 2018, **5**, 2948–2954.
181 V. Sudheeshkumar, K. O. Sulaiman and R. W. J. Scott, *Nanoscale Adv.*, 2020, **2**, 55–69.
182 R. Jin, G. Li, S. Sharma, Y. Li and X. Du, *Chem. Rev.*, 2021, **121**, 567–648.
183 Y. Liu, H. Tsunoyama, T. Akita and T. Tsukuda, *J. Phys. Chem. C*, 2009, **113**, 13457–13461.
184 H. A. Almukhlifi and R. C. Burns, *Appl. Catal., A*, 2015, **502**, 174–187.
185 M. Cargnello, C. Chen, B. T. Diroll, V. V. T. Doan-Nguyen, R. J. Gorte and C. B. Murray, *J. Am. Chem. Soc.*, 2015, **137**, 6906–6911.
186 N. Sakamoto, H. Ohtsuka, T. Ikeda, K. Maeda, D. Lu, M. Kanehara, K. Teramura, T. Teranishi and K. Domen, *Nanoscale*, 2009, **1**, 106–109.
187 K. Maeda, N. Sakamoto, T. Ikeda, H. Ohtsuka, A. Xiong, D. Lu, M. Kanehara, T. Teranishi and K. Domen, *Chem. – Eur. J.*, 2010, **16**, 7750–7759.
188 T. Ikeda, A. Xiong, T. Yoshinaga, K. Maeda, K. Domen and T. Teranishi, *J. Phys. Chem. C*, 2013, **117**, 2467–2473.

 This journal is © The Royal Society of Chemistry 2021

Open Access Article. Published on 12 2021. Downloaded on 02.06.2026 12:22:59.
This article is licensed under a Creative Commons Attribution 3.0 Unported Licence.

189 K. Maeda, A. Xiong, T. Yoshinaga, T. Ikeda, N. Sakamoto, T. Hisatomi, M. Takashima, D. Lu, M. Kanehara, T. Setoyama, T. Teranishi and K. Domen, *Angew. Chem., Int. Ed.*, 2010, **49**, 4096–4099.
190 A. Xiong, T. Yoshinaga, T. Ikeda, M. Takashima, T. Hisatomi, K. Maeda, T. Setoyama, T. Teranishi and K. Domen, *Eur. J. Inorg. Chem.*, 2014, 767–772.
191 T. Yoshinaga, M. Saruyama, A. Xiong, Y. Ham, Y. Kuang, R. Niishiro, S. Akiyama, M. Sakamoto, T. Hisatomi, K. Domen and T. Teranishi, *Nanoscale*, 2018, **10**, 10420–10427.
192 Y. H. Li, J. Xing, Z. J. Chen, Z. Li, F. Tian, L. R. Zheng, H. F. Wang, P. Hu, H. J. Zhao and H. G. Yang, *Nat. Commun.*, 2013, **4**, 2500.
193 E. Cui and G. Lu, *J. Phys. Chem. C*, 2013, **117**, 26415–26425.
194 E. Cui and G. Lu, *Int. J. Hydrogen Energy*, 2014, **39**, 7672–7685.
195 Y. Zhang, D. A. J. M. Ligthart, X.-Y. Quek, L. Gao and E. J. M. Hensen, *Int. J. Hydrogen Energy*, 2014, **39**, 11537–11546.
196 M. Hojamberdiev, M. M. Khan, Z. Kadirova, K. Kawashima, K. Yubuta, K. Teshima, R. Riedel and M. Hasegawa, *Renewable Energy*, 2019, **138**, 434–444.
197 M. Luo, P. Lu, W. Yao, C. Huang, Q. Xu, Q. Wu, Y. Kuwahara and H. Yamashita, *ACS Appl. Mater. Interfaces*, 2016, **8**, 20667–20674.
198 S. Xu, A. J. Du, J. Liu, J. Ng and D. D. Sun, *Int. J. Hydrogen Energy*, 2011, **36**, 6560–6568.
199 Q. Wu, S. Xiong, P. Shen, S. Zhao, Y. Li, D. Su and A. Orlov, *Catal. Sci. Technol.*, 2015, **5**, 2059–2064.
200 X. L. Du, X. L. Wang, Y. H. Li, Y. L. Wang, J. J. Zhao, L. J. Fang, L. R. Zheng, H. Tong and H. G. Yang, *Chem. Commun.*, 2017, **53**, 9402–9405.
201 S. Liu and Y.-J. Xu, *Sci. Rep.*, 2016, **6**, 22742.
202 F.-X. Xiao, Z. Zeng, S.-H. Hsu, S.-F. Hung, H. M. Chen and B. Liu, *ACS Appl. Mater. Interfaces*, 2015, **7**, 28105–28109.
203 A. Kogo, N. Sakai and T. Tatsuma, *Nanoscale*, 2015, **7**, 14237–14240.
204 L. D. Menard, F. Xu, R. G. Nuzzo and J. C. Yang, *J. Catal.*, 2006, **243**, 64–73.
205 E. W. Elliott, R. D. Glover and J. E. Hutchison, *ACS Nano*, 2015, **9**, 3050–3059.
206 J. Kilmartin, R. Sarip, R. Grau-Crespo, D. D. Tommaso, G. Hogarth, C. Prestipino and G. Sankar, *ACS Catal.*, 2012, **2**, 957–963.
207 B. Zhang, J. Fang, J. Li, J. J. Lau, D. Mattia, Z. Zhong, J. Xie and N. Yan, *Chem. – Asian J.*, 2016, **11**, 532–539.
208 S. Das, A. Goswami, M. Hesari, J. F. Al-Sharab, E. Mikmeková, F. Maran and T. Asefa, *Small*, 2014, **10**, 1473–1478.
209 S. Xie, H. Tsunoyama, W. Kurashige, Y. Negishi and T. Tsukuda, *ACS Catal.*, 2012, **2**, 1519–1523.
210 T. Yoskamtorn, S. Yamazoe, R. Takahata, J.-i. Nishigaki, A. Thivasasith, J. Limtrakul and T. Tsukuda, *ACS Catal.*, 2014, **4**, 3696–3700.
211 S. Yamazoe, T. Yoskamtorn, S. Takano, S. Yadnum, J. Limtrakul and T. Tsukuda, *Chem. Rec.*, 2016, **16**, 2338–2348.
212 C. Lavenn, A. Demessence and A. Tuel, *J. Catal.*, 2015, **322**, 130–138.
213 C. Liu, J. Zhang, J. Huang, C. Zhang, F. Hong, Y. Zhou, G. Li and M. Haruta, *ChemSusChem*, 2017, **10**, 1976–1980.
214 Y. Liu, H. Tsunoyama, T. Akita, S. Xie and T. Tsukuda, *ACS Catal.*, 2011, **1**, 2–6.
215 B. Zhang, S. Kaziz, H. Li, M. G. Hevia, D. Wodka, C. Mazet, T. Bürgi and N. Barrabés, *J. Phys. Chem. C*, 2015, **119**, 11193–11199.
216 B. Zhang, A. Sels, G. Salassa, S. Pollitt, V. Truttmann, C. Rameshan, J. Llorca, W. Olszewski, G. Rupprechter, T. Bürgi and N. Barrabés, *ChemCatChem*, 2018, **10**, 5372–5376.
217 B. Zhang, C. García, A. Sels, G. Salassa, C. Rameshan, J. Llorca, K. Hradil, G. Rupprechter, N. Barrabés and T. Bürgi, *Catal. Commun.*, 2019, **130**, 105768.
218 C. García, S. Pollitt, M. van der Linden, V. Truttmann, C. Rameshan, R. Rameshan, E. Pittenauer, G. Allmaier, P. Kregsamer, M. Stöger-Pollach, N. Barrabés and G. Rupprechter, *Catal. Today*, 2019, **336**, 174–185.
219 Y. Liu, H. Tsunoyama, T. Akita and T. Tsukuda, *Chem. Commun.*, 2010, **46**, 550–552.
220 Y. Zhu, H. Qian and R. Jin, *Chem. – Eur. J.*, 2010, **16**, 11455–11462.
221 Y. Zhu, H. Qian, A. Das and R. Jin, *Chin. J. Catal.*, 2011, **32**, 1149–1155.
222 J. Liu, K. S. Krishna, Y. B. Losovyj, S. Chattopadhyay, N. Lozova, J. T. Miller, J. J. Spivey and C. S. S. R. Kumar, *Chem. – Eur. J.*, 2013, **19**, 10201–10208.
223 J. Fang, J. Li, B. Zhang, X. Yuan, H. Asakura, T. Tanaka, K. Teramura, J. Xie and N. Yan, *Nanoscale*, 2015, **7**, 6325–6333.
224 K. O. Sulaiman, V. Sudheeshkumar and R. W. J. Scott, *RSC Adv.*, 2019, **9**, 28019–28027.
225 S. Gaur, J. T. Miller, D. Stellwagen, A. Sanampudi, C. S. S. R. Kumar and J. J. Spivey, *Phys. Chem. Chem. Phys.*, 2012, **14**, 1627–1634.
226 X. Nie, H. Qian, Q. Ge, H. Xu and R. Jin, *ACS Nano*, 2012, **6**, 6014–6022.
227 X. Nie, C. Zeng, X. Ma, H. Qian, Q. Ge, H. Xu and R. Jin, *Nanoscale*, 2013, **5**, 5912–5918.
228 W. Li, Q. Ge, X. Ma, Y. Chen, M. Zhu, H. Xu and R. Jin, *Nanoscale*, 2016, **8**, 2378–2385.
229 Y. Li, Y. Chen, S. D. House, S. Zhao, Z. Wahab, J. C. Yang and R. Jin, *ACS Appl. Mater. Interfaces*, 2018, **10**, 29425–29434.
230 Y. Chen, C. Liu, Q. Tang, C. Zeng, T. Higaki, A. Das, D.-e. Jiang, N. L. Rosi and R. Jin, *J. Am. Chem. Soc.*, 2016, **138**, 1482–1485.
231 Z. Wu, D.-e. Jiang, A. K. P. Mann, D. R. Mullins, Z.-A. Qiao, L. F. Allard, C. Zeng, R. Jin and S. H. Overbury, *J. Am. Chem. Soc.*, 2014, **136**, 6111–6122.
232 Z. Wu, G. Hu, D.-e. Jiang, D. R. Mullins, Q.-F. Zhang, L. F. Allard, Jr., L.-S. Wang and S. H. Overbury, *Nano Lett.*, 2016, **16**, 6560–6567.
233 S. Pollitt, V. Truttmann, T. Haunold, C. Garcia, W. Olszewski, J. Llorca, N. Barrabés and G. Rupprechter, *ACS Catal.*, 2020, **10**, 6144–6148.
234 G. Ma, A. Binder, M. Chi, C. Liu, R. Jin, D.-e. Jiang, J. Fan and S. Dai, *Chem. Commun.*, 2012, **48**, 11413–11415.

Open Access Article. Published on 12 2021. Downloaded on 02.06.2026 12:22:59.
This article is licensed under a Creative Commons Attribution 3.0 Unported Licence.

235 Y. Negishi, N. Shimizu, K. Funai, R. Kaneko, K. Wakamatsu, A. Harasawa, S. Hossain, M. E. Schuster, D. Ozkaya, W. Kurashige, T. Kawawaki, S. Yamazoe and S. Nagaoka, *Nanoscale Adv.*, 2020, **2**, 669–678.
236 G. Li and R. Jin, *J. Am. Chem. Soc.*, 2014, **136**, 11347–11354.
237 A. Shivhare, D. M. Chevrier, R. W. Purves and R. W. J. Scott, *J. Phys. Chem. C*, 2013, **117**, 20007–20016.
238 Y. Tan, X. Y. Liu, L. Zhang, A. Wang, L. Li, X. Pan, S. Miao, M. Haruta, H. Wei, H. Wang, F. Wang, X. Wang and T. Zhang, *Angew. Chem., Int. Ed.*, 2017, **56**, 2709–2713.
239 M. Urushizaki, H. Kitazawa, S. Takano, R. Takahata, S. Yamazoe and T. Tsukuda, *J. Phys. Chem. C*, 2015, **119**, 27483–27488.
240 Y. Negishi, M. Mizuno, M. Hirayama, M. Omatoi, T. Takayama, A. Iwase and A. Kudo, *Nanoscale*, 2013, **5**, 7188–7192.
241 Y. Negishi, Y. Matsuura, R. Tomizawa, W. Kurashige, Y. Niihori, T. Takayama, A. Iwase and A. Kudo, *J. Phys. Chem. C*, 2015, **119**, 11224–11232.
242 W. Kurashige, R. Kumazawa, Y. Mori and Y. Negishi, *J. Mater. Appl.*, 2018, **7**, 1–11.
243 W. Kurashige, R. Kumazawa, D. Ishii, R. Hayashi, Y. Niihori, S. Hossain, L. V. Nair, T. Takayama, A. Iwase, S. Yamazoe, T. Tsukuda, A. Kudo and Y. Negishi, *J. Phys. Chem. C*, 2018, **122**, 13669–13681.
244 W. Kurashige, R. Hayashi, K. Wakamatsu, Y. Kataoka, S. Hossain, A. Iwase, A. Kudo, S. Yamazoe and Y. Negishi, *ACS Appl. Energy Mater.*, 2019, **2**, 4175–4187.
245 W. Kurashige, Y. Mori, S. Ozaki, M. Kawachi, S. Hossain, T. Kawawaki, C. J. Shearer, A. Iwase, G. F. Metha, S. Yamazoe, A. Kudo and Y. Negishi, *Angew. Chem., Int. Ed.*, 2020, **59**, 7076–7082.
246 X. Gao and W. Chen, *Chem. Commun.*, 2017, **53**, 9733–9736.
247 S. Zhao, R. Jin, H. Abroshan, C. Zeng, H. Zhang, S. D. House, E. Gottlieb, H. J. Kim, J. C. Yang and R. Jin, *J. Am. Chem. Soc.*, 2017, **139**, 1077–1080.
248 O. Ioannidou and A. Zabaniotou, *Renewable Sustainable Energy Rev.*, 2007, **11**, 1966–2005.
249 H. Yin, Z. Ma, M. Chi and S. Dai, *Catal. Today*, 2011, **160**, 87–95.
250 F. Rashidi, T. Sasaki, A. M. Rashidi, A. N. Kharat and K. J. Jozani, *J. Catal.*, 2013, **299**, 321–335.
251 Y. Miseki, H. Kato and A. Kudo, *Energy Environ. Sci.*, 2009, **2**, 306–314.
252 A. Kudo, A. Tanaka, K. Domen and T. Onishi, *J. Catal.*, 1988, **111**, 296–301.
253 W.-J. Ong, L.-L. Tan, Y. H. Ng, S.-T. Yong and S.-P. Chai, *Chem. Rev.*, 2016, **116**, 7159–7329.
254 W. Ren, L. Xiong, G. Nie, H. Zhang, X. Duan and S. Wang, *Environ. Sci. Technol.*, 2020, **54**, 1267–1275.
255 A. Longo, E. J. J. de Boed, N. Mammen, M. van der Linden, K. Honkala, H. Häkkinen, P. E. de Jongh and B. Donoeva, *Chem. – Eur. J.*, 2020, **26**, 7051–7058.
256 S. S. Karpova, V. A. Moshnikov, S. V. Mjakin and E. S. Kolovangina, *Semiconductors*, 2013, **47**, 392–395.
257 J. Datka, A. M. Turek, J. M. Jehng and I. E. Wachs, *J. Catal.*, 1992, **135**, 186–199.
258 Z. Bao, V. Fung, F. Polo-Garzon, Z. D. Hood, S. Cao, M. Chi, L. Bai, D.-e. Jiang and Z. Wu, *J. Catal.*, 2020, **384**, 49–60.
259 C. Lavenn, F. Albrieux, G. Bergeret, R. Chiriac, P. Delichère, A. Tuel and A. Demessence, *Nanoscale*, 2012, **4**, 7334–7337.
260 Y.-J. Xu, P. Landon, D. Enache, A. F. Carley, M. W. Roberts and G. J. Hutchings, *Catal. Lett.*, 2005, **101**, 175–179.
261 B. P. C. Hereijgers and B. M. Weckhuysen, *J. Catal.*, 2010, **270**, 16–25.
262 M. W. Heaven, A. Dass, P. S. White, K. M. Holt and R. W. Murray, *J. Am. Chem. Soc.*, 2008, **130**, 3754–3755.
263 M. Haruta, T. Kobayashi, H. Sano and N. Yamada, *Chem. Lett.*, 1987, 405–408.
264 I. Ciabatti, C. Femoni, M. C. Iapalucci, S. Ruggieri and S. Zacchini, *Coord. Chem. Rev.*, 2018, **355**, 27–38.
265 T. Imaoka, H. Kitazawa, W.-J. Chun, S. Omura, K. Albrecht and K. Yamamoto, *J. Am. Chem. Soc.*, 2013, **135**, 13089–13095.
266 K. Yamamoto, T. Imaoka, W.-J. Chun, O. Enoki, H. Katoh, M. Takenaga and A. Sonoi, *Nat. Chem.*, 2009, **1**, 397–402.
267 S. Blonski and S. H. Garofalini, *Surf. Sci.*, 1993, **295**, 263–274.
268 J. H. Kwak, J. Hu, D. Mei, C.-W. Yi, D. H. Kim, C. H. F. Peden, L. F. Allard and J. Szanyi, *Science*, 2009, **325**, 1670–1673.
269 Y. Watanabe, X. Wu, H. Hirata and N. Isomura, *Catal. Sci. Technol.*, 2011, **1**, 1490–1495.
270 C. Yin, F. R. Negreiros, G. Barcaro, A. Beniya, L. Sementa, E. C. Tyo, S. Bartling, K.-H. Meiwes-Broer, S. Seifert, H. Hirata, N. Isomura, S. Nigam, C. Majumder, Y. Watanabe, A. Fortunelli and S. Vajda, *J. Mater. Chem. A*, 2017, **5**, 4923–4931.
271 U. Heiz, A. Sanchez, S. Abbet and W.-D. Schneider, *J. Am. Chem. Soc.*, 1999, **121**, 3214–3217.
272 R. M. Heck, R. J. Farrauto and S. T. Gulati, *Catalytic Air Pollution Control: Commercial Technology*, John Wiley & Sons, *America*, 3rd edn, 2009.
273 D. Ren, L. He, L. Yu, R.-S. Ding, Y.-M. Liu, Y. Cao, H.-Y. He and K.-N. Fan, *J. Am. Chem. Soc.*, 2012, **134**, 17592–17598.
274 A. Fujishima and K. Honda, *Nature*, 1972, **238**, 37–38.
275 A. Kudo and Y. Miseki, *Chem. Soc. Rev.*, 2009, **38**, 253–278.
276 K. Maeda, *ACS Catal.*, 2013, **3**, 1486–1503.
277 J. Yang, D. Wang, H. Han and C. Li, *Acc. Chem. Res.*, 2013, **46**, 1900–1909.
278 T. Kawawaki, Y. Kataoka, S. Ozaki, M. Kawachi, M. Hirata and Y. Negishi, *Chem. Commun.*, 2021, **57**, 417–440.
279 Y. Negishi, *Bull. Chem. Soc. Jpn.*, 2014, **87**, 375–389.
280 W. Kurashige, Y. Niihori, S. Sharma and Y. Negishi, *Coord. Chem. Rev.*, 2016, **320–321**, 238–250.
281 Q. Wang and K. Domen, *Chem. Rev.*, 2020, **120**, 919–985.
282 K. Maeda and K. Domen, *J. Phys. Chem. Lett.*, 2010, **1**, 2655–2661.
283 K. Maeda and K. Domen, *J. Phys. Chem. C*, 2007, **111**, 7851–7861.
284 K. Maeda, *J. Photochem. Photobiol. C*, 2011, **12**, 237–268.
285 K. Maeda, D. Lu and K. Domen, *Chem. – Eur. J.*, 2013, **19**, 4986–4991.
286 K. Maeda, K. Teramura, D. Lu, N. Saito, Y. Inoue and K. Domen, *Angew. Chem., Int. Ed.*, 2006, **45**, 7806–7809.

 This journal is © The Royal Society of Chemistry 2021

Open Access Article. Published on 12 2021. Downloaded on 02.06.2026 12:22:59.
This article is licensed under a Creative Commons Attribution 3.0 Unported Licence.

287 M. Yoshida, K. Takanabe, K. Maeda, A. Ishikawa, J. Kubota, Y. Sakata, Y. Ikezawa and K. Domen, *J. Phys. Chem. C*, 2009, **113**, 10151–10157.
288 K. Maeda, K. Teramura, D. Lu, N. Saito, Y. Inoue and K. Domen, *J. Phys. Chem. C*, 2007, **111**, 7554–7560.
289 S. J. Tauster, S. C. Fung and R. L. Garten, *J. Am. Chem. Soc.*, 1978, **100**, 170–175.
290 S. J. Tauster, *Acc. Chem. Res.*, 1987, **20**, 389–394.
291 E. J. Braunschweig, A. D. Logan, A. K. Datye and D. J. Smith, *J. Catal.*, 1989, **118**, 227–237.
292 A. D. Logan, E. J. Braunschweig, A. K. Datye and D. J. Smith, *Langmuir*, 1988, **4**, 827–830.
293 S. Labich, E. Taglauer and H. Knözinger, *Top. Catal.*, 2000, **14**, 153–161.
294 L. Liu, C. Ge, W. Zou, X. Gu, F. Gao and L. Dong, *Phys. Chem. Chem. Phys.*, 2015, **17**, 5133–5140.
295 X. Liu, M.-H. Liu, Y.-C. Luo, C.-Y. Mou, S. D. Lin, H. Cheng, J.-M. Chen, J.-F. Lee and T.-S. Lin, *J. Am. Chem. Soc.*, 2012, **134**, 10251–10258.
296 H. Tang, J. Wei, F. Liu, B. Qiao, X. Pan, L. Li, J. Liu, J. Wang and T. Zhang, *J. Am. Chem. Soc.*, 2016, **138**, 56–59.
297 T. Kawawaki, Y. Mori, K. Wakamatsu, S. Ozaki, M. Kawachi, S. Hossain and Y. Negishi, *J. Mater. Chem. A*, 2020, **8**, 16081–16113.
298 Z. Wang, C. Li and K. Domen, *Chem. Soc. Rev.*, 2019, **48**, 2109–2125.
299 Y. Wang, H. Suzuki, J. Xie, O. Tomita, D. J. Martin, M. Higashi, D. Kong, R. Abe and J. Tang, *Chem. Rev.*, 2018, **118**, 5201–5241.
300 D. E. Carlson and C. R. Wronski, *Appl. Phys. Lett.*, 1976, **28**, 671–673.
301 X.-T. Wang, T. Ouyang, L. Wang, J.-H. Zhong and Z.-Q. Liu, *Angew. Chem., Int. Ed.*, 2020, **59**, 6492–6499.
302 C. Huang, Y. Zou, Y.-Q. Ye, T. Ouyang, K. Xiao and Z.-Q. Liu, *Chem. Commun.*, 2019, **55**, 7687–7690.
303 M. K. Sheehan, M. Rudden, H. Cai and C.-K. Tsung, *Catal. Lett.*, 2016, **146**, 309–318.
304 L. Liu, X. Zhang, L. Yang, L. Ren, D. Wang and J. Ye, *Natl. Sci. Rev.*, 2017, **4**, 761–780.
305 C. Jiang, S. J. A. Moniz, A. Wang, T. Zhang and J. Tang, *Chem. Soc. Rev.*, 2017, **46**, 4645–4660.
306 M. G. Walter, E. L. Warren, J. R. McKone, S. W. Boettcher, Q. Mi, E. A. Santori and N. S. Lewis, *Chem. Rev.*, 2010, **110**, 6446–6473.
307 Z. W. Seh, J. Kibsgaard, C. F. Dickens, I. Chorkendorff, J. K. Nørskov and T. F. Jaramillo, *Science*, 2017, **355**, eaad4998.
308 M. R. Narouz, K. M. Osten, P. J. Unsworth, R. W. Y. Man, K. Salorinne, S. Takano, R. Tomihara, S. Kaappa, S. Malola, C.-T. Dinh, J. D. Padmos, K. Ayoo, P. J. Garrett, M. Nambo, J. H. Horton, E. H. Sargent, H. Häkkinen, T. Tsukuda and C. M. Crudden, *Nat. Chem.*, 2019, **11**, 419–425.
309 D. P. Anderson, J. F. Alvino, A. Gentleman, H. A. Qahtani, L. Thomsen, M. I. J. Polson, G. F. Metha, V. B. Golovko and G. G. Andersson, *Phys. Chem. Chem. Phys.*, 2013, **15**, 3917–3929.
310 D. P. Anderson, R. H. Adnan, J. F. Alvino, O. Shipper, B. Donoeva, J.-Y. Ruzicka, H. Al Qahtani, H. H. Harris, B. Cowie, J. B. Aitken, V. B. Golovko, G. F. Metha and G. G. Andersson, *Phys. Chem. Chem. Phys.*, 2013, **15**, 14806–14813.
311 H. S. Al Qahtani, R. Higuchi, T. Sasaki, J. F. Alvino, G. F. Metha, V. B. Golovko, R. Adnan, G. G. Andersson and T. Nakayama, *RSC Adv.*, 2016, **6**, 110765–110774.
312 S. Wang, S. Yin, G. Chen, L. Li and H. Zhang, *Catal. Sci. Technol.*, 2016, **6**, 4090–4104.
313 L. Li, L. Dou and H. Zhang, *Nanoscale*, 2014, **6**, 3753–3763.
314 S. Yin, J. Li and H. Zhang, *Green Chem.*, 2016, **18**, 5900–5914.
315 S. H. Joo, J. Y. Park, C.-K. Tsung, Y. Yamada, P. Yang and G. A. Somorjai, *Nat. Mater.*, 2009, **8**, 126–131.
316 M. A. Habeeb Muhammed and T. Pradeep, *Small*, 2011, **7**, 204–208.
317 A. Samanta, B. B. Dhar and R. N. Devi, *J. Phys. Chem. C*, 2012, **116**, 1748–1754.
318 V. Sudheeshkumar, A. Shivhare and R. W. J. Scott, *Catal. Sci. Technol.*, 2017, **7**, 272–280.
319 H. Chen, C. Liu, M. Wang, C. Zhang, G. Li and F. Wang, *Chin. J. Catal.*, 2016, **37**, 1787–1793.
320 Y. Zheng, X. Zhang, Y. Yao, X. Chen and Q. Yang, *RSC Adv.*, 2015, **5**, 105747–105752.
321 P. M. Arnal, M. Comotti and F. Schüth, *Angew. Chem., Int. Ed.*, 2006, **45**, 8224–8227.
322 V. Sudheeshkumar, A. Lushington, X. Sun and R. W. J. Scott, *ACS Appl. Nano Mater.*, 2018, **1**, 6904–6911.
323 X. Cui, J. Wang, B. Liu, S. Ling, R. Long and Y. Xiong, *J. Am. Chem. Soc.*, 2018, **140**, 16514–16520.
324 X. Li, T. W. Goh, L. Li, C. Xiao, Z. Guo, X. C. Zeng and W. Huang, *ACS Catal.*, 2016, **6**, 3461–3468.
325 L. Liu, Y. Song, H. Chong, S. Yang, J. Xiang, S. Jin, X. Kang, J. Zhang, H. Yu and M. Zhu, *Nanoscale*, 2016, **8**, 1407–1412.
326 L. Sun, Y. Yun, H. Sheng, Y. Du, Y. Ding, P. Wu, P. Li and M. Zhu, *J. Mater. Chem. A*, 2018, **6**, 15371–15376.
327 C. Liu, C. Zeng, T.-Y. Luo, A. D. Merg, R. Jin and N. L. Rosi, *J. Am. Chem. Soc.*, 2016, **138**, 12045–12048.
328 Y. Luo, S. Fan, W. Yu, Z. Wu, D. A. Cullen, C. Liang, J. Shi and C. Su, *Adv. Mater.*, 2018, **30**, 1704576.
329 L. M. Rossi, J. L. Fiorio, M. A. S. Garcia and C. P. Ferraz, *Dalton Trans.*, 2018, **47**, 5889–5915.
330 Z. Wu and R. Jin, *ACS Nano*, 2009, **3**, 2036–2042.
331 Y. Tai, W. Yamaguchi, M. Okada, F. Ohashi, K.-i. Shimizu, A. Satsuma, K. Tajiri and H. Kageyama, *J. Catal.*, 2010, **270**, 234–241.
332 R. H. Adnan and V. B. Golovko, *Catal. Lett.*, 2019, **149**, 449–455.
333 H. Häkkinen and U. Landman, *Phys. Rev. B: Condens. Matter Mater. Phys.*, 2000, **62**, R2287–R2290.
334 L. Vitos, A. V. Ruban, H. L. Skriver and J. Kollár, *Surf. Sci.*, 1998, **411**, 186–202.
335 C. Garcia, V. Truttmann, I. Lopez, T. Haunold, C. Marini, C. Rameshan, E. Pittenauer, P. Kregsamer, K. Dobrezberger, M. Stöger-Pollach, N. Barrabés and G. Rupprechter, *J. Phys. Chem. C*, 2020, **124**, 23626–23636.
336 K. T. Chan, J. B. Neaton and M. L. Cohen, *Phys. Rev. B: Condens. Matter Mater. Phys.*, 2008, **77**, 235430.
337 D. R. Kauffman, D. R. Alfonso, D. N. Tafen, C. Wang, Y. Zhou, Y. Yu, J. W. Lekse, X. Deng, V. Espinoza, J. Trindell,

Open Access Article. Published on 12 2021. Downloaded on 02.06.2026 12:22:59.
This article is licensed under a Creative Commons Attribution 3.0 Unported Licence.

O. K. Ranasingha, A. Roy, J.-S. Lee and H. L. Xin, *J. Phys. Chem. C*, 2018, **122**, 27991–28000.
338 D. R. Alfonso, D. Kauffman and C. Matranga, *J. Chem. Phys.*, 2016, **144**, 184705.
339 N. Austin, S. Zhao, J. R. McKone, R. Jin and G. Mpourmpakis, *Catal. Sci. Technol.*, 2018, **8**, 3795–3805.
340 A. V. Nagarajan, R. Juarez-Mosqueda, M. J. Cowan, R. Jin, D. R. Kauffman and G. Mpourmpakis, *SN Appl. Sci.*, 2020, **2**, 680.
341 S. Zhao, N. Austin, M. Li, Y. Song, S. D. House, S. Bernhard, J. C. Yang, G. Mpourmpakis and R. Jin, *ACS Catal.*, 2018, **8**, 4996–5001.
342 D. A. Pichugina, N. A. Nikitina and N. E. Kuz'menko, *J. Phys. Chem. C*, 2020, **124**, 3080–3086.
343 J. Han, J. Lu, M. Wang, Y. Wang and F. Wang, *Chin. J. Chem.*, 2019, **37**, 977–988.
344 R. Takahata, S. Yamazoe, Y. Maehara, K. Yamazaki, S. Takano, W. Kurashige, Y. Negishi, K. Gohara and T. Tsukuda, *J. Phys. Chem. C*, 2020, **124**, 6907–6912.
345 H. Asakura, S. Hosokawa, T. Ina, K. Kato, K. Nitta, K. Uera, T. Uruga, H. Miura, T. Shishido, J. Ohyama, A. Satsuma, K. Sato, A. Yamamoto, S. Hinokuma, H. Yoshida, M. Machida, S. Yamazoe, T. Tsukuda, K. Teramura and T. Tanaka, *J. Am. Chem. Soc.*, 2018, **140**, 176–184.
346 C. Zeng, Y. Chen, A. Das and R. Jin, *J. Phys. Chem. Lett.*, 2015, **6**, 2976–2986.
347 S. Tian, Y. Cao, T. Chen, S. Zang and J. Xie, *Chem. Commun.*, 2020, **56**, 1163–1174.
348 J. Schneider, M. Matsuoka, M. Takeuchi, J. Zhang, Y. Horiuchi, M. Anpo and D. W. Bahnemann, *Chem. Rev.*, 2014, **114**, 9919–9986.

 This journal is © The Royal Society of Chemistry 2021